The Pennsylvania State University

The Graduate School

EXPERIMENTAL CHARACTERIZATION OF MARINE AGGREGATE FRAGMENTATION STRENGTH THROUGH LABORATORY AND FIELD METHODS

A Dissertation in

Mechanical Engineering

by

Yixuan Song

Submitted in Partial Fulfillment
of the Requirements
for the Degree of

Doctor of Philosophy

May 2023

The dissertation of Yixuan Song was reviewed and approved by the following:

Matthew J. Rau
Assistant Professor of Mechanical and Aerospace Engineering
The George Washington University
Dissertation Advisor
Chair of Committee

Margaret L. Byron
Assistant Professor of Mechanical Engineering

Robert F. Kunz
Professor of Mechanical Engineering and Aerospace Engineering
Associate Head for Graduate Programs of Mechanical Engineering

Raymond G. Najjar, Jr.
Professor in Meteorology, Atmospheric Science, and Geoscience

Mary I. Frecker
Professor of Mechanical Engineering and Biomedical Engineering
Department Head of Mechanical Engineering
Riess Chair of Engineering
Director of the Penn State Center for Biodevices

ABSTRACT

Organic particulate matter plays a crucial role in the carbon transport through the oceanic water column. The size of the particulate matter, influenced by hydrodynamic fragmentation, primarily regulates the sinking flux of carbon from the surface ocean. Disaggregation, caused by turbulence-induced shear, acts to fracture or erode large particles into slower-settling sub-aggregates and primary particles. The strength and breakup response of organic marine aggregates (*i.e.,* marine snow particles consisting of phytoplankton) is poorly understood, limiting our ability to accurately predict marine particle transport effects on the global carbon cycle. In this dissertation, we have implemented field fragmentation measurements of naturally occurring marine aggregates and incorporated laboratory experiments in parallel to explain the formation and disruption mechanisms of marine snow aggregates.

We have developed one in-situ disaggregation system and measured the fragmentation of aggregates during two recent field deployments in the Northeastern United States Continental Shelf and Lake Tahoe. The prototype used one variable speed thruster to draw the fluid flow through a long tube and generated fully developed turbulent flows inside. By adjusting the thruster speed, we obtained varying flow conditions from a laminar flow to a strong turbulent flow. The disaggregation system exposed naturally occurring particles to this calibrated flow condition inside the tube. We also employed a programmable controller with power sources that allows for in-situ measurements at a depth of up to 200 m. We used a submersible digital holographic camera to capture particle size statistics and images in the Northeastern United States Continental Shelf, and deployed an underwater particle

size meter during the deployment in Lake Tahoe. Fragmentation results have validated the in-situ disaggregation system and showed particle fragmentation due to turbulence in the ocean and lake environments.

In the laboratory, we cultured two diatom species, Odontella aurita and Skeletonema grethae, to prepare simulated marine aggregates. We have developed a novel rotating/oscillating tank that can form aggregates and perform breakup experiments in a controlled environment. This novel tank does not need any manipulation of aggregates at all. The facility can additionally provide shear rates across a wide range of the ocean from very low turbulence in the mixed layer to high shear in the surface ocean. We formed diatom aggregates by operating the tank at a constant rotation speed and disrupted them when the tank underwent a harmonic oscillation around its central axis, which was oriented horizontally.

The flow motion inside the rotating/oscillating tank was a superposition of a solid body rotation and a harmonic oscillatory flow that was also an extension of the famous Stokes' second problem inside a cylindrical geometric configuration. We provided an analytical solution to this viscous oscillatory flow using the Laplace Transform and Residue Theorem. We detailed the transient starting condition and the quasi steady fluid motion, which we presented along with a particle image velocimetry experiment for validation. Given proper boundary conditions, this roller tank created calibrated laminar shear that is similar in magnitude to that in the ocean.

With high-speed imaging techniques, we captured the fragmentation of laboratory-made diatom aggregates exposed to the calibrated oscillatory flow. We have also developed a

unique image processing method that enabled continuous tracking of particle positions, sizes, and morphologies, as well as the determination of individual aggregate breakup events. The image processing consisted of background removal, particle identification, particle matching, and breakup detection. The analytical solution of fluid flow allowed us to couple the hydrodynamic conditions to the recorded time history. This method has great potential to capture breakup events of large marine snow particles, quantify the aggregate morphological changes leading up to and at breakup, and provide data sufficient for statistical analysis of laboratory aggregate populations. We tested the method using laboratory-cultured Odontella aurita. These fragmented aggregates underwent substantial morphological evolutions prior to the fragmentation.

The formation theory of colloidal particles is relatively well established but the knowledge of biological bonding governing the strength of naturally occurring aggregates is still limited. To better comprehend fragmentation processes and adhesion forces, we implemented aggregate breakup experiments with diatom aggregates and colloidal flocs made in the laboratory from polystyrene and polyethylene microspheres. We captured the fragmentation of diatom aggregates and polystyrene flocs after substantial deformation, while polyethylene aggregates did not break. The fragmentation results provided upper and lower limits of the biological bonding strength of diatom aggregates using two colloidal floc types. Additionally, we employed a force balance model to evaluate attractive interactions within clusters of particles using time series of shear and morphology. We found that the fractal structures of the aggregates lead to a power law of breakup strength with size. This study also reveals time-integrated stress is influential in floc fragmentation.

Finally, we summarize our contributions related to the fragmentation of marine snow and its influence on carbon transport. Knowing the breakup strength of marine snow can improve our predictions of particle fragmentation in the particle population balance, which further enhances our understanding of the oceanic carbon sequestration and the mass transport in the biological carbon pump. We additionally identify multiple priorities for the continuation of this work and address recommended future directions.

TABLE OF CONTENTS

LIST OF FIGURES

LIST OF TABLES

NOMENCLATURE

Symbol	Description
a	magnitude of tank oscillation
b	constant rotation speed
d	aggregate length scale
d_0	average particle size after three hours of aggregation
d_1	primary particle size
d_{ave}	average particle size
d_c	mean size of aggregates in Stokes number calculation
d_{eq}	equivalent diameter
d_f	characteristic length of a floc
d_{Fmin}	minimum Feret diameter
d_{max}	largest stable aggregate size
d_n	neck size
d_t	inner diameter of tube
d_∞	steady-state mean particle size
e	charge of a single electron
f	dimensionless velocity in time domain
g	buoyance force / gravitational force
g_1, g_2	interrogation window 1 and 2
k	Boltzmann's constant
l	separation distance
l_t	tube length
l_0	minimum equilibrium distance

m	particle mass
m_1	primary particle mass
m_f	floc mass
n	exponent relating the accumulated stress with the strain difference
n_i	number of ions of each ion
r	radial coordinates
r_0	balance length for stable region
r_p	effective radius of a particle
r_s	radius of stable region
s	complex frequency after Laplace Transform
t	time
t_c	time for flow rate calibration
t_e	experiment time
t_f	flushing time
t_m	measurement time
u'	velocity fluctuation
$\overline{u}$	average floc velocity in the tube
$u_{f,1}$, $u_{f,2}$	corresponding fluid velocity at subaggregates 1 and 2
u_p	particle velocity at its center of mass
u_θ	azimuthal fluid velocity
v_i	valency of each ionic species
w_s	aggregate sinking velocity
x	strength exponent relating the breakup strength and the aggregate size
z	distance between the particle surface and the slipping plane

z_0, $z_{0,n}$	simple pole of the complex-value function; the n^{th} simple pole
A_{11}	Hamaker constant for solid material 1
A_{131}	Hamaker constant for two same materials 1 (PE or PS) interacting through medium 3 (water)
A_{33}	Hamaker constant for liquid material 3
A_H	Hamaker constant
A_i	aggregation rate at which smaller particles aggregate into larger clusters of mass m
A_o	aggregation rate at which aggregates of mass m aggregate into flocs of even greater mass
AR	aspect ratio
B_i	breakup rate at which larger aggregates break into smaller sub-aggregates of mass m
B_o	breakup rate at which aggregates of mass m disrupt into even smaller particles
C_0	constant relating the hydrodynamic pressure stress to velocity fluctuations ~ 0.5
C_1, C_2	constants to be solved in Chapter 2
D_{12}	Taylor deformation parameter
D_2	two-dimensional fractal dimension based on major axis length
Df	fractal dimension of a floc or aggregate
Dp	two-dimensional fractal dimension based on perimeter
F	dimensionless velocity in frequency domain
F_1	interparticle bonding force
F_c	coupling force between two subaggregates
F^{AB}	Lewis acid base force
F^{EL}	electrostatic force

F^{LW}	van der Waals force
G	shear rate
G_m	maximum shear rate
J_1	the Bessel function of the first kind and of order one
K	breakup frequency
K_1	the modified Bessel function of the second kind and of order one
L	characteristic length scale
L_{ma}	major axis length of a floc
L_{mi}	minor axis length of a floc
L_n	neck size of a deformed particle
M	total mass
M_2, N_2	maximum numbers of x and y pixels in the g_2 interrogation window
MQD	minimum quadratic difference
MQD_R	ratio of the MQD
N	number distribution of particles
P	perimeter of aggregate
P'	gauge pressure across the aggregate
QD	quadratic difference
R	tank radius
R^2	coefficient of determination
Re	Reynolds number
R_s	radius of microspheres
S_{io}	sources or sinks of particle mass
SR	stable region

St	Strouhal number
ST	Stokes number
T	absolute temperature
U	characteristic velocity scale
V_1, V_2	volume of subaggregates 1 and 2
V_f	normalized volume fraction
W	particle mass loss due to the gravitational settling
W^{AB}	surface energy of Lewis acid base interaction
W^{DL}	electrostatic repulsion surface energy
W_{DLVO}	total free surface energy per unit area in DLVO theory
W^{LW}	surface energy of van der Waals attraction
α	particle stickiness
α_n	the n^{th} zero of J_1
β	neck-min-Feret ratio
β_A	aggregation kernel
γ_{ff}	interfacial tension between the fluid phases
γ_L	liquid surface tension
γ^{LW}	Lifshitz-van der Waals surface energy (apolar energy)
$\gamma_{p,f}$	particle-fluid interfacial tension
γ^+	electron accepticity
γ^-	electron donicity
δ	characteristic length scale in the oscillatory laminar flow
δ_d	characteristic boundary layer thickness for flow over a rotating disk
δ_s	penetration depth

ε	turbulence dissipation rates
ε_0	permittivity of free space
ε_1	dielectric constant of water
$\hat{\varepsilon}$	equivalent dissipation rates calculated from shear rates
ε_b	turbulence dissipation energy that causes the breakup
ε_e	strain of a deformed aggregate
ζ	zeta potential
η	dimensionless radius distance
η_K	Kolmogorov length scale
η_R	dimensionless radius of roller tank
θ	contact angle
κ	inverse Debye length
λ	decay length
μ	dynamic viscosity
ν	kinematic viscosity
ξ	empirical constant relating particle sinking velocity to its size
ρ	medium density
ρ_f	density of salt water
ρ_l	liquid density
ρ_p	density of flocs
σ_1	primary cohesive stress
σ_b	breakup stress
σ_f	fluid stress
σ_n	necking stress

σ_y	yield strength of an aggregate
τ	dimensionless time
τ_w	tube wall shear stress
φ	porosity of an aggregate
φ_0	colloid surface potential
ϕ	orientation angle between the particle's major axis and the streamwise direction
χ	exponent relating breakup frequency to the particle length scale
ω	oscillation frequency
Γ	particle size distribution function
ΔG^{AB}	free polar potential energy for a geometric configuration of two parallel flat plates
ΔG_{SL}	polar surface free energy between solid and liquid
$\Delta\varepsilon$	strain difference
Ω	tank rotation rate in rad/s

ABBREVIATIONS

Symbol	Description
1D	one-dimensional
2D	two-dimensional
3D	three-dimensional
iDAS	in-situ disaggregation system
ppt	parts per thousand
A	aggregation processes in population balance
AB	Lewis acid base force
AM	aggregation mode
B	breakup processes in population balance
CS	Continental Shelf
DIH	digital in-line holography
DL	electrostatic repulsion
DLVO	Derjaguin–Landau–Verwey–Overbeek (theory)
ESC	electronic speed controller
FM	fragmentation mode
FOV	field of view
I2C	inter-integrated circuit
IDE	integrated development environment
LW	van der Waals attraction
MQD	minimum quadratic difference
OA	Odontella aurita
PBE	population balance equation

PE	polyethylene
PIV	particle image velocimetry
POD	proper orthogonal decomposition
PS	sulfate polystyrene
PSD	particle size distribution
PTV	particle tracking velocimetry
PWM	pulse-width modulation
QD	quadratic difference
RTC	real time clock
SG	Skeletonema grethae
SR	stable region
TEP	transparent exopolymer particles
XDLVO	extended Derjaguin–Landau–Verwey–Overbeek (theory)

ACKNOWLEDGEMENTS

First of all, I would like to acknowledge the mentorship of my advisor Dr. Matthew Rau. I always feel lucky to have him as my advisor, as he is thoughtful, knowledgeable, willing to listen, and glad to spend time with his students. (I also feel guilty sometimes because I am a big time sink during the meeting, paper revising….) I am lucky to become his second Ph.D. student, since he is willing to teach us in person and show us how to start a lab. I am sincerely grateful to him, for his high standards in every aspect of my research, and his continued support and guidance of how to become a better researcher. He has also shared with me many external research opportunities and resources for career development.

I am really grateful to my other graduate committee members for their time and thoughtful input and review of my dissertation research. Dr. Byron is always friendly and willing to help. She shares her lab resources and many novel research ideas with me. I really like the weekly FDRC originally hosted by Dr. Kunz, which has opened my eyes to more interesting fluid research. Dr. Najjar is a nice and knowledgeable professor. He helped spark my interest in a career of ocean science and engineering. I am particularly thankful for the expertise and recommendations Dr. Adrian Burd, our project collaborator, has shared with me, even though I am not lucky enough to have him become my graduate committee member.

Additionally, I would like to thank my friends, lab mates, colleagues and collaborators at Penn State and other research institutions. Dohwan is my best friend at this town and he is a great listener who is always available. Nicolas, Nick, Brandon, Adrain, Raj, and Reza are nice and trustworthy lab mates. The Rau boys are always patient and never complain

about my lengthy presentation. I must remember the friendship from other lab groups, and my unforgettable time on the ship (Daniel, Ahmed, Kieran, Austin, Kenny, and Alex). I also appreciate the help from the friendly staff at ME department, including but not limited to Julie, Ashley, Sandy, Chris and Jamie. I have also had so much help from other departments and groups at Penn State.

I am thankful for the funding support for my research through NSF grant OCE-1948283 and Penn State.

Everyone has shared the same three years of the pandemic. COVID is like God's rolling the dice, when everyone's life has been randomly changed forever more or less. During the pandemic era, friends, colleagues, and I suffered from different tough situations. Yet, most of them did not lose hope but had become stronger, in despite of traumas. Their examples and kind help from everywhere ultimately had shaped me into a more courageous person. I really appreciate my advisor, Dohwan, Haosen, Yawei, Xiaoling, Xiaoyue, Xinyi, Eric, and many other friends, who spent time with me and helping me get through the tough time. I understand there will be more frustrations occurring at me in the future, but their selfless help will be always kept in my mind.

Finally, I acknowledge the never-ending support from my family in China. I am grateful to my parents and grandparents, for their ceaseless encouragement, trust and understanding. Not seeing them for more than three years is the most regretful thing during my Ph.D. life, but we will reunite soon. I wish next time I can do a better job describing my research work and field trips. I will make you all proud.

I believe the completion of my dissertation is also a great karma. Every friend, every experience, and every choice eventually solidified my intent of pursuing a Ph.D. in the United States. Therefore, truly, I wish to thank every friend, every professor at SJTU and USC, and everyone in my life. “Flowers will bloom on the other shore”, written in calligraphy on my folding fan, was a gift from my friend more than ten years ago. I am hoping something extraordinary will eventually become reality on both shores of the Pacific Ocean.

Federal Funding Disclaimer: The findings and conclusions do not necessarily reflect the view of the funding agency.

Chapter 1

Introduction

1.1 Motivation

Aggregation is the process by which colloidal particles stick together to form large and fast-sinking particle clusters, typically called aggregates or flocs. Disaggregation is the reverse process, where an already-formed aggregate disrupts into sub-aggregates or primary particles. Together, aggregation and disaggregation act to govern particle size and transport properties in diverse applications, including dredging processes (Smith & Friedrichs, 2011), fouling in heat exchangers and air-handling equipment (Kim, 2018), drug manufacturing and delivery systems (Yang *et al.*, 2014), and many others. The aggregation of microplastics and nanoplastics is important to wastewater treatment (Hsu & Glasgow, 1983) and threatens the ecosystem (Carr *et al.*, 2016; da Costa *et al.*, 2016). Creating artificial oil-mineral aggregates can even mitigate the pollution of crude oil spills (K. Lee *et al.*, 2002), as oil in oil-mineral aggregates is dispersed more rapidly due to the enhancement of biodegradation processes (Weise *et al*., 1999). Specifically, organic flocs in the ocean, often known as marine snow, play an essential role in the global carbon cycle (Alldredge *et al.*, 1993). It is this last topic that has motivated the dissertation work, in that the aggregation theory of the large organic flocs in the ocean (marine snow particles) is relatively well understood (Alldredge & Silver, 1988; Burd & Jackson, 2009), but fragmentation processes have seen little investigation despite their apparent importance in the oceanic carbon budget (Briggs *et al.*, 2020). In particular, being able to predict and

parameterize fragmentation processes will necessitate understanding the balance between external hydrodynamic and internal adhesion forces, the latter of which is particularly complex given that marine snow mostly contains a mixture of biological and abiotic particles (Alldredge & Silver, 1988) and that our knowledge of biological cell adhesion is still limited (S. Li *et al.*, 2011; Mari *et al.*, 2017).

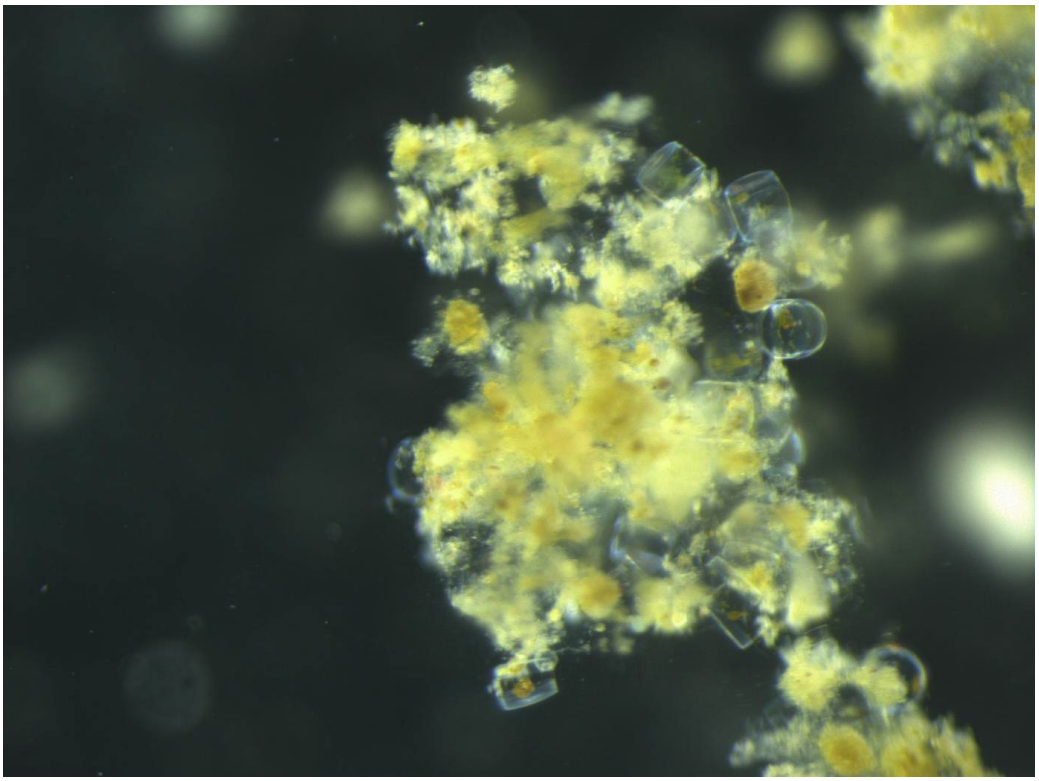

Figure 1-1: Natural marine snow aggregates containing diatoms (Durkin, 2015).

Human activities causes the increased amount of greenhouse gas emissions in the atmosphere (Salam & Noguchi, 2005; Yue & Gao, 2018). To mitigate the serious impacts of climate change (Kirilenko & Sedjo, 2007; McNutt, 2013; Tol, 2018; Wheeler & von Braun, 2013), lowering the CO_2 concentrations is required. Friedlingstein *et al.* (2022)

reported that the sinking process of CO_2 accounts for approximately half of the carbon uptake. Therefore, we cannot accurately predict climate change effects without knowing the marine carbon sequestration. Aggregated particulate organic matter in the ocean, known as marine snow (shown in Figure 1-1), makes up a large part of the oceanic sedimentary flux and is key to biological transformations in marine ecosystems (Kiørboe, 2001). In shallow waters, up to 63% of the particulate organic carbon can be contained within marine snow, the size of which can range from a few microns up to centimeters (Alldredge & Silver, 1988). Every year, approximately 10^{15} grams of carbon is pumped from the surface ocean to the deep sea by sinking marine snow particles (Middelburg, 2011; Muller-Karger, 2005). In the natural environment, the settling velocity of marine snow varies widely (Cael *et al.*, 2021) but has been observed to be as high as 0.43 cm/s (370 m d^{-1}) (Alldredge & Gotschalk, 1988). Figure 1-2 shows a schematic diagram of the biological pump (Renier & Durkin, 2016), in which phytoplankton capture CO_2 through photosynthesis and the settling and upwelling dominates the biological pump. These sinking particles are the primary source of carbon fixation in the ocean and this process significantly affects the concentration of CO_2 in the atmosphere (Kwon *et al.*, 2009).

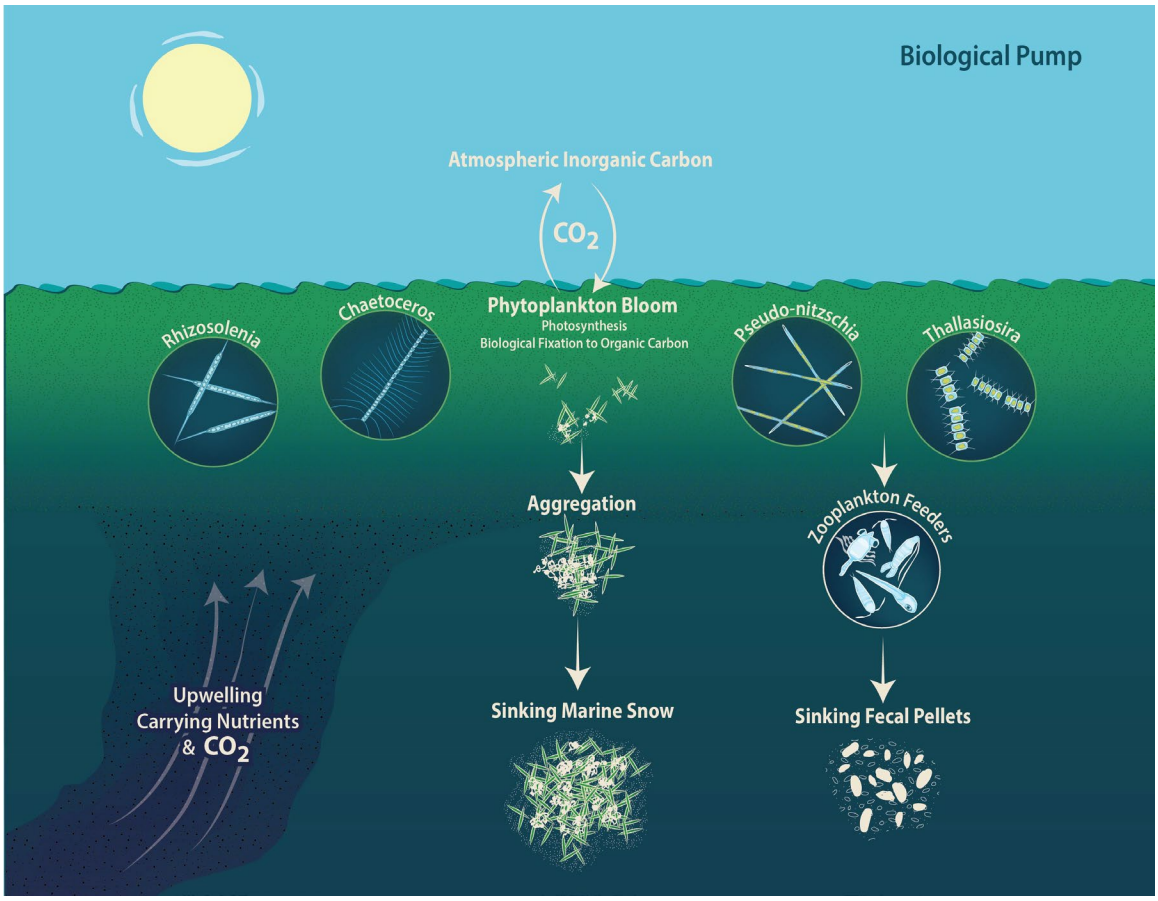

Figure 1-2: Schematic diagram of biological pump with carbon fixation in the ocean (Renier & Durkin, 2016).

However, carbon flux measurements have revealed an exponential decrease in this downward flux of organic materials with depth (Berger 1988), which has not yet been fully explained. Degradation of sinking particles caused by attached bacteria and the consumption by zooplankton are major sources of this decrease, but these processes alone do not fully explain the attenuation observed in the environment (Collins *et al.*, 2015). Fragmentation of large sinking aggregates into slower-settling sub-aggregates is one likely explanation that could help reconcile the carbon budget (Briggs *et al.,* 2020). Previous

studies (Jackson, 1994, 2015; Smayda, 1971) empirically proved the positive correlation of the settling speed of marine aggregates with their size, so fragmentation potentially plays an important role in the biological pump as well as aggregation in Figure 1-2. Along with carbon (C), transport of other nutrients and elements like nitrogen (N) (Gruber & Galloway, 2008) and silicon (Si) (Laruelle *et al.*, 2009; Struyf *et al.*, 2009) are also influenced by the aggregation and disaggregation process. While aggregation theory has been well developed (Alldredge & Silver, 1988; Burd & Jackson, 2009; Fowler & Knauer, 1986) and its influence on particle flux is represented in ocean transport models (Aumont *et al.*, 2015), fragmentation processes have not yet reached this same level of parametric understanding.

1.2 Theoretical Considerations

In this section, we summarize three theoretical frameworks relevant to the aggregate breakup strength: the population balance model aims to model the particle population considering aggregation and fragmentation processes subjected to varying hydrodynamic conditions; the subsection of marine aggregate strength discusses previous models for measuring the strength of flocs in turbulence; the bonding theory of colloidal dispersions provides the force analysis over charged microspheres in nanoscale or microscale.

1.2.1 Population Balance Model

Aggregation and fragmentation can be modeled through the one-dimensional population balance equation (PBE) (Burd & Jackson, 2009). The advantage of the PBE over more

complex particle-resolved models is that it can be easily coupled to larger ocean or computational fluid dynamics simulations for particle transport calculations. The PBE is given by

$$\frac{dN(m,t)}{dt} = A_i - A_o + B_i - B_o + W + S_{io}, \tag{1.1}$$

where N is the time-varying number distribution of particles of mass m. The number of particles in a population is governed by aggregation processes (denoted by the A terms), breakup processes (B terms), loss due to gravitational settling (W), and sources or sinks of particulate mass (S_{io}). Particle loss due to gravitational settling is typically defined through terminal velocity estimates. Source and sink terms can come from a variety of sources but are typically caused by growth and feeding of organisms for organic marine particles.

Aggregation rates depend heavily on particle type and the flow field and are typically modeled as

$$A_i = \frac{\alpha}{2}\int_0^m \beta_A\left(m_j, m-m_j\right) N\left(m-m_j,t\right) N\left(m_j,t\right) dm_j, \tag{1.2a}$$

$$A_o = \alpha N\left(m,t\right)\int_0^\infty \beta_A\left(m,m_j\right) N\left(m_j,t\right) dm_j, \tag{1.2b}$$

where A_i denotes the rate at which smaller particles aggregate into larger clusters of mass m while A_o describes the rate at which aggregates of mass m aggregate into flocs of even greater mass. Both aggregation rate equations are a function of a particle stickiness parameter (α) and the aggregation kernel (β_A). The aggregation kernel describes the frequency with which particles come into contact given their relative sizes and the surrounding hydrodynamics. Aggregation kernels are well established for both laminar and turbulent flow in the literature (Burd & Jackson, 2009).

Disaggregation has seen less agreement in the literature, especially for aggregates consisting primarily of organic material relevant to the open ocean (*i.e.,* phytoplankton and other organic microorganisms). The breakup terms of the PBE can be expressed as functions of the particle number distribution as

$$B_i = \int_m^\infty K\left(m_j\right)\Gamma\left(m, m_j\right) N\left(m_j, t\right) dm_j, \tag{1.3a}$$

$$B_o = K\left(m\right) N\left(m, t\right), \tag{1.3b}$$

where $\int_0^m m_j \Gamma\left(m, m_j\right) dm_j = m$ and Γ represents the size distribution of the aggregate mass. In the above equation, B_i is the rate at which larger aggregates break into smaller sub-aggregates of mass m and B_o is the rate at which aggregates of mass m disrupt into even smaller particles.

In order to develop disaggregation relationships for use in the PBE, we need to define the breakup frequency of aggregates as a function of their mass (K) for a wide range of hydrodynamic and particle conditions. In a turbulent fluid, hydrodynamic shear typically causes disaggregation. Parker *et al.* (1972) conducted an early attempt to theoretically define the breakup frequency (K) of aggregates in waste treatment processes. Their model agreed well with experimental data for inorganic aggregates but failed to agree with the measured disruption response of organic aggregates. A key limitation in this study was the assumption that sub-aggregates were not formed during disruption. Instead, only the shearing of primary particles from the aggregate surface was considered. Subsequent studies have often taken an empirical approach to developing aggregate disruption models, with breakup frequency equations being assumed to follow a power-law of the form $K \propto d^{\chi}$, where d is a relevant aggregate length scale (Jackson, 1995; Saha *et al.*, 2014;

Spicer *et al.*, 1996). A few attempts have been made to theoretically define *K* in Equations (1.3); however, these relationships still typically rely on some a-priori knowledge of the aggregate yielding strength (Hsu & Glasgow, 1983; Kusters, 1991).

It is clear from the above literature that despite our understanding of aggregation, the breakup response of aggregates, and in particular marine aggregates, is still poorly understood. Without a reliable mathematical explanation of breakup, the incomplete PBE limits our ability to thoroughly explain the biological carbon pump. Specifically, the breakup frequency *K* determined by the breakup strength in the breakup term *B* cannot be determined until we know the marine aggregate strength.

1.2.2 Marine Aggregate Strength

The complexity of determining the yielding strength of marine aggregates results from the composition, shape and fractal dimension *Df* (Alldredge & Silver, 1988). For discussion, the floc mass m_f is related to its size as, $m_f \propto d_f^{Df}$, where d_f is the characteristic length of the floc. A fractal dimension of $Df = 3$ represents a solid particle, while a lower value of the fractal dimension indicates a porous structure. Fractal dimensions of marine aggregates typically vary from 1.3 to 2.3 (Burd & Jackson, 2009).

Few studies have attempted to create a marine aggregate strength model. Rumpf (1962) considered the porosity φ of the aggregates and presented a simple model for the yielding strength of aggregate,

$$\sigma_y = 1.1\left[(1-\varphi)/\varphi\right]\left(F_1/d_1^2\right), \tag{1.4}$$

where F_1 and d_1 are the interparticle bond force and diameter of the primary particles, respectively. However, Equation (1.4) does not adequately explain variability in composition and aggregate shape. In the meantime, porosity of marine aggregates is thought to be determined by fractal dimension. Additionally, abundant transparent exopolymer particles (TEP) play a significant role in biogeochemical cycling of elements (Passow, 2002a), which also affects strength (Mari *et al.*, 2017). The ocean environment, including its PH values and salinity, complicates the problem further. For example, at lower salinity the fractal dimension of diatoms was shown to decrease (Vrieling *et al.*, 2007), which may cause a decrease in aggregate strength due to the higher expected porosity.

Hinze (1955) studied the splitting of globules through hydrodynamics, which inspired many researchers to quantify aggregate strength using a similar approach (Jarvis *et al.*, 2005; Rau *et al.*, 2018). The basic idea of the hydrodynamic method is assuming the aggregate yield stress is balanced by the hydrodynamic stress. This critical state of stress balance corresponds to the largest stable aggregate size d_{max} in the turbulent flow,

$$\sigma_y\left(d_{\max}\right) = P'\left(d_{\max}\right). \tag{1.5}$$

where P' is the gauge pressure difference acting across the aggregate. For reference, the size range of aggregates in natural systems varies from microns to a few millimeters (C. A. Durkin *et al.*, 2015).

The length scale of the aggregates is vital to this hydrodynamic problem. In turbulence theory, the Kolmogorov length scale of the flow, defined as $\eta_K \sim (\nu^3/\varepsilon)^{1/4}$ where ν is the molecular kinematic viscosity and ε is the energy dissipation rate, usually determines the length scale of the smallest turbulence structure. In the open ocean, the energy dissipation rate ε typically varies from 10^{-10} W kg^{-1} to 10^{-1} W kg^{-1} (Thorpe, 2005), which means that

the Kolmogorov length scale of turbulence can be as small as 60 μm. For particles that are smaller than the Kolmogorov length scale, they are under the viscous dissipation subrange of turbulence. For large aggregates, inertia dominates where the large scale flow motion needs to be considered. We should separately consider the cases for aggregates in the inertial and the viscous subrange for determining the critical breakup strength.

A turbulent flow typically can be characterized through the statistics of its velocity fluctuations. For aggregate breakup, the velocity fluctuations occurring at the length scales of the aggregate are most important (Hinze, 1955). Characteristic mean-square velocities of turbulence fluctuations acting over a distance d (*i.e.* acting across the aggregate) can be theoretically related to the bulk dissipation rate ε through:

Inertial convection subrange,

$$\overline{u'^2}(d) = C_0(\varepsilon d)^{2/3}; \tag{1.6a}$$

Viscous dissipation subrange,

$$\overline{u'^2}(d) = \frac{C_0}{2}\frac{\varepsilon}{\nu}d^2, \tag{1.6b}$$

where C_0 is a constant of ~0.5 (Pope, 2001). One potential cause of aggregate disruption is due to the differences in dynamic pressure caused by these differences in fluctuating velocities. The dynamic pressure difference across the aggregate is thus given by (Thomas, 1964),

$$P'(d) = \frac{1}{2}\rho_l \overline{u'^2}(d). \tag{1.7}$$

Combining Equations (1.5), (1.6a) and (1.7), we can derive the critical strength for maximum aggregate size in the inertial subrange of turbulence,

$$\sigma_y\left(d_{\max}\right)=\frac{1}{2}\rho_l\overline{u'^2}\left(d_{\max}\right)=\frac{1}{2}\rho_l C_0\left(\varepsilon d_{\max}\right)^{2/3}. \tag{1.8}$$

The above equation, thus, gives a direct measure for the yield stress of the largest aggregates in a population as long as d_{max} can be determined. Previous researchers applied this strength equation to quantify the breakup strength of varying aggregates (Hsu & Glasgow, 1983; T. Li *et al.*, 2007; Rau *et al.*, 2018), but it has not been applied to natural marine aggregates yet.

1.2.3 Bonding Theory of Colloidal Dispersions in Nanoscale and Microscale

Aggregates are ultimately held together through the primary bonds between individual particles. The classic Derjaguin–Landau–Verwey–Overbeek (DLVO) theory (Derjaguin & Landau, 1993; Verwey & Overbeek, 1948) explains the aggregation of colloidal dispersions and describes the forces between charged surfaces, which are often the relevant primary particle forces in aggregates. Exempt from biological interactions, this theory considers that the total free surface energy W_{DLVO} per unit area is a function of the separation distance l, and is simply the result of two additive contributions from van der Waals attractions (LW) and electrostatic repulsions (DL) (Israelachvili, 2011),

$$W_{DLVO}\left(l\right)=W^{LW}\left(l\right)+W^{DL}\left(l\right). \tag{1.9}$$

Equation (1.9) can model surface adhesion forces in the geometric configurations of two spheres, two parallel flat plates, and others.

Van der Waals forces result from interactions of the fluctuating dipoles of atoms and molecules (Israelachvili, 2011). This non-polar surface interaction decays very fast as a

function of the separation distance *l*. Van der Waals forces are always attractive for two identical particles or molecules immersed in the liquid (van Oss, 2008). For a geometric configuration of two parallel flat plates, the free energy of van der Waals can be written as

$$W^{LW}(l) = -\frac{A_H}{12\pi(l-l_0)^2}, \tag{1.10a}$$

while the van der Waals energy between two identical spheres of equivalent radius R_s is given as

$$W^{LW}(l) = -\frac{A_H R_s}{12(l-l_0)}, \tag{1.10b}$$

where A_H is the Hamaker constant (Hamaker, 1937) and l_0 is the minimum equilibrium distance (Israelachvili & McGuiggan, 1988). The Hamaker constant depends on the two substrates or particles and the intervening medium. Van Oss *et al.* (1988) determined the minimum equilibrium distance to be 0.157 nm.

Electrostatic repulsion is sometimes called electrical double layer interaction. It is important for charged particles or substrates, especially at low salt concentrations. The surface charge potential φ_0 is a function of the particle radius R_s and the distance z between the particle surface and the slipping plane (van Oss, 2008). It can be written as,

$$\varphi_0 = \zeta\left(1+\frac{z}{R_s}\right)\exp(\kappa z), \tag{1.11}$$

where ζ is called the zeta potential and κ is the inverse Debye length subjected to the aqueous solutions. The zeta potential is the electrical potential at the slipping plane that separates the moving fluid from the fluid attached to the charged surface (Israelachvili,

2011). The distance z between the particle surface and the slipping plane usually ranges from 0.3 to 0.5 nm. We write the inverse Debye length as

$$\frac{1}{\kappa} = \sqrt{\frac{\varepsilon kT}{4\pi e^2 \sum v_i^2 n_i}} \tag{1.12}$$

where k is Boltzmann's constant, T is the absolute temperature, e is the charge of an electron, v_i is the valency of each ionic species, and n_i is the number of ions of each ion. Next, we represent the double layer interaction energy as,

$$W^{DL}(l) = 2\varepsilon_1\varepsilon_0\kappa^2\varphi_0^2 \ln\left[1+\exp\left(\kappa\left(l_0-l\right)\right)\right], \tag{1.13a}$$

for the geometric configuration of two parallel flat plates. The electrostatic repulsion for two identical spheres is written as,

$$W^{DL}(l) = 2\pi\varepsilon_1\varepsilon_0\kappa R_s\varphi_0^2 \ln\left[1+\exp\left(\kappa\left(l_0-l\right)\right)\right], \tag{1.13b}$$

where ε_1 and ε_0 are the dielectric constant of water and the permittivity of free space, estimated to be 80 (at 20 °C) and 8.854×10^{-12} C/V·m, respectively (Elimelech *et al.*, 1995).

Van Oss (2008) claimed that Lewis acid-base forces (AB), known as polar interactions, also contribute to the total free energy of interactions between two surfaces of microspheres. Especially in water, the polar interaction energy is always present, where the electrical double layer force of the DLVO theory also applies. Therefore, he extended the classic DLVO theory to be the following,

$$W_{XDLVO}(l) = W^{LW}(l) + W^{DL}(l) + W^{AB}(l). \tag{1.14}$$

The Lewis acid-base theory accurately explains the interactions between solid substrate and the liquid medium, called hydrophobic attractions or hydrophilic repulsions. It has an exponential rate of decay with the separation distance. The Lewis acid base interaction is

a short-range force, and the working range is typically smaller than 8 nm in water solutions (Brant, 2002; van Oss, 2008). Van Oss (2008) proposed a model of exponential decay for this polar energy for the geometric configuration of two parallel flat plates,

$$W^{AB}(l) = \Delta G^{AB} \exp\left[(l_0 - l)/\lambda\right]. \tag{1.15a}$$

where ΔG^{AB} is the free polar potential energy for a geometric configuration of two parallel flat plates at minimum equilibrium distance, and λ is the decay length. For two identical spheres, the expression is given as,

$$W^{AB}(l) = \pi R_s \lambda \Delta G^{AB} \exp\left[(l_0 - l)/\lambda\right], \tag{1.15b}$$

The decay length for polar interactions in water is approximately 0.6 nm (van Oss, 2008).

All interactions described above are size and distance dependent, and the intermolecular forces have been validated in many colloidal studies (Boström *et al.*, 2006; Shams *et al.*, 2020; Sonntag & Russel, 1986). However, biological content complicates the problem of adhesion in marine snow aggregates. Notably, recent studies have found that transparent exopolymer particles (TEP) play a substantial role in forming marine aggregates (Azetsu-Scott & Passow, 2004; Mari *et al.*, 2017; Passow, 2002b). These organic, gel-like particles make it more difficult to quantify the adhesive force directly as their adhesive characteristics, and the molecular properties leading to those characteristics, are not yet understood.

1.3 Methods to Study Particle Aggregation and Breakup

1.3.1 Aggregation

The lack of knowledge of marine aggregate strength stems in part from the difficulty in accurately simulating and measuring its aggregation and disaggregation behavior in the laboratory. Fluid shear is responsible for breakup while there are diverse mechanisms for aggregation. McCave (1984) summarized the three main mechanisms by which particles come into contact and aggregate, which are Brownian motion, shear forces from laminar or turbulent flow, and differential sedimentation. Fluid shear and differential sedimentation are most relevant in the marine environment. Shanks and Edmondson (1989) introduced the concept of the roller tank to form marine aggregates in the laboratory. Aggregates were formed by flocculation of particles inside a cylinder filled with sea water and rotating with a constant angular speed. After an initial start-up period, shear within the fluid in the tanks dissipates and solid-body rotation of the fluid and particles persists. Any solid particles suspended in the flow continually settle and aggregate through differential sedimentation. The hydrodynamic response of these tanks with time, and their influence on particle aggregate formation, have been described in detail by Jackson (1994, 2015). Their design quickly became the standard method to form marine aggregates (Jackson, 1994), despite the lack of fluid shear.

Studies of marine aggregated particles are unique, in that the aggregated particles are typically quite fragile due to their formation in the marine environment (Alldredge *et al.*, 1990). To mimic natural marine snow particles in the laboratory, researchers often use the traditional rolling cylindrical tanks to cause aggregation of particulate matter through differential sedimentation (Shanks & Edmondson, 1989). Because the fluid motion in these

tanks follows solid body rotation, we cannot use them for disaggregation studies as there is no way to directly expose the marine snow particles to calibrated shear forces. Typically, researchers must manually extract the marine snow particles and then individually place them in a separate facility for breakup quantification process (Alldredge *et al.*, 1990; Saha *et al.*, 2016; Ziervogel *et al.*, 2020). This manipulation can disaggregate or alter the aggregates prior to measurement.

1.3.2 Laboratory Fragmentation Experiments

In natural systems like the ocean, particles and aggregates experience shear forces from the surrounding fluid flow, which can affect how they form and their ultimate size, shape, and density (McCave, 1984). It in turn governs settling velocity (Johnson *et al.*, 1996). For example, clay particles and phytoplankton in the ocean can deform or break apart by this fluid shear (Rau *et al.*, 2018; Tambo & Hozumi, 1979; Tomi & Bagster, 1980). The magnitude of shear rate G in the ocean can typically vary from 10^{-2} s^{-1} to 300 s^{-1} (Thorpe, 2005). Creating a controlled environment in the laboratory that can generate hydrodynamic shear at these magnitudes, while also allowing measurement of particle aggregation and breakup parameters, is not trivial.

Previous researchers have conducted laboratory breakup experiments in a simulated turbulent environment. Glasgow and Luecke (1980) studied the disaggregation of flocs in a turbulent environment and analyzed population statistics of particle size. Later, Rau *et al.* (2018) exposed bentonite clay flocs to varying turbulence and attempted to quantify their strength from the change in particle size spectrum. Alldredge *et al.* (1990) quantified the

breakup strength of collected natural marine snow using turbulence generated with an oscillating grid. Here, aggregates were collected, stored briefly, and then released individually into a turbulence tank. Ziervogel *et al.* (2020) similarly studied fragmentation of marine oil snow by first creating laboratory-made aggregates in a roller tank and then manually transferring the aggregates to a turbulence tank to observe fragmentation at different levels of turbulence intensity. Fuchs *et al.* (2004) used a similar grid-stirred tank to observe the sinking behaviors of marine gastropod larvae where they had to gently add samples into the tank before measuring larval movement. In addition to requiring manipulation of the particles by the researchers prior to measurement, the above cases also quantified shear rates using time-average values of energy dissipation rate. Measuring the instantaneous local shear forces acting on the particles was not possible. Goldthwait *et al.* (2004) analyzed the fragmentation of marine snow due to swimming euphausiids. To obtain local time-averaged fluid stresses caused by the feeding animals, they performed separate particle image velocimetry experiments using tethered animals, then assumed the shear magnitude was unchanged during animal interaction with an aggregate. In these works, researchers could not couple the time-varying responses of aggregates to local instantaneous hydrodynamic phenomena due to their time-averaged characterization.

In more detailed experiments, previous researchers have used various flow devices to resolve hydrodynamic conditions to study the local fragmentation of droplets and other types of particle aggregates. For example, laboratory observations captured droplet deformation and breakage in simple shear flows generated by a Couette device (Torza *et al.*, 1972; Williams *et al.*, 1997). With flow conditions determined analytically, the researchers could determine transient shapes and droplet bursting and their dependence on

instantaneous hydrodynamics. Saha *et al.* (2014, 2016) investigated the breakup of colloidal aggregates in an extensional flow using contracting nozzles and in-homogenous isotropic turbulence with three-dimensional particle tracking velocimetry (3D-PTV) techniques. They measured velocity gradients to determine the local fluid stress at the instant of individual aggregate breakup. The spatially and temporally resolved data from the above experiments have provided unique insights into the morphological evolution of droplets and aggregates exposed to hydrodynamic shear. The need exists for a facility that enables high numbers of detailed fragmentation measurements like those described above to clarify the fragmentation dynamics of marine aggregates. Due to their fragile nature, avoiding aggregate manipulation after formation is also desirable as handling can alter morphology and strength.

Franks *et al.* (2022) measured turbulence intensities in the open ocean and found that most observed turbulence was characterized by a small dissipation rate. In particular, at a depth of 150 m, over 99% of dissipation rates were less than 10^{-7} W/kg. However, Alldredge *et al.* (1990) fragmented phytoplankton aggregates using dissipation energy of great than 10^{-6} W/kg, which represented relatively rare hydrodynamic conditions in the open ocean. The limited laboratory experiments thus far implemented cannot yet establish the relative importance of disaggregation in the ocean. More laboratory facilities that can expose aggregates to shear relevant to the low turbulence in the ocean are needed.

1.4 Laminar Shearing Device Using Stokes' Second Problem

To mimic natural marine snow particles in the laboratory, researchers often use rolling cylindrical tanks, which cause aggregation of particulate matter through differential sedimentation (Shanks & Edmondson, 1989). Using the same tank, we can create an oscillatory flow by superimposing a harmonic oscillation to the tank wall. A time-varying shear stress inside the boundary layer can expose aggregated marine particles to fluid shear. This configuration is an extension to the famous Stokes' second problem but in the cylindrical geometry.

Stokes' second problem is one of the famous exact solutions to the Navier-Stokes equations (Herman Schlichting, 1979). Originally analyzed by G.G. Stokes (1850) and later by Lord Rayleigh (1911), the problem is one in which an infinitely long flat wall oscillates harmonically in a fluid. Because of the no-slip boundary condition and viscosity, the fluid near the wall follows a harmonic motion that is parallel to the wall. As a result, the velocity profile of the fluid is similar to that of a damped harmonic oscillation, where layers within the fluid can be identified based on their phase lag with the wall oscillation.

Since the original quasi-steady solution, this laminar oscillating flow has been described by only a few additional analytical investigations. Erdogan (2000) provided an exact solution for an infinite flat plate considering a stationary start where the wall motion started from rest. His result included a transient term and a quasi-steady term. The transient term decayed rapidly within a few cycles of boundary oscillations and had the same expression of quasi-steady state that was originally developed by Stokes. Li & Marfatia (1971) provided the expression for Stokes' second problem for flow on the outside of a cylinder with a harmonically oscillating rotation. Rivero *et al.* (2019) later analyzed this analytical

solution and conducted experiments to validate their results. Both results consisted of a transient solution for a stationary starting condition and a quasi-steady solution similar to Stokes' classical formulation. They showed that the dimensionless quasi-steady oscillatory flow on the outside of a cylinder was smaller in magnitude compared to a flat plate when the cylinder was small, but that the solution converged rapidly to the flat plate solution in both transient and quasi-steady terms as the radius of the cylinder increased. Von Kerczek and Davis (1974) and Hall and Stuart (1978) have also used linear stability theory to predict the limiting conditions for these quasi-steady analytical solutions for flat plate and external cylindrical geometries, respectively.

Due to its applicability to only laminar flows with an oscillating boundary, Stokes' second problem has seen limited application outside of the above-mentioned studies. Ai and Vafai (2005) theoretically extended Stokes' second problem to three different types of non-Newtonian fluids in contact with an oscillating flat plate. Their results showed that the magnitude of the fluid velocity was highly dependent on the non-Newtonian fluid behavior, which they captured using appropriate models. Flows generated by an oscillating wall have also had applications related to plasma actuators, where Hehner *et al.* (2019) developed a novel oscillatory plasma actuator by forming a Stokes layer. Their results indicated a potential application to turbulent drag reduction.

Fluids in contact with the inner surface of a moving cylinder, for example liquids in some coating processes (for example see (R. E. Johnson, 1988; Tirumkudulu & Acrivos, 2001)) or water rolled for particle content analysis in cylindrical tanks (Shanks & Edmondson, 1989) offer a unique potential application of Stokes' second problem. In this geometry, the fluid is contained inside of an outer moving cylindrical wall. The analytical

solution for the fluid motion subject to an outer cylindrical boundary oscillation, which is opposite the problem solved by Li & Marfatia (1971), is currently absent from the literature.

1.5 Research Objectives and Tasks

Marine snow is aggregated particles consisting of phytoplankton, inorganic minerals, and organic debris (Alldredge & Silver, 1988). Due to the material content and complex ocean environment, the strength of marine snow is poorly understood. Field measurements are challenging but necessary, as direct in-situ measurements of marine snow exposed to turbulence can provide evidence of breakup due to turbulence. At the same time, creating a controlled environment in the laboratory that can generate hydrodynamic shear at similar magnitudes to the ocean is necessary to provide detailed measurement of particle aggregation and breakup parameters.

This dissertation aims to develop field and laboratory methods to better our understanding of aggregate strength and fragmentation. The research objectives and tasks are outlined as follows.

Objective 1: Improve and develop a new in-situ disaggregation system.

Task 1.1 implement and verify the system with autonomous control during field deployments.

Task 1.2 confirm the existence of aggregates and fragmentation in the ocean.

Objective 2: Design a laboratory facility for studying disaggregation.

Task 2.1 develop an experimental facility that has a controlled fluid flow that exposes formed aggregates to calibrated hydrodynamic shear forces. Then calibrate the flow using analytical, experimental, or numerical methods.

Task 2.2 create phytoplankton aggregates in the laboratory and expose them to hydrodynamic forces.

Task 2.3 Capture breakup events using high-speed imaging techniques and develop an image processing method to automatically analyze a large number of breakup events.

Objective 3: Characterize the breakup strength of laboratory-made aggregates.

Task 3.1 develop a force balance model to predict the fluid force on aggregates.

Task 3.2 characterize the disaggregation of a wide range of aggregate materials, including algae and microplastics.

Task 3.3 use XDLVO theory and microplastic particles to estimate the cohesive force within algae aggregates.

Task 3.4 clarify the effects of biological bonding in algae aggregates by comparing the morphology and breakup behaviors of marine snow to flocs of plastic microspheres.

1.6 Dissertation Contents and Structure

The remainder of the dissertation is structured in the following manner. Chapter 2 addresses tasks in Objective 1. This chapter summarizes the development of an in-situ disaggregation system and its initial deployment in the field. This chapter reviews the

concept of exposing natural aggregates to controlled turbulent pipe flows and describes the improvement over the original facility developed by Ackleson and Rau (2020). We implemented fragmentation experiments in two field deployments to the Northeastern United States Continental Shelf (CS) and Lake Tahoe. The deployment in the Northeastern United States CS captured digital holographic pictures of phytoplankton and marine snow aggregates. The deployment additionally provides evidence of aggregate fragmentation in the mixed layer. The fragmentation results in Lake Tahoe show the significance of particle aggregation in a freshwater system.

Chapter 3 addresses the first two tasks in Objective 2. In this chapter, we first provide an analytical solution to a viscous oscillatory flow inside a cylindrical tank that undergoes a harmonic oscillation along its axial direction. The laminar flow is an extension of the famous Stokes' second problem, and we perform a particle image velocimetry experiment to verify the analytical solution. Based on the flow condition, we designed a disaggregation tank by rotating and oscillating a cylindrical tank. This chapter then describes the operation of the tank and evaluates the fluid shear created. Assuming a constant settling speed, we calculated particle trajectories and assessed the stable region where particles will have no wall contact during an experiment.

Chapter 4 addresses Tasks 2.3 – 2.5. We develop a high-speed imaging method to couple the hydrodynamic force with the particle breakup. This chapter describes the imaging processing algorithm that tracks particles and detects breakup events. We present in this chapter the formation of laboratory aggregates and investigate the morphological evolutions prior to individual fragmentation events. Chapter 4 also provides the assessment and outlines the advantages of the new method. Additionally, we introduce a version of the

method that can be used to study time-varying particle population statistics, which reflects the fragmentation rate and enhances our understanding of fragmentation.

Chapter 5 addresses tasks in Objective 3, and presents the fragmentation experiments of four different material types. We create two types of plastic colloidal flocs and compare their breakup behaviors with laboratory-made diatom aggregates. We perform a bonding force calculation for plastic flocs based on the XDLVO theory and estimate the adhesive strength within phytoplankton aggregates. This chapter also develops a simple force balance model for measuring the breakup force from the hydrodynamic conditions. Lastly, we discuss porous structures and viscoelastic behaviors of aggregates.

Finally, Chapter 6 presents the major conclusions of the entire dissertation work. It also addresses the major research contributions and recommendations for future work.

Chapter 2

In-situ Measurements of Disaggregation of Naturally Occurring Aggregates

As previous laboratory work (Alldredge *et al.*, 1990) could not provide comparable turbulence dissipation rates to the ocean, the implementation of fragmentation experiments due to oceanic turbulence is needed. This chapter describes the in-situ method we developed for the disaggregation measurement. We have applied this facility with autonomous control in two recent field deployments, the Northeastern United States CS and Lake Tahoe. The field deployment in the Northeastern United States CS took place in April and May 2022, and we had another collaboration deployment in Lake Tahoe in September 2022. Results from both deployments have proved the existence of naturally occurring aggregates and disaggregation due to turbulence. Work in this chapter will be compiled with collaborators and then submitted to journal publications.

This chapter is organized into three subsequent sections. In Section 2.1, we describe the development of the in-situ disaggregation system, implement the concepts with autonomous control, and implement calibrations of the turbulence dissipation rates. Section 2.2 discusses the preliminary results collected by our disaggregation system and the holographic analysis of natural marine particles. Section 2.3 summarizes our findings and addresses the future directions with supplemental data collected with our collaborators.

2.1 Development of the In-situ Disaggregation System

2.1.1 Concepts and Designs

Rau *et al.* (2018) described the concept of exposing formed clay flocs to a turbulent pipe flow with varying energy dissipation rates. They set up two tanks with different heights to create a constant hydrostatic pressure difference between the two ends of the tube. The fluid flow inside the tube could reach a laminar state or varying turbulence intensities by adjusting the hydrostatic pressure difference. This study observed that high turbulence intensities could cause bentonite clay flocs to fragment into smaller aggregates. Later, Ackleson and Rau (2020) applied a similar idea and developed the original in-situ disaggregation system (iDAS) for measuring the disaggregation of natural marine aggregates in the coastal region or surface water. They used one underwater thruster to draw the fluid flow passing through a particle size meter (LISST-100X) to measure the size spectrum of natural marine particles. The LISST (Laser In Situ Scattering and Transmisometery) software adopts the laser scattering methods originally developed by Agrawal *et al.* (2000, 2008). These techniques use Mie-scattering theory of particles with regular shapes to obtain the particle size from the small angle laser scattering. The original iDAS successfully captured the particle size variability with different flow conditions. However, the measurement was limited to the ocean surface due to the cabled system, which was about 20 m only. We are interested in the microscale physics in the mixed layer in which the depth can reach more than 50 m. Additionally, the size of natural marine snow aggregates can reach up to a few millimeters (Alldredge & Silver, 1988), but the size measurement range of the LISST-100X only has an upper limit of 200 microns. Both needs,

greater detection depth and larger measurement size range, required us to develop an upgraded iDAS.

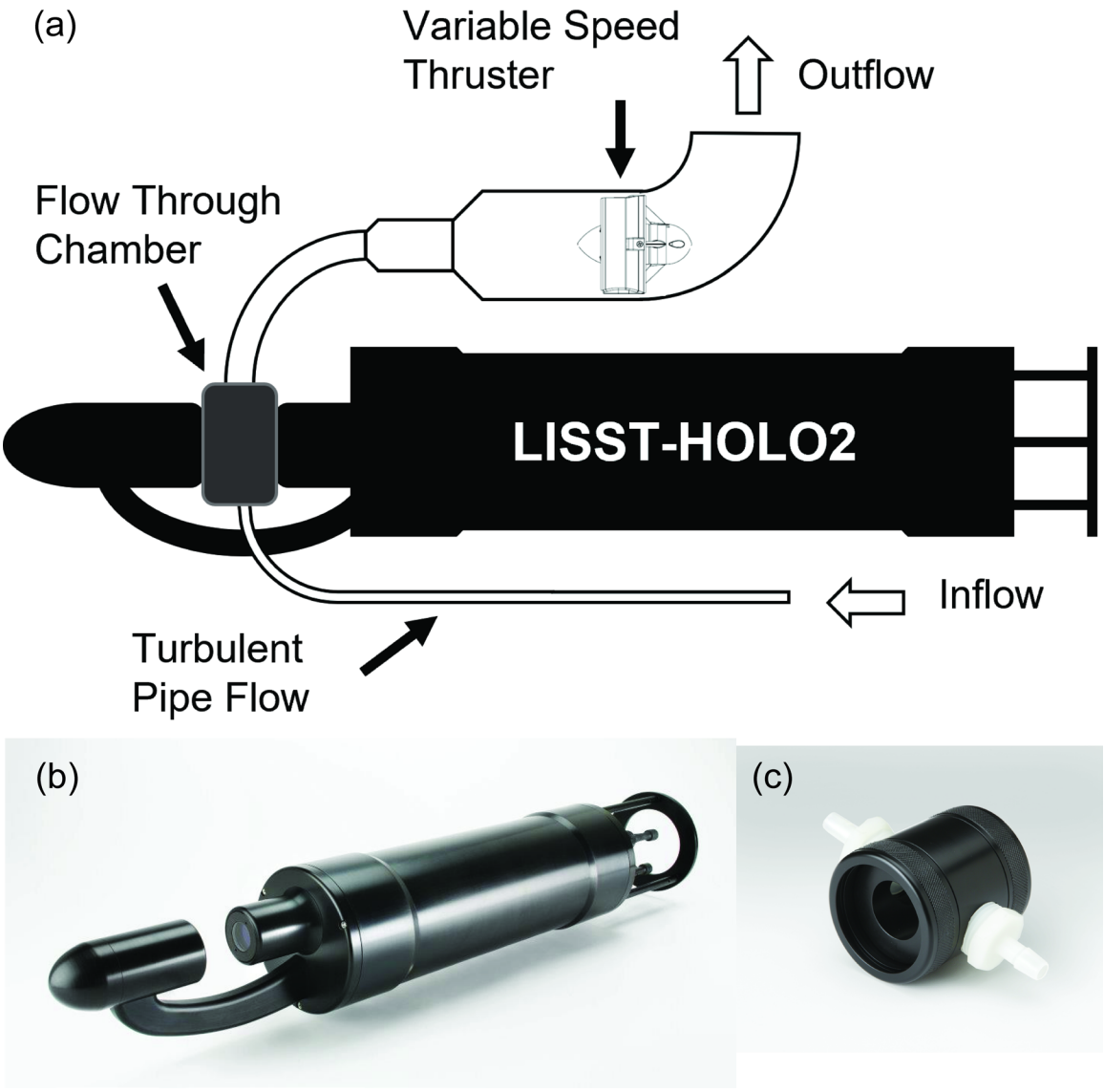

Figure 2-1: (a) schematic diagram of the in-situ disaggregation system attached to a LISST-HOLO2 submersible digital holographic camera, and pictures of (b) LISST-HOLO2 and (c) the flow-through chamber (Sequoia Scientific). The tube has an inner diameter of 12.7 mm and a length of 3.048 m.

Figure 2-1 shows the schematic diagram of the new iDAS attached to a submersible digital holographic camera, LISST-HOLO2 (Sequoia Scientific). The LISST-HOLO2 emits a red laser (658 nm) across an open sample volume and captures the light interference pattern of all suspended particles within the laser beam. Proper reconstruction procedures (self-developed reconstruction code or embedded programs LISST HOLO Batch and HOLO Detail) can generate particle images and particle size statistics. The operation reconstructs the light intensities as a function of depth, allowing to image in-focus particles across its 50 mm-long sample volume (Graham & Nimmo Smith, 2010; Malkiel *et al.*, 2004). The size range is from 25 μm to 2,500 μm, which covers most phytoplankton cells and naturally occurring marine aggregates.

The new iDAS applies the same concept as the original version (Ackleson & Rau, 2020), using a variable speed thruster (T200, Blue Robotics) to create different flow rates inside the tube. The tube has an inner diameter of 12.7 mm and a length of 3.048 m (l_t/d_t = 240). Therefore we can assume the turbulent flow inside the tube achieves fully-developed conditions (Bakewell & Lumley, 1967). We will describe the flow conditions and calibrations in the following sections. The tube connects to a small flow-through chamber shown in Figure 2-1(c) (SEQ-AC-LHO-CHFP, Sequoia Scientific), which is sealed tightly with two O-rings to the measurement end of the LISST-HOLO2 (the left side of Figure 2-1(b)). This chamber completely encloses the measurement end of the instrument and creates a closed flow path for the particle samples. The other end of the flow through chamber was connected with a PVC pipe. The PVC pipe with a large diameter and a moderate strength had the outlet face towards the opposite direction of the inlet, which

minimized the influence from the outlet flow. Near the outlet was installed an underwater thruster in a PVC pipe. The T200 thruster is a three-phase, brushless motor controlled by an electronic speed controller (ESC, Blue Robotics). The speed and direction of the motor can be controlled by providing varying pulse-width modulation (PWM) signals to the electronic speed controller.

The original iDAS required a manual control onboard to transmit the PWM signal to the ESC. The cable limited the maximum depth for the measurement. To study the disaggregation in a wide range of depths, we implemented an Arduino-based control system for the new iDAS. The electronic hardware was sealed inside two aluminum enclosure tubes (3" series, Blue Robotics) and consisted of a motherboard (Arduino Mega 2560 Rev3, or Arduino Uno R3), a real time clock (RTC) (PCF8523, Adafruit), a pressure and temperature sensor (BAR30, Blue Robotics), and a micro SD card breakout board (Adafruit). Each enclosure tube had an inner diameter of 75 mm and a length of 240 mm and could withstand hydrostatic pressure of up to 950 m depth in the ocean. A 9 V alkaline battery supplied the power to the Arduino board underwater. We uploaded a program with speed variations and time control into the mother board through the Arduino IDE (integrated development environment). The Arduino board then generated PWM signals for programmed time intervals to control the variable speed thruster. Appendix G contains the wiring diagram with the pinout connections of all sensors on an Arduino Mega board.

2.1.2 Flow Calibrations

Bakewell and Lumley (1967) provided the expression for the average turbulence dissipation rate in a fully-developed pipe flow by assuming the mechanical work done by the wall shear stress is fully transferred to turbulence dissipation energy. The average turbulent kinetic energy dissipation ε can be written as,

$$\varepsilon = \frac{\tau_w \bar{u}}{\rho d_t / 4}, \tag{2.1}$$

where τ_w is the shear stress at the tube wall (H. Schlichting, 1979), $\bar{u}$ is the average flow velocity, ρ is the fluid density, and d_t is the inner diameter of the tube. The experimental results of τ_w inside a tube are related to the Reynolds number $\mathrm{Re} = \bar{u} d_t / \nu$, which agrees with the Blasius correlation. We can rewrite the expression as a function of the flow velocity,

$$\tau_w = 0.03325 \rho (\bar{u})^{7/4} \nu^{1/4} \cdot \left(d_t / 2\right)^{-1/4}. \tag{2.2}$$

Equations (2.1) and (2.2) can thus predict the energy dissipation rates inside the tube if we know the volumetric flow rate inside the tube, which is controlled by the PWM signal we input to the thruster.

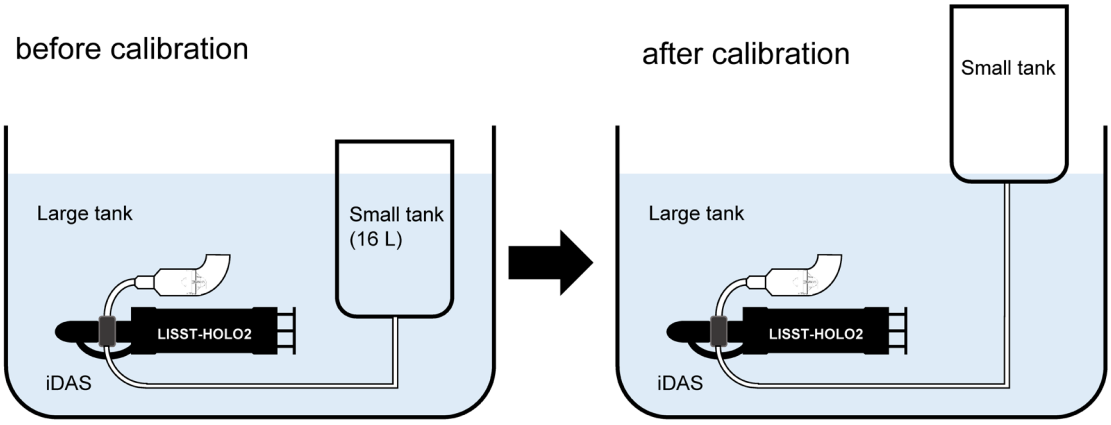

Figure 2-2: Schematic diagram of flow rates calibration. The left and right panels show different water levels in the small tank before and after the calibration.

Figure 2-2 schematically shows a dual-tank experiment to calibrate flow rates (Ackleson & Rau, 2020). First, we submerged the entire iDAS in a large tank filled with artificial seawater (Instant Ocean). We prepared a smaller container and drilled one hole at the bottom. This hole was connected to the open end of the iDAS tube. Next, we filled the small container with 16 L of the same seawater and partially submerged it so that the free surface of the water inside the container was the same as the water level of the large tank (left and right panels in Figure 2-2), thus creating no hydrostatic difference between the two containers. The thruster would draw the water from the small container into the large tank. During the calibration, we continually adjusted the position of the small container to maintain a free surface that was always identical to that of the large tank to minimize the hydrostatic pressure difference between the two ends of the iDAS. For a given PWM

signal, we calculated the average flow velocity $\bar{u}$ inside the tube based on the total time t_c required for drawing V_b = 16 L of water from the container,

$$\bar{u} = \frac{4}{\pi d_t^2} \frac{V_b}{t_c}. \tag{2.3}$$

The calibration was subjected to a few uncertainty sources. The T200 thruster has an open-loop control such that there is no feedback from the thruster. Additionally, manually adjusting the free surface of the bucket could also cause some errors. To minimize the uncertainty, we repeated each sampling speed three times.

Figure 2-3 shows the calibration using the iDAS and the flow through chamber compatible with LISST-HOLO2. We used a quadratic regression to fit an empirical relation between the PWM signal and the flow rate. The second-order polynomial, least-squares regression expresses as $\bar{u} = -3.334 \cdot 10^{-5} PWM^2 + 0.0628 PWM - 20.220$. The Pearson product-moment correlation was 0.945, which showed a very high quality of fitting. The maximum flow rate was approximately 1.1 m/s (9 L/min) corresponding with a dissipation rate of 1.6 m^2/s^3. We installed one customized honeycomb flow reducer after the outlet of the flow through chamber. This configuration would cause a Reynolds number inside the tube smaller than 2,300 at a PWM signal of 1450, which was a laminar flow. The smallest flow rate was approximately 0.7 L/min. At the flow rate of 1.6 L/min (PWM = 1425), the dissipation rate was 0.016 m^2/s^3. Therefore, we could vary the flow inside the tube from laminar state to a dissipation rate much higher than the surface ocean. During storms, the turbulence kinetic energy can reach up to 0.1 m^2/s^3 (Thorpe, 2005).

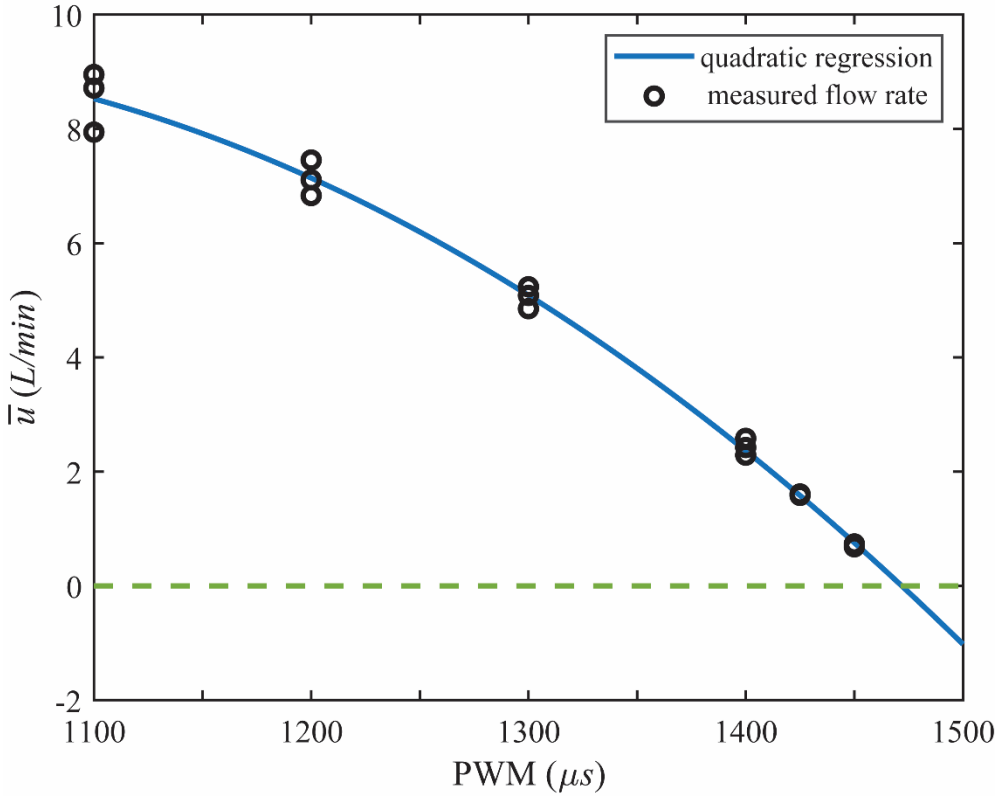

Figure 2-3: Flow rate calibrations as a function of PWM signal. The solid-blue curve represents the quadratic regression, and the green dashed line represents the zero flow rate. The second-order polynomial regression equation is $\bar{u} = -3.334 \cdot 10^{-5} PWM^2 + 0.0628 PWM - 20.220$.

2.1.3 Field Implementations

We have implemented the new iDAS during a cruise to the Northeastern United States CS. The new iDAS could reach a depth up to 200 m. We deployed the package shown in Figure 2-4(a) and ran the automated program to conduct disaggregation measurements at depth. Activation of power on the Arduino board triggered the program. Table 2-1 shows

a sample time series of thruster speeds when we deployed the iDAS. There was a delay of five minutes (sometimes ten minutes, depending on the measurement depth). During the delay, the iDAS underwent a flushing process using the highest thruster speed to eliminated air bubbles trapped inside the tube. Each thruster speed also had a specific time interval for measurement. The measurement for each speed required another prior flushing process, to eliminate particles exposed to the last flow condition and staying in the tube with the flow-through chamber. We programmed the flushing process using the same thruster speed and the flushing time based on the flow rate such that the volume of flow during the flushing was at least three times the total volume of the tube with the flow through chamber. We also required the flow volume of each measurement to be similar to each other so that we obtained similar samples for statistical analyses. The sample program lasted 65 minutes from its start until we finished the last measurement using the highest turbulence dissipation rate. With a sampling rate of 2 Hz, we captured approximately 1,680 holograms during the measurement time at the lowest thruster speed. The highest speed only recorded 240 holograms but had a similar sampling volume.

Table 2-1: Time series of programmed thruster speeds during a single cast of iDAS. The experiment started (Arduino was powered) at t_e = 0, and there was a 5 min buffer time waiting for the package to get to depth (t_e = 5 min).

PWM signal (µs)	**Dissipation rates ε (m^2/s^3)**	**Flushing time t_f (min)**	**Measurement time t_m (min)**	**Experiment time t_e (min)**

1450	Laminar	5	14	10-24
1425	0.016	3	7	27-34
1400	0.049	2	5	36-41
1375	0.104	2	4	43-47
1350	0.182	2	3	49-52
1325	0.279	2	3	54-57
1300	0.396	2	2	59-61
1100	1.633	2	2	63-65

Ackleson and Rau (2020) mentioned a few additional problems with the deployment of the original iDAS. The original iDAS with a LISST-100X particle size meter could measure particles from 1.09 μm to 184 μm, which could not cover the size of marine snow aggregates. Also, due to unknown upwellings or circulations, the total particle volume fraction could depend on ambient flow conditions in the ocean. Therefore, a significant improvement would be to measure the ambient particles at the same time. This would allow separation of disaggregation signals from bulk changes in ambient particle population.

In order to measure larger marine snow with ambient particles, we prepared the instrument package shown in Figure 2-4. Figure 2-4(a) shows a picture onboard the ship, and Figure 2-4(b) is the schematic diagram showing each instrument and sensor. On the top left is the original iDAS attached to a backscatter sensor (ECO Triplet, Sea-Bird Scientific) borrowed from the Naval Research Lab. The old iDAS was used to investigate the variation of backscattering signals in the upper mixed layer when subjected to different turbulent flow conditions. We attached and deployed this cabled instrument only for

surface measurements and separated it from the package for deeper deployments. On the top right Figure 2-4(b) is the new iDAS attached to a LISST-HOLO2. We deployed this iDAS attached to a second LISST-HOLO2 and a LISST-100X with a backscatter sensor (ECO Triplet, Sea-Bird Scientific) to measure the ambient particles. The combination of LISST-100X and LISST-HOLO2 was able to measure particle statistics with a size range from 1.84 μm to 2500 μm. The two backscatter sensors obtained measurements of turbidity and changes in bulk suspended particle concentrations.

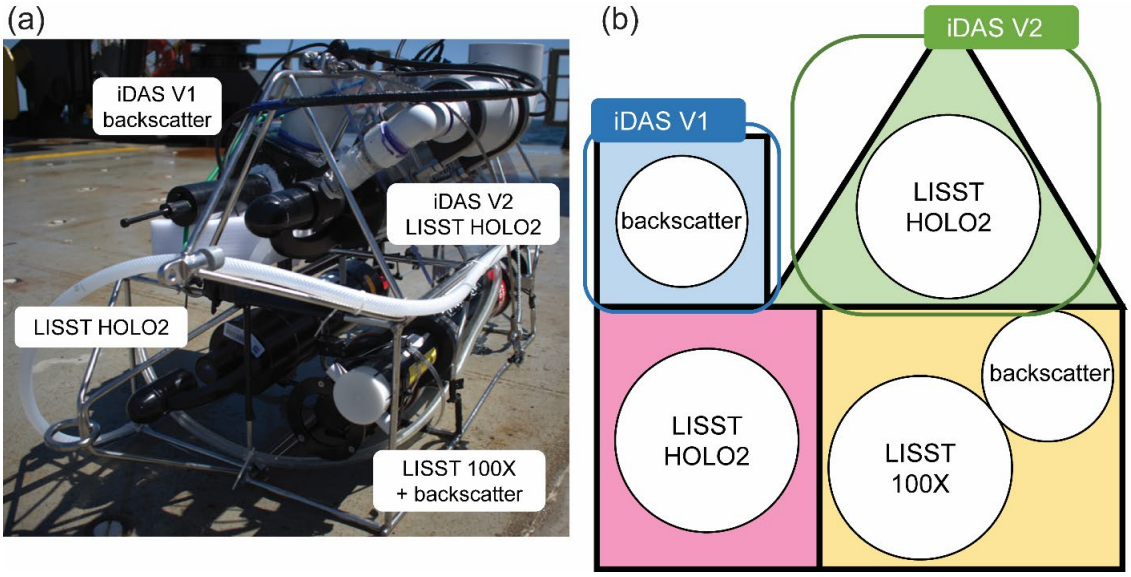

Figure 2-4: (a) picture of the in-situ instrument package during the deployment in the Northeastern United States CS, and (b) schematic diagram of the package. There were four separate in-situ instruments, the old iDAS attached to a backscatter sensor on the top left, the new iDAS on the top right, a LISST-HOLO2 submersible digital holographic camera on the bottom left, and a LISST-100X particle sizer with a backscatter sensor on the bottom right.

2.2 Aggregates and Fragmentation in the Natural System

2.2.1 Hologram Reconstruction

Digital in-line holography (DIH) is a 3D imaging technique that applies the light wave front information instead of capturing the projected image of an object (Falgout *et al.*, 2019; Xu *et al.*, 2002). It captures two-dimensional diffraction patterns of particles with a collimated laser and numerically determines the focal planes of particles. HOLO Batch is the default program developed by Sequoia Scientific for processing holograms captured by LISST-HOLO2. It automatically generates a montage image of all focused particles, as shown in Figure 2-4, with a particle size distribution of all processed particles. Graham and Nimmo-Smith (2010) originally developed the prototype of the LISST-HOLO2 and a fast and simple method (the original code for HOLO Batch) to determine the best focal plane for each particle. The algorithm first applies a median filter of 3 × 3 pixels to remove speckle noise. Then they segment the raw hologram after an image binarization using the Otsu threshold (Otsu, 1979). They assume that each segmented image has only one primary particle of interest. Last, they determine the best focus within the region of interest when the sum of all pixels' intensities reaches the global maximum over imaging depth.

The particle image reconstruction is the second major step and applies the algorithm developed by Owen and Zozulya (2000). The summarized reconstruction procedures have four main steps. The algorithm first transforms the image captured by a CCD camera into the Fourier domain and obtains the Fourier coefficients. Then it filters out the central Fourier components, which relate to the undistracted part of the reference laser beam. This

step enhances the contrast and sensitivity of the reconstruction. Next, they propagate the Fourier harmonics to the original position of the real image. The original position represents the best focal plane along the camera's viewing axis. The last step applies the inverse Fourier transform over the image from the frequency domain to the intensity domain.

Figure 2-5(a) shows a hologram captured at a depth of 190 m, at the station near the Hudson Canyon (39.46 N 72.30 W) on May 1st, 2022. We manually reconstructed the hologram at a focal depth of 30 mm. In the middle is one in-focus aggregate with sharp edges shown in Figure 2-5(b). This image revealed the existence of aggregates at a depth of 190 m. This aggregate image is only 2D but provides more details, including the structures of individual cells. Other interference patterns in Figure 2-5(a) are other out-of-focus particles. It is noted that two interference patterns near the top and bottom of Figure 2-5(a) likely result from the nonuniformity of salinity and temperature, as we manually confirm there are no particles in both regions. Sudden changes in salinity and temperature underwater due to small scale circulations can alter the refractive index causing interference fringes in the holograms.

Following the particle autofocusing (Graham & Nimmo Smith, 2010) and the reconstruction (Owen & Zozulya, 2000), another processed hologram in Figure 2-4(c) shows a few diatom cells (in the leftmost square) and chain-forming diatoms (in the red ellipse). This hologram was collected at the station near the Georges Bank (41.48 N 67.43 W) on April 25th, 2022. We also observe solid particles with irregular shapes (in the rightmost two squares in Figure 2-5(c)). They are likely natural aggregates consisting of minerals and phytoplankton. However, the quality of the image reconstruction is not as

satisfactory as Figure 2-5(b). For example, the algorithm divides the chain-forming diatom (in the red ellipse) into a few particles, so a few pseudo small particles will replace a real chain-forming diatom, thus affecting the particle size statistics. Despite the error, HOLO Batch in general works for capturing most particle shapes and can provide estimated particle size distributions. A new reconstruction method is favored to improve the image quality and extract more accurate particle size and morphology information.

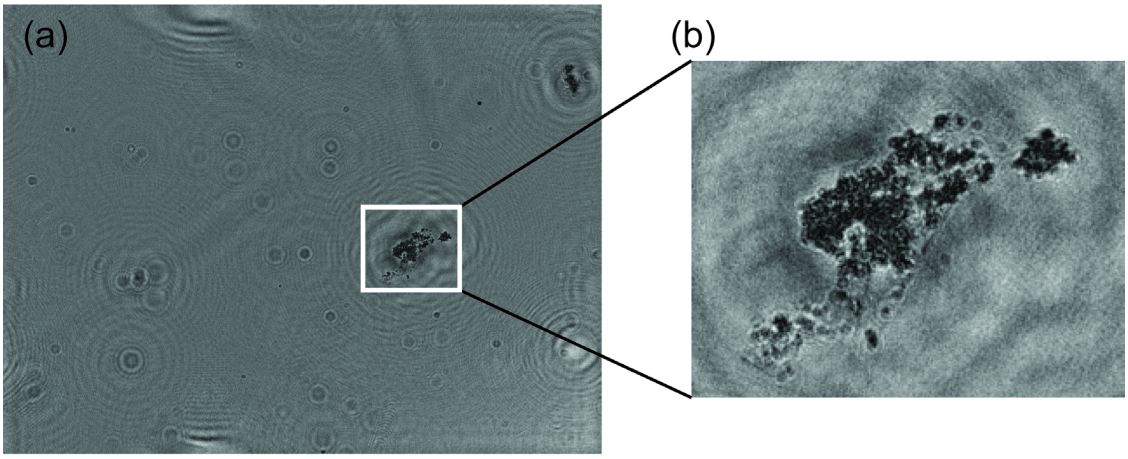

(c)

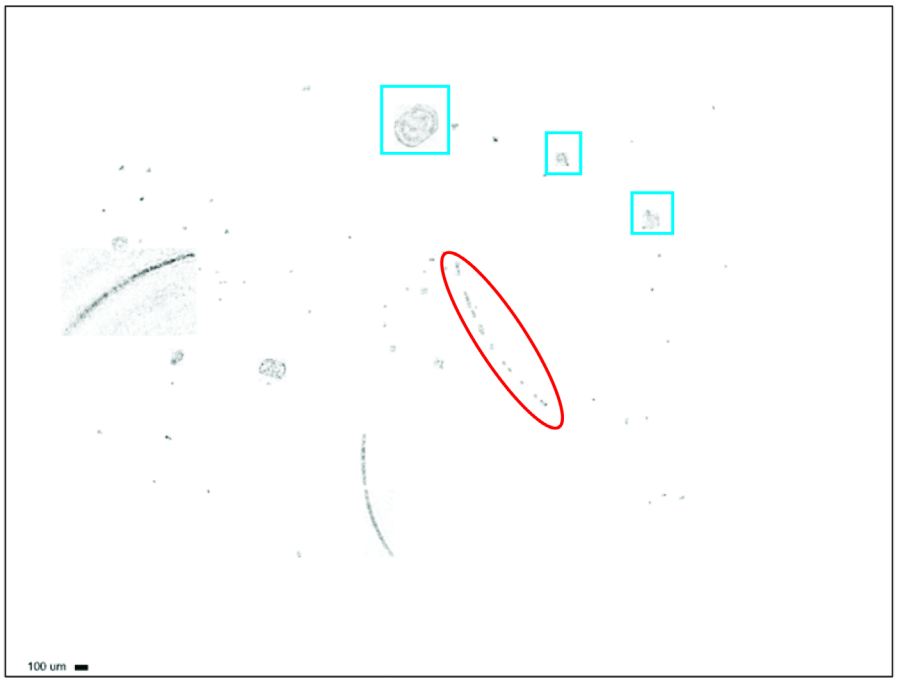

Figure 2-5: (a) sample hologram with a reconstruction depth of 30 mm, (b) an in-focus marine aggregate, and (c) sample reconstructed hologram processed by HOLO Batch (Sequoia Scientific). The hologram in (a) was captured at the station near the Hudson Canyon (39.46 N 72.30 W) on May 1st, 2022 and the hologram in (c) was collected at the station near Georges Bank (41.48 N 67.43 W) on April 25th, 2022. The scale bar represents a length of 100 μm and each pixel equals 4.4 μm.

2.2.2 Evidence of Aggregates Breakup in the Northeastern United States Continental Shelf

We have processed particle size spectra from the holograms collected in the Northeastern United States CS, using HOLO Batch. Figure 2-6 shows particle size distributions obtained under different flow conditions of a consecutive measurement, at a depth of 190 m in the Hudson Canyon (39.46 N 72.30 W) on May 1st, 2022. We plot particle volume concentration on the vertical axis as a function of the equivalent spherical diameter. Most particles ranged from 20 μm to 200 μm at this station. The four measurements with varying flow conditions had similar volume concentrations for particles smaller than 50 μm. We observed lower concentrations of particles larger than 70 μm with increasing turbulence intensities. We tried one measurement with extremely high dissipation rates, shown in the black line, which disrupted almost all large particles. As they could withstand the laminar shear shown in the blue curve, we determined that they were breakable aggregates. In other words, these particles fragmented into smaller ones due to the turbulence created by the iDAS. Additionally, the maximum stable particle size decreased

from approximately 300 μm in the laminar flow to 100 μm with a dissipation rate of 1.633 m^2/s^3. This trend also indicated that larger particles were more fragile against the fluid force created by the iDAS.

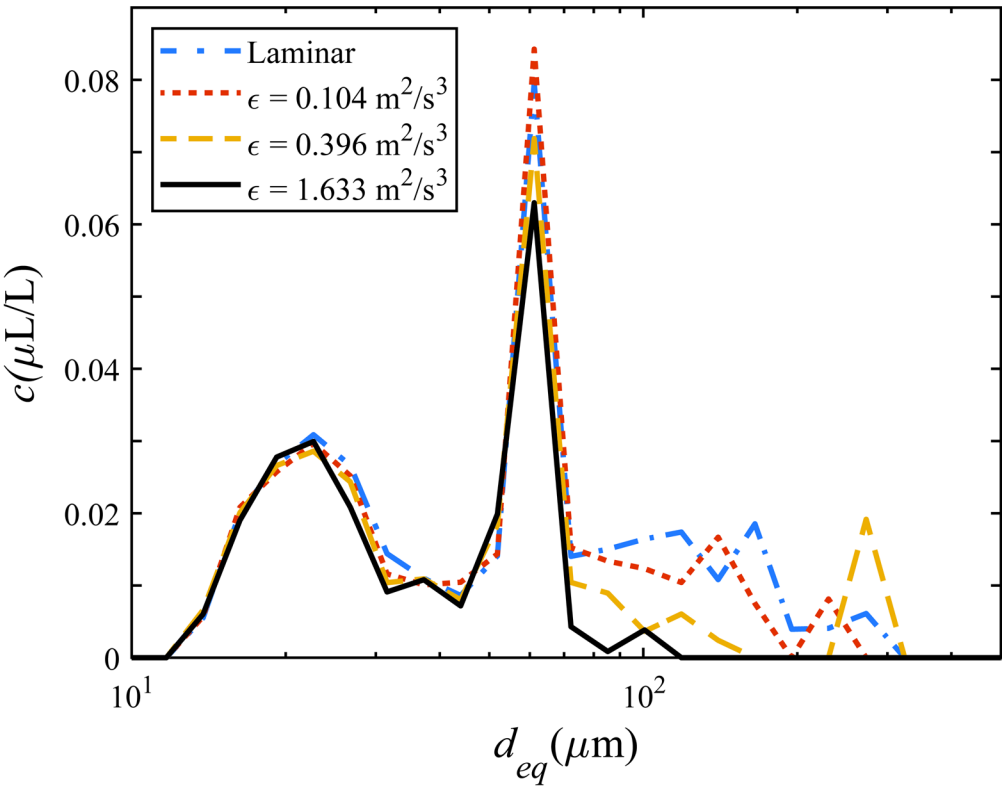

Figure 2-6: particle size spectra of volume fractions as a function of equivalent particle size, measured at the station near the Hudson Canyon (39.46 N 72.30 W) on May 1st, 2022, processed by HOLO Batch (Sequoia Scientific). The four colored lines represent particle size distributions at four thruster speeds.

2.2.3 Disaggregation of Freshwater Aggregates in Lake Tahoe

We had another chance to test the iDAS and determine the prevalence of aggregates and disaggregation in the field at Lake Tahoe, CA, from September 26th to October 2nd, 2022.

This project aimed to understand the sedimentation of wildfire ash and the self-cleansing process in Lake Tahoe. The purpose of this field experiment was to validate the existence of aggregates in Lake Tahoe. Aggregation can enhance the settling rate (Burd & Jackson, 2009) and thus influences the self-cleansing capacity (Santschi, 2018). Lake Tahoe is one of the largest freshwater bodies in California. The increasing urban waste threatens the water quality, local ecosystem, and food web (Antonucci & Schaumburg, 1975; Vander Zanden *et al.*, 2003), from which the phytoplankton growth benefits. Since phytoplankton plays an essential role in forming aggregates in the aquatic environment, this study also helps understand the population level and other environmental changes due to human activities.

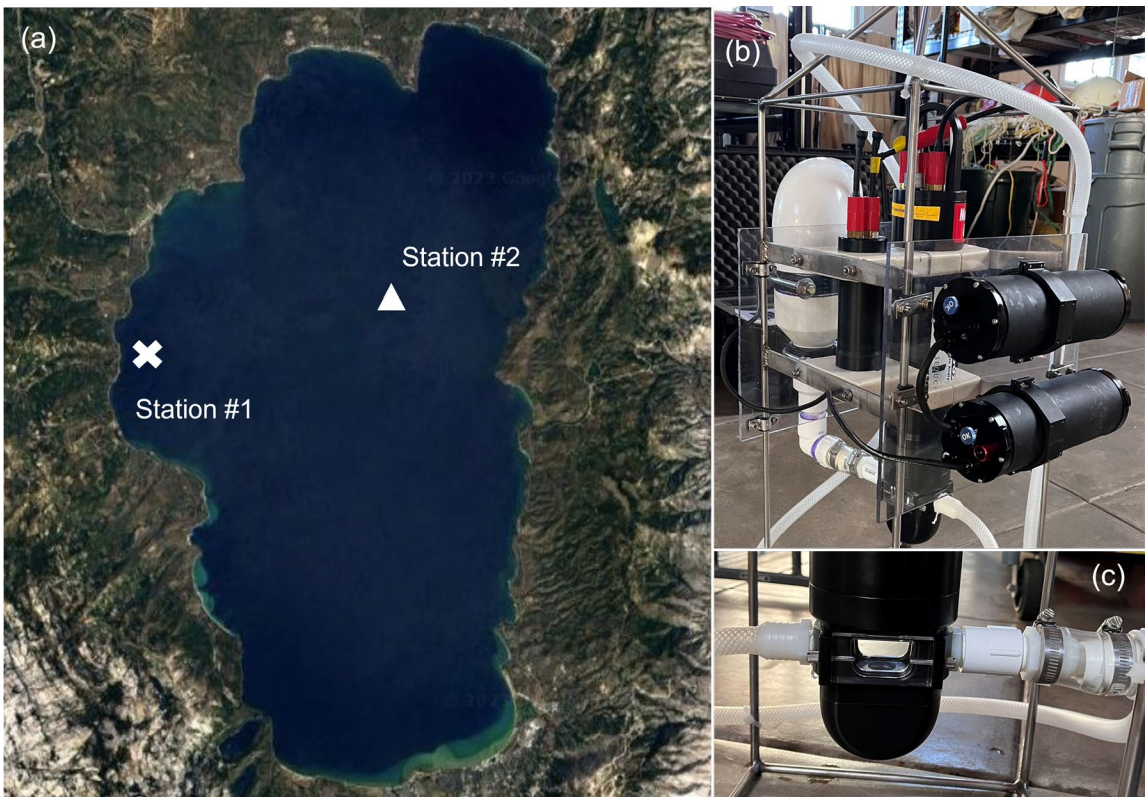

Figure 2-7: (a) satellite map of Lake Tahoe (Google Map) with locations of two test stations, (b) picture of the iDAS attached to a LISST-200X (Sequoia Scientific), and (c) the flow through chamber.

Figure 2-7 shows the locations of the two test stations, one near shore and the other offshore, where we repeated nine iDAS casts at different depths of interest. We detached the new iDAS from a LISST-HOLO2 and attached it to a LISST-200X (Sequoia Scientific) particle sizer, as shown in Figure 2-7(b). A LISST-200X measures suspended particles from 1.0 μm to 500 μm. Like the LISST-100X it succeeds, the LISST-200X uses small-angle forward light scattering and Mie-theory to generate particle concentrations as a function of particle size. We measured particle size distributions at six depths (5 m, 20 m, 40 m, 60 m, 75 m, and 90 m) at station #1 and three depths (5 m, 40 m, and 75 m) at station #2. Each cast performed a full iDAS operation with the eight flow conditions shown in Table 2-1. We have also implemented a separate flow rate calibration for the smaller LISST-200X flow through chamber, displayed in Figure 2-7(c).

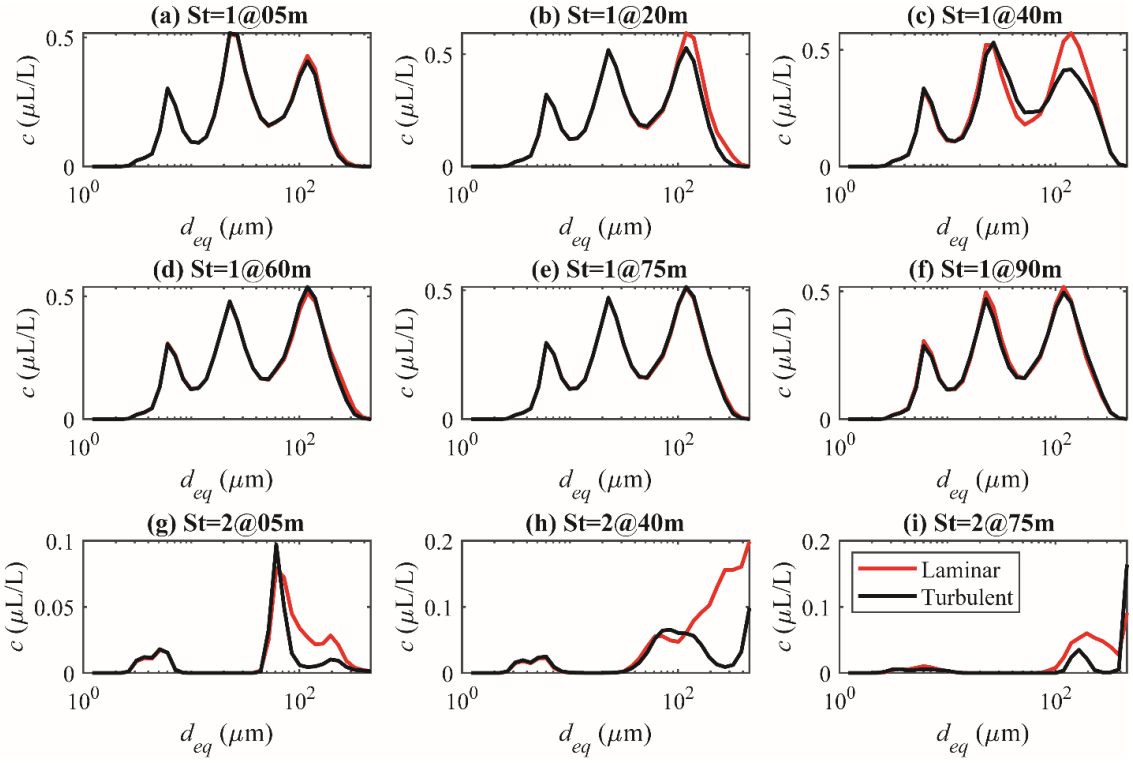

Figure 2-8: particle volume concentrations as a function of equivalent diameter and comparisons of size distributions between laminar and turbulent flows. (a) – (i) show the results at different test stations and depths.

Figure 2-8 compares the particle size statistics between laminar and turbulent flow conditions for nine different casts. The turbulent flow used a PWM signal of 1100, representing the strongest dissipation rate of 1.60 m^2/s^3. The turbulent force was strong enough to break most aggregates. Figure 2-8(a) – (f) plot the volume fractions as a function of particle size at the six depths of station #1, and Figure 2-8(g) – (i) display the results for station #2. At station #1, we observed only small differences between the two flow conditions, which indicated very few aggregates. Most solid particles detected were unbreakable particles, and the three peaks likely represented three major groups of

suspended solid mineral particles. A possible reason for the lack of aggregates might be presence of upwelled particles. Lake Tahoe has prevailing southwesterly winds (Dettinger, 2013), which means that upwelling typically influences the water column near the west shore. We observed the largest difference in particle spectra at depths of 20 m and 40 m. The peak of chlorophyll content occurred right above 40 m depth, so there was likely more phytoplankton within the region, which could have promoted aggregation. The offshore station showed more interesting results, as we observed a distinct decrease in the concentration of large particles with increasing turbulent dissipation rates. Three casts at different depths all revealed the fragmentation of large particles, indicating more organic materials might be present with aggregates in the middle of the lake.

2.3 Summary

This chapter describes the development of the new in-situ disaggregation system. The iDAS allows naturally occurring particles to be exposed to varying flow conditions. The IDAS has great potential to study the formation and strength of aggregates. The new iDAS can easily be attached to different deployable particle-sizing instruments (*e.g.*, LISST-100X, LISST-200X, and LISST-HOLO2) to obtain the particle statistics or images of interest. The autonomous control with a battery power supply enables measurements at depths up to 200 m. Two implementations of the new iDAS have proved its use in disaggregation studies.

A potential drawback to the iDAS is that the uncertainty from the natural environment can cause the nonuniformity of particle statistics. The long time duration necessary for the

iDAS measurements means that it is vulnerable to changes in ambient particle population caused by advecting waters. It is noted that deployment with other sensors will minimize this uncertainty. Another potential problem is that the dissipation rate generated by the thruster might be too strong for the ambient flow conditions.

The measurements performed in the Northeastern United States CS provided evidence of disaggregation in a controlled turbulent environment from the upper ocean to a depth of over 200 m. The disaggregation experiments indicated that hydrodynamic forces in the mixed layer could fragment large marine snow aggregates. The other measurement in Lake Tahoe shows there were more aggregates in the central part of the lake that could be disaggregated, which suggested the presence of additional organic material. The near shore station had more unbreakable particles likely due to upwelling sediment, but the station in the middle of the lake had more organic content. The deployment in Lake Tahoe also revealed that the aggregation process in the freshwater system is as important as that in the ocean.

In-situ measurements are challenging to interpret, as we need additional chemical and biological analysis to figure out the content of marine snow aggregates. The imaging is also limited by the rough environment. The varying ambient hydrodynamic conditions cause more uncertainty in determining the breakup strength. Therefore, a more detailed study of how individual aggregates are breaking apart is needed. Particularly, it is necessary to create a controlled laboratory environment and use known aggregate contents to further clarify the governing factors behind marine snow disaggregation.

Chapter 3

Extension to Stokes' Second Problem and Design of Shear-Generating Disaggregation Tanks

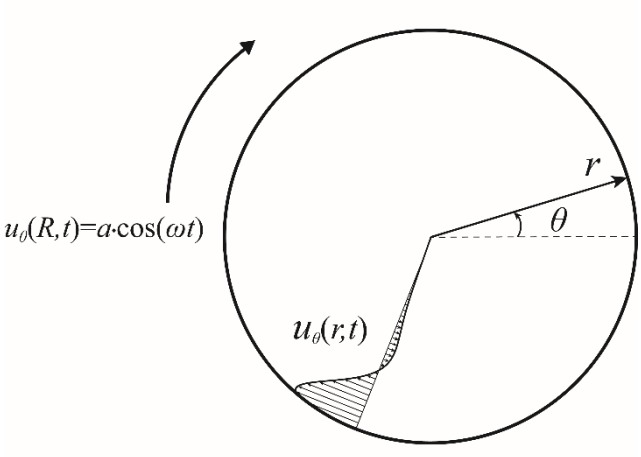

Figure 3-1: Schematic diagram of viscous flows inside an oscillating cylinder.

This chapter describes the oscillatory shear flow inside a cylindrical tank whose wall undergoes a harmonic oscillation. This flow configuration is applied to design an experimental facility with calibrated hydrodynamic conditions for the study of aggregate fragmentation. The concept is inspired by the famous Stokes' second problem, and the work is published by Song and Rau (2020a). The second half of this chapter describes the operation of a novel rotating/oscillating cylindrical tank using proper boundary conditions to create comparable fluid shear in the ocean. We have published the original idea with assessment of particle trajectories (Song & Rau, 2019), and the preliminary experimental validation using bentonite clay flocs (Song & Rau, 2020b).

The chapter is organized into five subsequent sections. In Section 3.1, we formulate the analytical solution of the fluid velocity profile in cylindrical coordinates. In Section 3.2, we describe the implementation of a particle image velocimetry (PIV) experiment with an optically transparent oscillating cylindrical tank, and present the results of our validation study for the quasi-steady state. Additionally, we discuss the unique effect of the dimensionless parameters on the flow. Section 3.3 describes the design of the rotating/oscillating tank by applying the oscillatory viscous flow and evaluates particle trajectories within the tank and stable regions under varying boundary conditions. In Section 3.4, we perform preliminary breakup experiments with bentonite clay. Observed breakup events with aggregation validate the design for the disaggregation study. Section 3.5 provides a summary and recommends future work.

3.1 Viscous Fluid Flow inside an Oscillating Tank

In this problem, we assume an incompressible Newtonian fluid with a constant kinematic viscosity ν and density ρ inside an infinitely long cylinder of radius R. We neglect pressure and gravity forces and assume that the cylinder oscillates around its center at low-enough speeds for the fluid to remain laminar. Figure 3-1 displays a schematic diagram of this flow, where all fluid motion is in the azimuthal direction and we assume that the radial and axial components of velocity can be neglected. We can, thus, reduce the Navier-Stokes equation in cylindrical coordinates to

$$\frac{\partial u_\theta}{\partial t} = \nu\left(\frac{1}{r}\frac{\partial u_\theta}{\partial r} + \frac{\partial^2 u_\theta}{\partial r^2} - \frac{u_\theta}{r^2}\right), \tag{3.1}$$

where u_θ is the azimuthal velocity, t is time, and r is the radial position. Due to the geometry, the azimuthal velocity magnitude at the center of the cylinder must be zero. We can thus solve Equation (3.1) subject to the boundary conditions that include this bounded center and the velocity boundary condition at the wall. For our harmonically oscillating cylinder, we represented the boundary and initial conditions as

$$u_\theta = a \cdot \cos(\omega t) \text{ at } r = R,\ t \geq 0, \tag{3.2a}$$

$$u_\theta = 0 \text{ at } t = 0, \tag{3.2b}$$

$$u_\theta = 0 \text{ at } t < 0. \tag{3.2c}$$

Here, a and ω are the amplitude and frequency of oscillation. The cylinder begins to oscillate about its axis at time t = 0. We use a cosine function to represent the harmonic oscillation. Though they differ in their startup transient, either a sine or cosine function leads to the same quasi-steady behavior. We describe the solution procedure in more detail below, with the solution for a sine function as the boundary condition provided in 0.

3.1.1 Mathematical Formulation

We can non-dimensionalize Equation (3.1) by defining a dimensionless velocity f, time τ and length η as follows,

$$f = \frac{u_\theta}{a}, \tag{3.3a}$$

$$\tau = \omega t, \tag{3.3b}$$

$$\eta = \frac{r}{\delta}, \tag{3.3c}$$

where f is the ratio of the azimuthal velocity to the maximum velocity at the wall and η is the radial position with respect to the characteristic length scale δ. For oscillating flows, the oscillation frequency ω and the viscosity of the fluid v usually determine the characteristic thickness of the oscillatory boundary layer. Therefore we choose δ as,

$$\delta = \sqrt{\frac{\nu}{\omega}}, \tag{3.4}$$

which has the same definition as that used by previous solutions (Erdogan, 2000; Li & Marfatia, 1971). Next, we can non-dimensionally represent the one-dimensional oscillatory flow inside a cylinder as,

$$\frac{\partial f}{\partial \tau} = \frac{\partial^2 f}{\partial \eta^2} + \frac{1}{\eta}\frac{\partial f}{\partial \eta} - \frac{f}{\eta^2}, \tag{3.5}$$

$$f = \cos(\tau) \text{ at } \eta = \eta_R, \ \tau \geq 0, \tag{3.6a}$$

$$f = 0 \text{ at } \eta = 0, \tag{3.6b}$$

$$f = 0 \text{ at } \tau < 0, \tag{3.6c}$$

where $\eta_R = R/\delta$ is a constant representing the dimensionless outer radius of the tank. From here, we apply the Laplace transform to solve the initial value problem (O'Neil, 2011), $L[f(\eta,\tau)] = F(\eta,s)$. We can then write the governing equation after the Laplace transformation with a zero initial condition as

$$\eta^2 \frac{\partial^2 F}{\partial \eta^2} + \eta \frac{\partial F}{\partial \eta} - (s\eta^2 + 1)F = 0, \tag{3.7}$$

with the two boundary conditions now defined as

$$F\left(\eta_R, s\right) = \frac{s}{s^2 + 1}, \tag{3.8a}$$

$$F\left(0, s\right) = 0. \tag{3.8b}$$

Equation (3.7) is the modified Bessel differential equation (Howlett *et al.*, 1966) and its general solution is given as

$$F(\eta, s) = C_1 I_1\left(\eta\sqrt{s}\right) + C_2 K_1\left(\eta\sqrt{s}\right), \tag{3.9}$$

where I_1 is the modified Bessel function of the first kind and of order one and K_1 is the modified Bessel function of the second kind and of order one. By applying the boundary conditions of Equations (3.8a) and (3.8b), we can solve for the two constants C_1 and C_2 as

$$C_1 = \frac{s}{s^2 + 1} \cdot \frac{1}{I_1\left(\eta_R\sqrt{s}\right)}, \tag{3.10a}$$

$$C_2 = 0. \tag{3.10b}$$

Therefore, the general solution of Equation (3.9) becomes

$$F\left(\eta, \tau\right) = \frac{s}{s^2 + 1} \cdot \frac{I_1\left(\eta\sqrt{s}\right)}{I_1\left(\eta_R\sqrt{s}\right)}, \tag{3.11}$$

Here we can obtain a solution through the use of the inverse Laplace transform, which defines the dimensionless velocity f as

$$f\left(\eta, \tau\right) = \frac{1}{2\pi i}\int_{c-i\infty}^{c+i\infty} \frac{s}{s^2 + 1} \cdot \frac{I_1(\eta\sqrt{s})}{I_1\left(\eta_R\sqrt{s}\right)} \cdot \exp\left[s\tau\right] ds. \tag{3.12}$$

We can then solve Equation (3.12) to find the dimensionless solution for the azimuthal velocity inside of our cylinder. Equation (3.12) is similar in form to solutions provided for Stokes' second problem on the outside of a cylinder (Li & Marfatia, 1971), but differs in that their solution used K_1 instead. The Bessel function K_1 converges to 0 as z increases, which is appropriate for the far-field boundary condition of an external flow around a cylinder in an infinite stagnant fluid. To solve the inverse Laplace transform in Equation (3.12), we can make use of the Residue Theorem. We start by defining a function $g(s)$ as the integrand of Equation (3.12),

$$g(s) = \frac{s}{s^2+1} \cdot \frac{I_1(\eta\sqrt{s})}{I_1\left(\eta_R\sqrt{s}\right)} \cdot \exp[s\tau], \tag{3.13}$$

where s can be any complex number. The terms in the denominator of Equation (3.13) indicate $g(s)$ has simple poles at $\pm i$ and at all values where $I_1\left(\eta_R\sqrt{s}\right) = 0$, where z_0 is a simple pole of the complex-value function g, expressed as,

$$\mathrm{Res}[g, z_0] = \lim_{s \to z_0} (s - z_0)\, g(s). \tag{3.14}$$

For the simple poles at $z_0 = \pm i$, the two residues are

$$\mathrm{Res}[g, i] = \frac{1}{2}\exp[i\tau]\frac{I_1\left(\eta\sqrt{i}\right)}{I_1\left(\eta_R\sqrt{i}\right)}, \tag{3.15a}$$

$$\mathrm{Res}[g, -i] = \frac{1}{2}\exp[-i\tau]\frac{I_1\left(\eta\sqrt{-i}\right)}{I_1\left(\eta_R\sqrt{-i}\right)}. \tag{3.15b}$$

To define the residues for the poles associated with $I_1\left(\eta_R\sqrt{s}\right)=0$, we need to find all zeros for this function in the complex plane. $I_1(z)$ has only one real zero when evaluated at $z = 0$ and we can find the residue for the resulting pole at $z_0 = 0$ through Equation (3.14) and use of L'Hopital's rule (Howlett *et al.*, 1966),

$$\mathrm{Res}\left[g,0\right]=\lim_{s\to 0}\left(s-0\right)\frac{s}{s^2+1}\cdot\frac{I_1(\eta\sqrt{s})}{I_1\left(\eta_R\sqrt{s}\right)}\cdot\exp\left[s\tau\right]=0. \tag{3.16}$$

We can find imaginary zeros of I_1 by substituting $I_1\left(iz\right)=iJ_1\left(z\right)$, where $J_1\left(z\right)$ is the Bessel function of the first kind and of order one. All zeros of the odd function $J_1\left(z\right)$ occur for simple and real values of z (Howlett *et al.*, 1966). If we define $z=\pm\alpha_n$ to be the n^{th} zero of $J_1(z)$, and $s = z_{0,n}$ as the n^{th} zero of $I_1\left(\eta_R\sqrt{s}\right)$, we have $i\eta_R\sqrt{z_{0,n}}=\pm\alpha_n$, which is equivalent to

$$z_{0,n}=-\frac{\alpha_n^2}{\eta_R^2}. \tag{3.17}$$

Equation (3.17) is, thus, and expression for all the simple poles, $z_{0,n}$, of $g(s)$. Next, we can re-write Equation (3.13) into the following form,

$$g\left(s\right)=\frac{p\left(s\right)}{q\left(s\right)}, \tag{3.18}$$

where

$$p\left(s\right)=\exp\left[s\tau\right]\frac{s}{s^2+1}\cdot I_1\left(\eta\sqrt{s}\right), \tag{3.19}$$

$$q\left(s\right)=I_1\left(\eta_R\sqrt{s}\right). \tag{3.20}$$

Corollary 22.1 on page 735 of O'Neil (2011) shows that, if $q(s)$ in Equation (3.18) has a simple zero at z_0 and $p(z_0) \neq 0$, the residue of $g(s)$ at the resulting pole can be written as,

$$\mathrm{Res}\left[g, z_{0,n}\right] = \frac{p\left(z_{0,n}\right)}{q'\left(z_{0,n}\right)} = \exp\left[z_{0,n}\tau\right] \frac{4z_{0,n}^{\frac{3}{2}}}{\left(z_{0,n}^2+1\right)\eta_{R?}} \cdot \frac{I_1\left(\eta\sqrt{z_{0,n}}\right)}{I_0\left(\eta_R\sqrt{z_{0,n}}\right) + I_2\left(\eta_R\sqrt{z_{0,n}}\right)}, \quad (3.21)$$

where q' is the derivative of q with respect to s and $I_0(z)$ and $I_2(z)$ are modified Bessel functions of the first kind and of order zero and two, respectively. Taking the sum of Equation (3.15a), (3.15b), (3.16) and (3.21), we can arrive at the expression of the solution to Equation (3.12) as

$$\begin{aligned} f(\eta,\tau) = \sum \mathrm{Res}\left[g, z\right] &= \frac{1}{2}\left[\exp\left[i\tau\right]\frac{I_1\left(\eta\sqrt{i}\right)}{I_1\left(\eta_R\sqrt{i}\right)} + \exp\left[-i\tau\right]\frac{I_1\left(\eta\sqrt{-i}\right)}{I_1\left(\eta_R\sqrt{-i}\right)}\right] \\ &+ \sum_n^{\infty} \exp\left[z_{0,n}\tau\right] \frac{4z_{0,n}^{\frac{3}{2}}}{\left(z_{0,n}^2+1\right)\eta_{R?}} \cdot \frac{I_1\left(\eta\sqrt{z_{0,n}}\right)}{I_0\left(\eta_R\sqrt{z_{0,n}}\right) + I_2\left(\eta_R\sqrt{z_{0,n}}\right)}. \end{aligned} \quad (3.22)$$

Equation (3.22) is, thus, the analytical solution for the dimensionless velocity f for one-dimensional laminar fluid flow inside of a harmonically oscillating cylindrical wall. Equation (3.22) consists of two parts. The first part is the solution for the quasi-steady dimensionless velocity, f_s, which has a period of 2π and can be written as,

$$f_s(\eta,\tau) = \frac{1}{2}\left[\exp\left[i\tau\right]\frac{I_1\left(\eta\sqrt{i}\right)}{I_1\left(\eta_R\sqrt{i}\right)} + \exp\left[-i\tau\right]\frac{I_1\left(\eta\sqrt{-i}\right)}{I_1\left(\eta_R\sqrt{-i}\right)}\right], \quad (3.23)$$

The infinite summation in Equation (3.22), therefore, is necessary to describe the transient starting condition of the fluid motion. This second part of the solution decays rapidly with the time τ due to the exponential function of the negative $z_{0,n}$.

3.1.2 Analytical Results

Figure 3-2(a) shows the analytical quasi-steady velocity profiles calculated with Equation (3.23) for an infinitely long cylinder with a dimensionless radius of $\eta_R = 50$. In this figure, $\tau = 0$ corresponds to the beginning of the cosine boundary condition. Here, we plot the instantaneous velocity at six different phase angles during one period of oscillation. As expected, the amplitude of dimensionless velocity is high near the wall and becomes smaller as η decreases. Though not shown in the plot, the velocity becomes zero at $\eta = 0$. We determine a positive velocity envelope from the norm of the quasi-steady velocity in Equation (3.22). With a symmetric negative envelope, they represent the greatest magnitude of velocity over time as a function of η. The distance between envelopes can be used to determine δ_s, which is the penetration depth of the viscous wave and is defined as the point at which the value of the envelope magnitude reaches 0.01 (Schlichting, 1979). The case shown in Figure 3-2 ($\eta_R = 50$) has a penetration depth $\delta_s = 6.6\delta$. This value is slightly greater than that of the penetration depth of Stokes' second problem for a flat plate, given as 6.5δ (Schlichting, 1979). The thicker layer in the present problem can be attributed to the cylindrical geometry, as we will discuss in greater detail below. Figure 3-2(b) shows the velocity boundary condition at $\eta = \eta_R$, given by Equation (3.2a), plotted as a function of dimensionless time. In this figure we also plot the time-varying velocity at three locations close to the boundary; $\eta = 47$, 48, and 49. The velocity of the fluid inside the tank follows the motion of the boundary oscillation but with reduced amplitude and a lag in

phase. At a dimensionless radius of $\eta = 47$, the maximum velocity is 12.4% of that at the boundary.

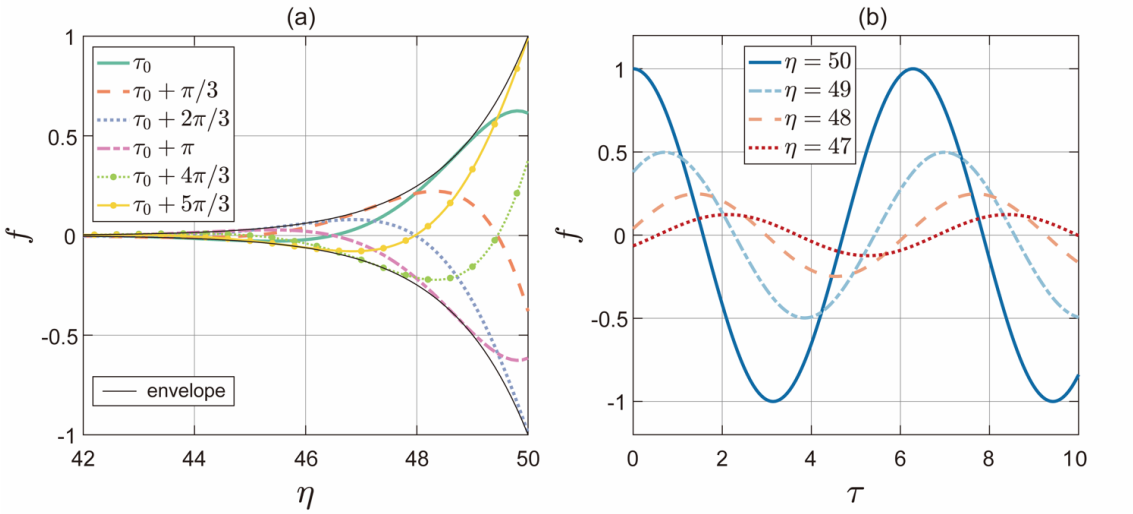

Figure 3-2: (a) One period of quasi-steady velocity profiles plotted versus dimensionless radius during one oscillation of the cylinder (cylinder radius is $\eta_R = 50$), and (b) dimensionless velocity versus dimensionless time at the cylinder boundary and three radial distances within the fluid.

Figure 3-3 shows the fluid velocity profiles considering the transient start, Equation (3.22), at early dimensionless times for the same boundary condition and cylinder with $\eta_R = 50$. We plot in total four velocity profiles within a quarter of the first oscillation period, along with one instant of the quasi-steady velocity profile. The first 500 terms of the infinite series are used in Figure 3-3 and the truncation error is estimated to be $O(10^{-15})$. Figure 3-3 shows how the transient motion from the initial startup impulse vanishes as time increases and the velocity profiles approach their quasi-steady values. After one quarter oscillation

($\tau = \pi/2$), the maximum difference in dimensionless velocity compared to the quasi-steady velocity at the corresponding phase angle reduces to less than 0.06. After the first full cycle of oscillation, the difference reduces to less than 0.01.

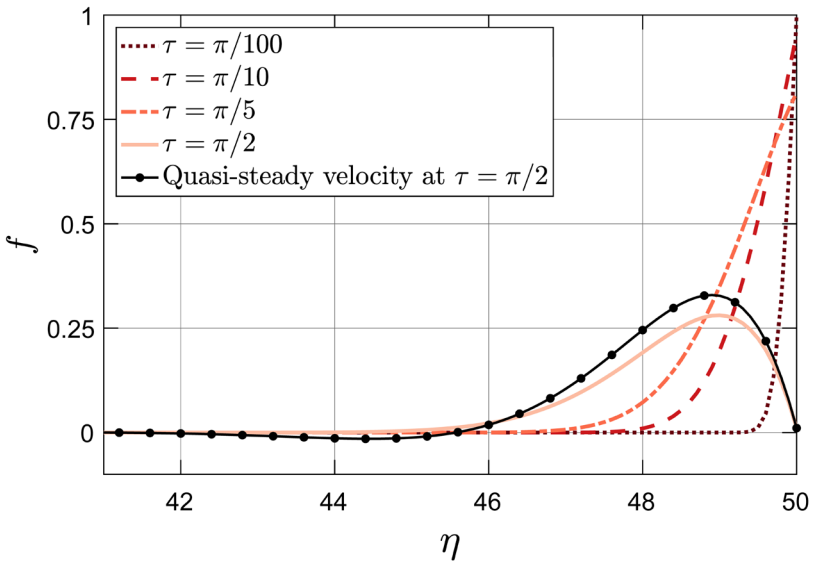

Figure 3-3: Transient velocity profiles, Equation (3.22), at different dimensionless times plotted versus dimensionless radius. The solid line with circles represents the quasi-steady velocity profile, Equation (3.23) at a phase angle of π/2. The first 500 positive zeros of $J_1(z)$ are used for Equation (3.22).

3.2 Flow Validation Using Particle Image Velocimetry

3.2.1 Experimental Methods

3.2.1.1 Experimental Facility

To verify the validity of quasi-steady motion expressed in Equation (3.23), we performed PIV experiments of this internal cylindrical oscillating flow. Song and Rau (2019) originally developed the experimental facility, which consisted of a transparent cylindrical acrylic tank that rested on four rollers, as shown schematically in Figure 3-4(a). A programmable electric servo motor (Dynamixel MX-28T, Trossen Robotics) connected to one end of the tank with a belt-pulley system controlled the rotational motion of this tank. The tank was 300 mm in length, 100 mm in inner diameter with a wall thickness of 5 mm. We determined the tank was long enough that we could neglect the effect of secondary flows on measurements acquired along the central cross-section of the tank by estimating the end-wall boundary layer thickness (Kármán, 1921; Turner & Weidman, 2019). We precisely controlled the servo motor using a U2D2 controller (Trossen Robotics).

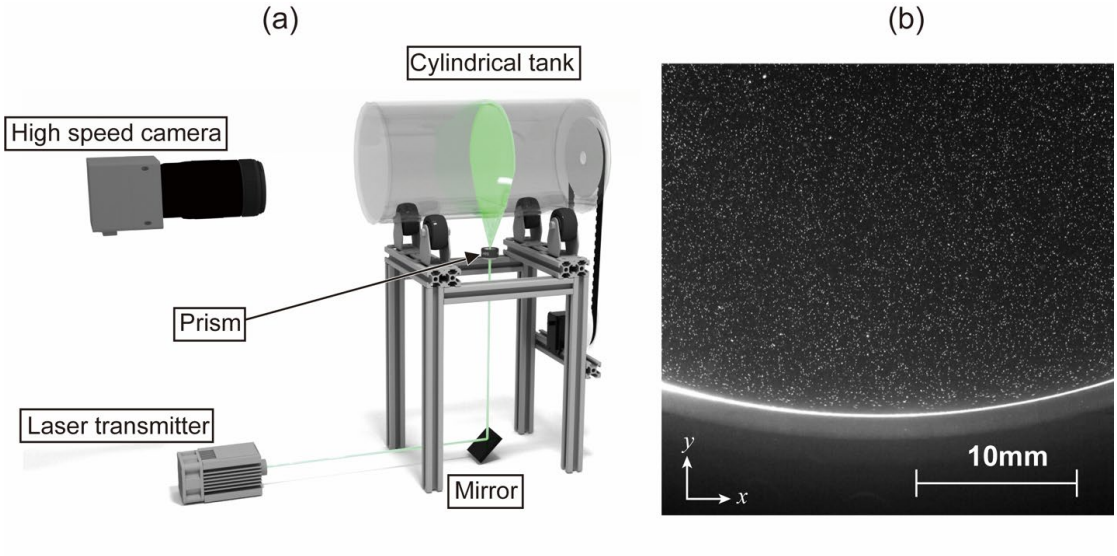

Figure 3-4: (a) Schematic diagram of the test section showing the laser path, and (b) the camera field-of-view from the high-speed camera showing illumination of PIV particles.

We illuminated the PIV flow tracers using a continuous laser with a wavelength of 532 nm (Opus 532, Laser Quantum), which was formed into a light sheet that bisected the tank using a Powell lens (75º, Edmund Optics). The light sheet was parallel to the end caps of the tank so that the azimuthal fluid velocity could be captured by the illuminated flow tracers. An example PIV image obtained with this illumination scheme is shown in Figure 3-4(b).

We mounted a high-speed camera (FASTCAM Mini AX200, Photron) such that its viewing axis was perpendicular to the illuminated PIV particles, which it viewed through the transparent end cap of the cylindrical tank. We used a macro lens with a 200 mm focal length (AF Micro-Nikkor 200mm f/4D IF-ED) to focus the camera on the light sheet. This lens provided a field of view (FOV) roughly 28 mm × 28 mm (27 μm per pixel resolution

with the 1024 × 1024 pixel sensor of the camera). Because this FOV was not big enough to view the entire tank cross section, we positioned the camera such that the fluid near the bottom tank wall was in view, as shown in Figure 3-4(b). To reduce the effects of wall reflections to enable near-wall measurements, we seeded the water with red fluorescent polystyrene PIV particles (PSFR010UM, MagSphere) and installed a wavelength filter (Orange M62.0 × 0.75 filter, ThorLabs) on the end of the camera lens. We calculated the seeding density from our experimental images to be on average around 15 particles per 32 × 32 pixel window.

We recorded PIV image frames as a time series at a rate of 500 frames per second (fps) with a shutter speed of 1/1000 s. The period for one oscillation of this quasi-steady problem depends on the oscillation frequency ω, as given in Equation (3.2a). We recorded data for each test for at least one period of oscillation after a long enough time had passed to avoid the startup transient.

3.2.1.2 Data Processing

We calculated velocity vectors from our PIV images using codes developed by Eckstein and Vlachos (2009a,b,c) and available online (Vlachos, 2015). Before PIV analysis, we calculated the local minimum intensity at each pixel from the entire image dataset and subtracted this intensity from each image. This process removes all background intensity that remains stationary throughout the experiment. We implemented three passes for the velocity evaluation. The first pass used a square evaluation window with a size of 32 × 32 ($x \times y$) pixels and a window overlap of 50% in both x and y directions. After the initial pass,

we reduced the window size to 32 × 8 pixels with a window overlap of 75%. We reduced the window height to eight pixels to better resolve the velocity profile in the boundary layer (Wieneke & Pfeiffer, 2010), which was predominantly in the *y*-direction given the placement of our FOV within this cylindrical geometry. Overall, this evaluation scheme gave us vector spacing of 5 vectors per mm in the *x*-direction and 18 vectors per mm in the *y*-direction. We applied a universal outlier detection (UOD) (Westerweel & Scarano, 2005) after each pass to eliminate bad vectors and a Gaussian smoothing filter after the first and second passes. We used the robust phase correlation (A. C. Eckstein, Charonko, & Vlachos, 2008; A. Eckstein & Vlachos, 2009a,b,c) with iterative image deformation to compensate for in-plane velocity gradients (Scarano, 2002).

The camera viewed a portion of the tank wall during the experiments, which was outlined by a small amount of PIV particles that had adhered to the wall during the initial test setup. This outline can be seen in Figure 3-4(b), where the internal wall boundary appears as a uniform bright curve. Because the camera FOV did not include the center of the tank, we calculated the location of the tank center by fitting a circle to this illuminated wall arc. This fitting process is shown schematically in Figure 3-5. The radial locations of the fluid within the FOV could then be determined from their locations relative to the wall boundary and the tank center.

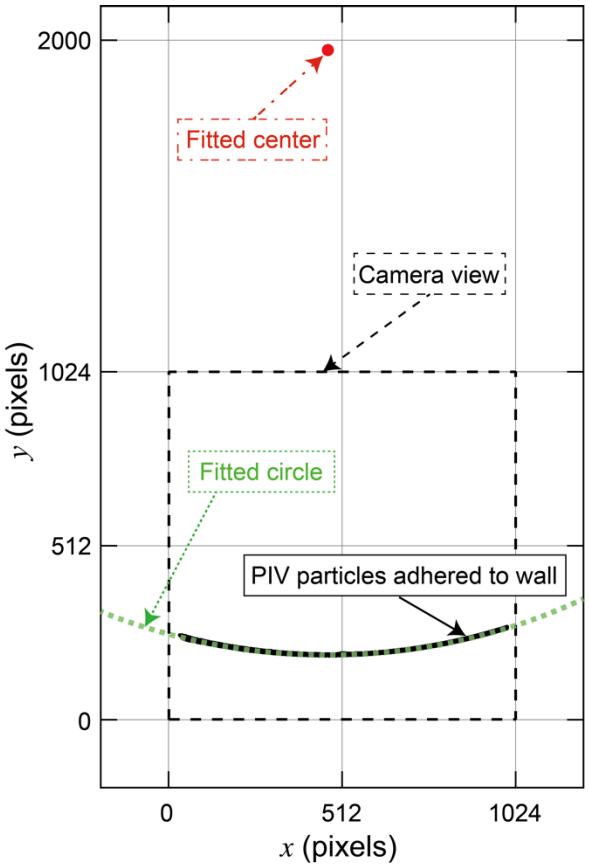

Figure 3-5: The center of the cylindrical tank as determined from fitting a circle to the tank wall within the camera FOV.

To obtain azimuthal velocity profiles, we first linearly interpolated the measured velocity vectors (in Cartesian coordinates from our PIV analysis) to a circular grid with a radial spacing of 5.9 vectors per mm. We could then calculate the spatially averaged azimuthal velocity at each radial location from the interpolated vectors at each experimental time step. This azimuthal averaging reduced our measurement uncertainty, discussed below, and is consistent with the one-dimensionality of our flow geometry.

3.2.2 Experimental Validation

We implemented a series of particle image velocimetry (PIV) measurements using the experimental facility described in Chapter 3.2.1 to validate the analytical solution of quasi-steady motion given by Equation (3.23). The oscillation frequency of the cylindrical tank was 0.5 rad/s and oscillation magnitude was 9 cm/s, giving us the boundary condition of

$$u_\theta(R,t) = 9 \cdot \cos(0.5t). \tag{3.24}$$

The kinematic viscosity v of the water was $9.8 \cdot 10^{-7}$ m^2/s and the radius of the cylinder was R = 5 cm, which resulted in a dimensionless radius of $\eta_R = 35.7$ for this test case. Figure 3-6(a) shows dimensional velocity profiles plotted versus radius at two distinct times during the oscillation, where t = 0 s was the starting time of the experimental recording. The experimental results closely follow the analytical solution and display the boundary layer clearly near the tank wall. Figure 3-6(b) shows the velocity variation over time at a fixed radial distance of r = 4.77 cm from the center of the tank, which also closely followed the analytical solution given by Equation (3.23).

We analyzed the difference between the analytical and experimental results and the time-average root-mean-square deviation was 0.09 cm/s, with a maximum of 0.22 cm/s at r = 4.97 cm. Uncertainty in the fluid viscosity, which was calculated for water at room temperature, and the synchronization between the analytical and experimental results could account for this deviation. Based on the resolution and the frame rate of our measurements, we estimate that the results could be out-of-sync by a maximum of 0.02 s, which would result in a velocity discrepancy of up to 1.9%. It should be noted that we observed no flow

instabilities in the experimental results at these conditions and that the flow was stable and repeatable over many oscillations.

We analyzed the uncertainty in our PIV measurements following the method developed by (Xue *et al.*, 2014), which utilizes the mutual information between particle image patterns to estimate uncertainty. Effectively, this method estimates uncertainty based on the strength of the PIV correlation. We present velocity uncertainty as the vertical error bars shown in both Figure 3-6(a) and (b). Uncertainty in our measurements was highest in locations very near the wall ($r > 4.92$ cm) since there were fewer PIV particles in this region and, thus, poorer PIV correlation. The maximum root-sum-square uncertainty of velocity in this near-wall region was 7.8%, compared to the oscillation magnitude at the wall. The locations further from the wall had uncertainty in velocity of 2% or less. In addition to the velocity determination, there were also uncertainties in our calculation of radial distance from the center of the tank. During our analysis, we observed that the inner wall of the tank moved vertically within the camera FOV by a maximum of 25 pixels (0.7 mm) over each rotation, which we determined was caused by a non-constant tank wall thickness. The fitting process used to find the tank center (described in Chapter 3.2.1) accounted for this displacement, but did not eliminate the position uncertainty. We estimated the uncertainty in the radial position to be 0.12 mm based on the fitted results. Given the excellent agreement between our analytical solution and experimental results, the tank imperfection did not appear to significantly affect the quasi-steady azimuthal fluid velocities in the tank.

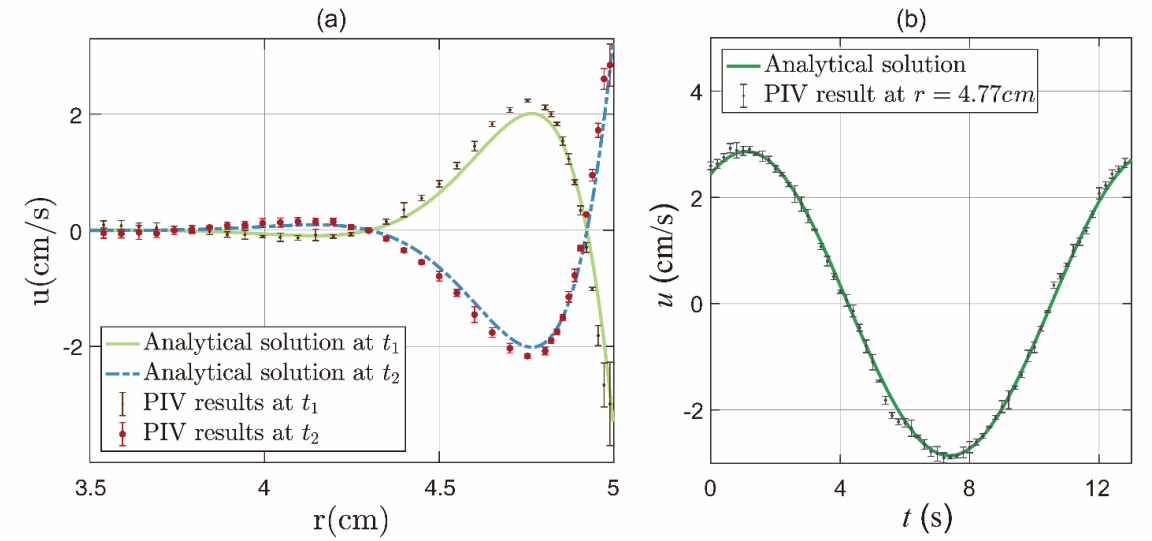

Figure 3-6: PIV validation of our analytical solution for a tank with dimensionless radius of $\eta_R = 35.7$ (R = 5 cm, ω = 0.5 rad/s) showing, (a) comparisons between the analytical solution and PIV results at two time instants and, (b) velocity variation over one period at a radial distance r = 4.77 cm.

3.2.3 Discussion of Dimensionless Variables

This problem can be thought of as an extension to the classic Stokes' second problem, where there now exists a balance between the penetration depth of the viscous effects and the finite radius of the cylinder. From the analytical solution of quasi-steady dimensionless velocity, the velocity profile given by Equation (3.23) is only affected by the size of the cylinder R, the oscillation frequency ω, and the viscosity of the fluid ν, all of which are captured in the nondimensional radial position η. Based on this non-dimensional relationship, we can expect that decreasing the size of cylinder will have a similar effect on the dimensionless velocity profile as decreasing the oscillation frequency or using a

more viscous fluid. At the same time, the amplitude of the oscillation a, which only determines the magnitude of the azimuthal velocities, will not influence the penetration depth per radius as long as the flow remains laminar. In Figure 3-7, we plot velocity profiles for four different η_R, which show how the fluid velocity profile penetrates further into the cylinder as η_R decreases. This plot indicates that thick Stokes layers, relative to the cylinder radius, can be generated by using small cylinders, low-frequency oscillations, or more-viscous fluids.

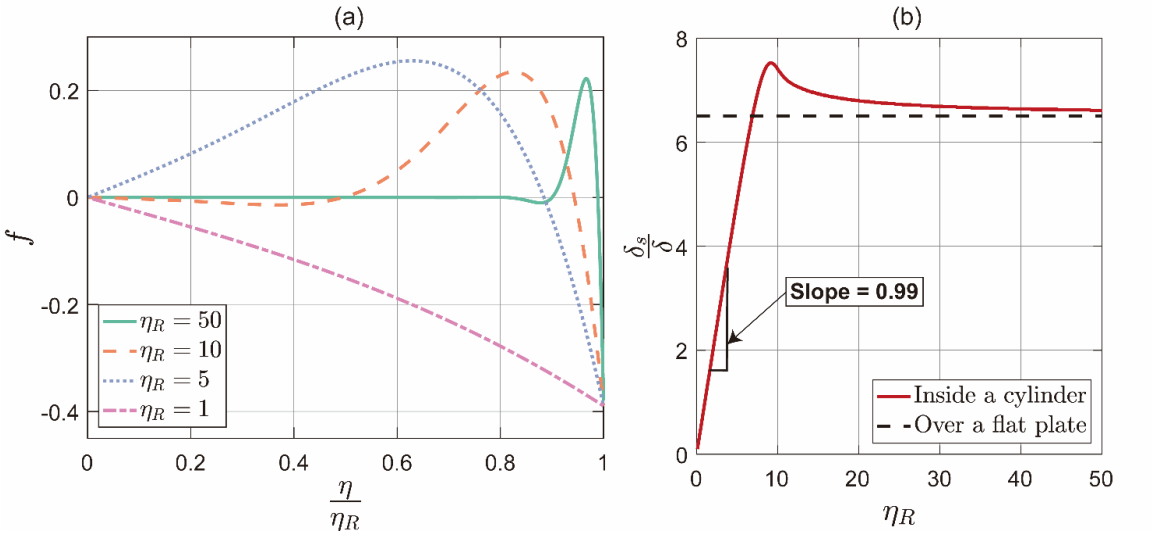

Figure 3-7: (a) Dimensionless velocity profiles at $\tau = 0.63\pi$ for four different dimensionless cylinder sizes η_R, and (b) penetration depth ratio δ_s/δ versus η_R compared to the case of the flat plate.

Unlike Stokes' second problem of external flows on an infinite flat plate (Rayleigh, 1911; Herman Schlichting, 1979; Stokes, 1850) or outside a cylinder (Li & Marfatia, 1971; Rivero *et al.*, 2019), which have a single boundary, our solution for the flow inside a cylinder is bounded by the cylinder center and the cylinder outer wall. This leads to two

distinct solutions at the limit of very small and large cylinders. When the dimensionless cylinder size η_R approaches infinity, the penetration depth thickness approaches that of Stokes' second problem for a flat plate, as shown in Figure 3-7(b). As we decrease the cylinder radius, the penetration depth initially thickens relative to δ, but then quickly decreases. As the cylinder size approaches δ (η_R = 1), the flow approaches solid body rotation and the slope of δ_s/δ as a function of η_R converges to a value of 0.99, which is equivalent to $\delta_s = 0.99R$. Given that the definition of δ_s is the point at which the velocity envelope decays to 1% of the boundary velocity amplitude, this equality is consistent with solid body rotation. Recalling that the characteristic length scale of this problem is defined as $\delta = \sqrt{\nu/\omega}$, we can define the characteristic velocity as the oscillation magnitude a, and the Reynolds number for the problem as $\mathrm{Re} = a\delta/\nu = a/\sqrt{\nu\omega}$, which has the same expression as that used by previous studies (Kerczek & Davis, 1974; Rivero *et al.*, 2019). We can also define a Strouhal number based on the oscillation frequency of $2\pi\omega$, where $\mathrm{St} = 2\pi\omega R/a$. Multiplying the Reynolds number by the Strouhal number we obtain,

$$\mathrm{Re}\cdot\mathrm{St} = \frac{a}{\sqrt{\nu\omega}}\cdot\frac{2\pi\omega R}{a} = 2\pi\frac{R}{\sqrt{\nu/\omega}} = 2\pi\eta_R \tag{3.25}$$

The product of the two dimensionless number is, thus, 2π times the dimensionless radius η_R. This value indicates the ratio of oscillatory momentum to the viscous effects. Small cylinder sizes are analogous to a small value of Re·St and indicate that viscous forces dominate the flow. Under these conditions, near-linear velocity profiles result from the solution as shown in Figure 3-7(a) for η_R = 1. From this, we can conclude that Stokes flow is maintained for dimensionless cylinder radii $\eta_R \ll 1$.

3.3 Design of a Rotating/Oscillating Tank for Studying Disaggregation

3.3.1 Velocity Profiles of a Rotating/Oscillating Tank

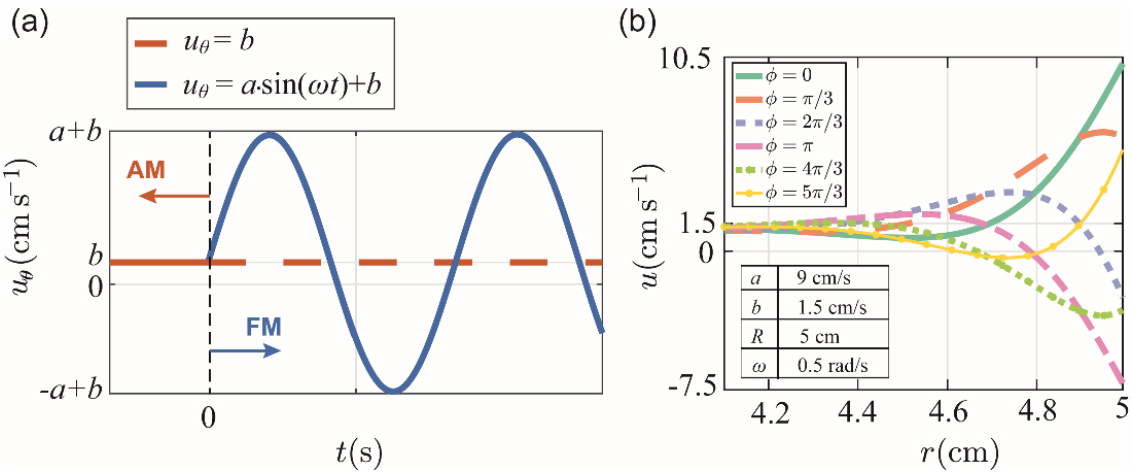

Figure 3-8: (a) Sample wall boundary conditions for both Aggregation Mode and Fragmentation Mode, and (b) one period of quasi-steady velocity profiles plotted at different phase angles during Fragmentation Mode.

We have developed an analytical solution to describe the fluid motion with a symmetric oscillation (Song & Rau, 2020a). Particle image velocimetry (PIV) experiments confirmed the validity of the analytical results and that the flow along the central tank cross-section remained two-dimensional and laminar. Here, we modified this analytical solution to include the oscillating motion plus the constant rotation of the roller tank. Assuming the saltwater is an incompressible Newtonian fluid with a constant kinematic viscosity ν, we can simplify the two-dimensional Navier Stokes equation to contain only the azimuthal component, as shown in Equation (3.1),

$$\frac{\partial u_\theta}{\partial t} = \nu\left(\frac{1}{r}\frac{\partial u_\theta}{\partial r} + \frac{\partial^2 u_\theta}{\partial r^2} - \frac{u_\theta}{r^2}\right). \tag{3.1}$$

In Equation (3.1), gravity is neglected as it integrates to zero in the azimuthal direction assuming no free surfaces are present inside of the closed cylinder. During the switch from Aggregation Mode (AM) to Fragmentation Mode (FM), the fluid experiences a change in the outer wall boundary condition. Shown in Figure 3-8(a) as a constant rotation speed $u_\theta = b$ in AM, this boundary condition changes to $u_\theta = a\sin(\omega t) + b$ in FM, where a is the amplitude and ω the angular frequency of the superimposed harmonic oscillation. In our analysis, we assumed the tank rotated in AM for a long enough time that the fluid velocity was a steady solid-body rotation. The resulting initial and boundary conditions representing a sudden change from AM to FM are thus,

$$u_\theta(r,0) = \frac{r}{R}b, \tag{3.26a}$$

$$u_\theta(R,t) = a\cdot\sin(\omega t) + b, \tag{3.26b}$$

$$u_\theta(0,t) = 0. \tag{3.26c}$$

where R is the inside radius of the tank. The resulting transient solution, which contains the transition motion from solid body rotation, is written as,

$$u_\theta(r,t) = \frac{r}{R}b + \frac{a}{2}\left[\exp\left(i\omega t - i\frac{\pi}{2}\right)\frac{I_1\left(r\sqrt{i\,\omega/\nu}\right)}{I_1\left(R\sqrt{i\,\omega/\nu}\right)} + \exp\left(-i\omega t + i\frac{\pi}{2}\right)\frac{I_1\left(r\sqrt{-i\,\omega/\nu}\right)}{I_1\left(R\sqrt{-i\,\omega/\nu}\right)}\right]$$
$$+a\cdot\sum_n^\infty \exp\left(z_{0,n}\omega t\right)\frac{4z_{0,n}^{1/2}}{\left(z_{0,n}^2+1\right)R\sqrt{\omega/\nu}}\cdot\frac{I_1\left(r\sqrt{z_{0,n}\,\omega/\nu}\right)}{I_0\left(R\sqrt{z_{0,n}\,\omega/\nu}\right)+I_2\left(R\sqrt{z_{0,n}\,\omega/\nu}\right)},$$

(3.27)

where I_0, I_1, and I_2 are the modified Bessel functions of the first kind and order zero, one, and two, respectively. The variable $z_{0,n}$ is defined as,

$$z_{0,n} = -\frac{\alpha_n^2 \nu^2}{R^2 \omega^2}, \tag{3.28}$$

where α_n is the n^{th} zero of J_1, the Bessel function of the first kind and order one. The details of the mathematical solution procedure to derive Equation (3.27) are identical to those provided by Song and Rau (2020a) and have, thus, been omitted here for brevity. Equation (3.27) consists of three terms: the first term represents solid body rotation, the second term represents the oscillating velocity at different radial locations, and the third term represents a rapidly decaying transient motion due to the transition between AM and FM. This third transient term decays within one cycle of oscillation (Song & Rau, 2020a), after which we can neglect the transient term in Equation (3.27) and assume the fluid motion inside the tank obtains a periodic state represented by,

$$u_{\theta,s}(r,t) = \frac{r}{R}b + \frac{a}{2}\left[\exp\left(i\omega t - i\frac{\pi}{2} \right) \frac{I_1\left(r\sqrt{i\,\omega/\nu} \right)}{I_1\left(R\sqrt{i\,\omega/\nu} \right)} + \exp\left(-i\omega t + i\frac{\pi}{2} \right) \frac{I_1\left(r\sqrt{-i\,\omega/\nu} \right)}{I_1\left(R\sqrt{-i\,\omega/\nu} \right)} \right]. \tag{3.29}$$

Figure 3-8(b) shows periodic velocity profiles at six different phase angles within one period of oscillation during FM for an oscillation magnitude of a = 9 cm/s and the constant rotation rate b = 1.5 cm/s for a tank with an inner radius of R = 5 cm (this constant rotation rate is equivalent to a rotation speed of 2.86 rpm). The velocity variation is maximum close to the outer wall of the tank, which is reflected in the boundary layer thickness $\delta = \sqrt{\nu/\omega}$ (Song & Rau, 2020a). However, we will show below how the small velocity variation further from the tank wall still creates shear of relevance to the ocean and aggregate fragmentation outside of the boundary layer does occur. We can use Equation (3.29) to

calculate the azimuthal velocity as a function of radius inside any oscillating roller tank so long as the appropriate speed and dimensional parameters are adjusted in the equation (*i.e.*, a, b, R, and ω) and the tank maintains a laminar, two-dimensional flow. We validated these latter two conditions experimentally and found the equation valid for dimensionless radii $\sqrt{\omega R^2/\nu}$ in excess of 35.7 (Song & Rau, 2020a), though the upper limit of validity was not determined. The operating conditions in this work corresponded to a dimensionless radius of 34.3, though many different operating conditions could be used with this method to tune the shear conditions in the tank to a particular application of interest.

3.3.2 Fluid Shear

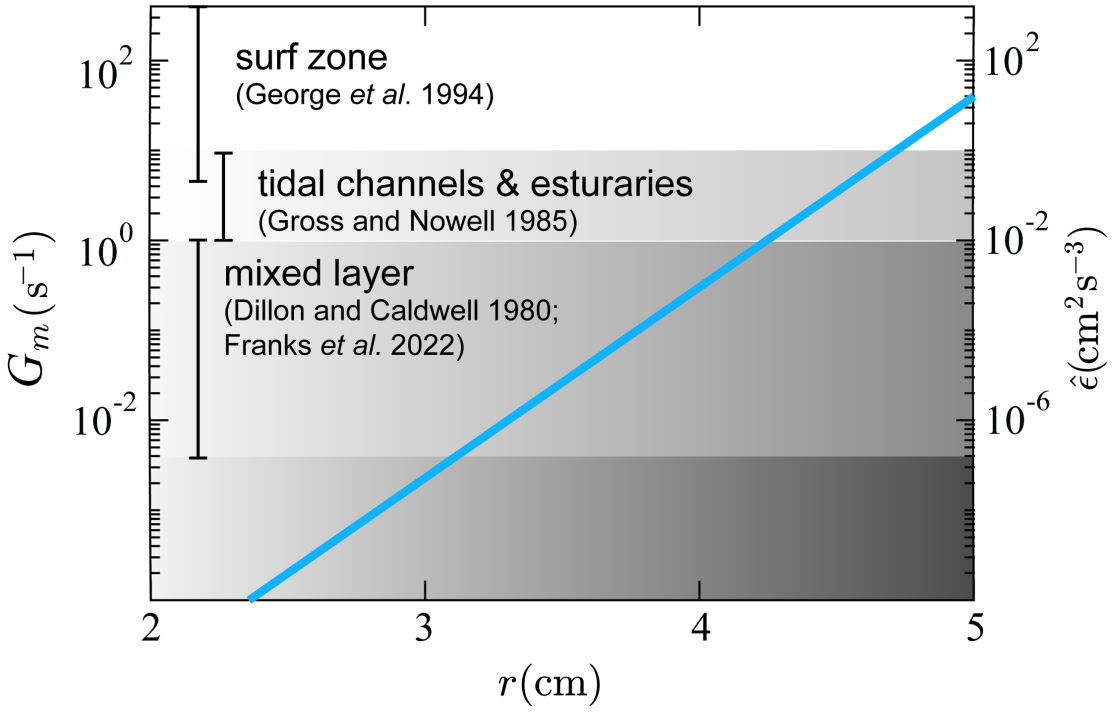

Figure 3-9: Theoretical maximum shear in the tank compared to typical shear observed in the ocean.

Knowing the fluid velocity from Equations (3.27) and (3.29), we can calculate the time-varying laminar shear, G, during FM as,

$$G = r\frac{\partial\left(u_\theta / r\right)}{\partial r}. \tag{3.30}$$

As a result of the oscillating velocity profiles, the shear rate oscillates with small amplitudes near the tank center and large amplitudes near the tank wall. Figure 3-9 shows the maximum shear rate, G_m, as a function of radius for the velocities plotted in Figure 3-8(b). Also plotted are equivalent dissipation rates, $\hat{\varepsilon}$ calculated from $G = \sqrt{\hat{\varepsilon}/\nu}$. We determine the equivalent dissipation rates by assuming that the laminar shear rate has the same order of magnitude to the average fluid strain rate in a homogeneous turbulent flow. We can compare shear in the tank to that generated in typical ocean conditions based on the ranges given by Dillon and Caldwell (1980) and Franks *et al.* (2022) for mixed-layer turbulence, Gross and Nowell (1985) for tidal channels and estuaries, and George *et al.* (1994) for surf zones. Using the prescribed conditions, the regions close to the tank wall provide high shear rates typical of the most turbulent regions of the ocean, whereas the inner regions provide shear more typical of the open ocean. We can adjust the range of shear in the tank by modifying the tank dimensions or oscillation magnitude or frequency as indicated in Equation (3.29).

3.3.3 Particle Trajectories

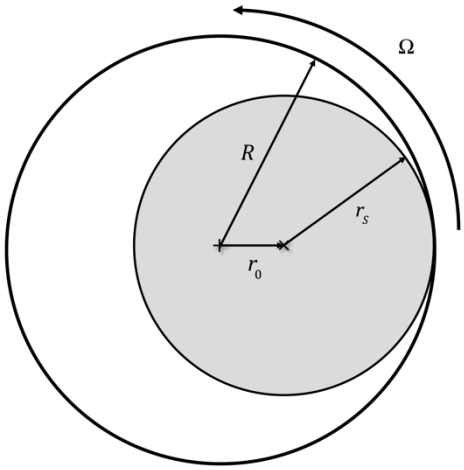

Figure 3-10: The stable region (shaded) in traditional rotating tanks.

When designing a particle aggregation system, it is important that effects of walls, pumps, impellers, etc. are minimized as they may influence the shape, structure, and strength of aggregated particles. Based on analysis of the fluid motion, the trajectory of a falling particle in a roller tank can be traced over time. The velocity of a falling particle is determined by the sum of the particle's sinking velocity and the water velocity at the particle position. For given tank dimensions, rotation rates, and particle settling velocities, it is possible to divide the tank cross-sectional area into stable and un-stable regions. Stable regions are defined as all of the initial particle positions where particles will never come into contact with the wall of the tank. Unstable regions are defined as the initial positions where the particles will eventually hit the tank wall, potentially altering their aggregation state. For tanks with a constant rotation rate, stable regions can be calculated as shown in Figure 3-10, where Ω is the angular rotation speed of the roller tank, *R* is the radius of the

roller tank and r_s is the radius of our stable region. The balance length, r_0 is obtained from the quotient of the falling velocity and the angular rotation speed ($r_0 = u_s/\Omega$). The equation $r_s = R - r_0$ then indicates the regions of the tank that are stable. The particles that begin in this region will not touch the wall of the roller tank. The area of the stable region compared to the total tank cross-sectional area is then given by $(r_s/R)^2$.

While the standard roller tank design provides a convenient way to aggregate particles through differential sedimentation, no shear forces are present in the fluid once steady solid-body rotation is achieved. We are proposing a modification to the standard design that superimposes a periodic oscillation to a constant rotation on the tank motion. The rotating and oscillating tank has several advantages for studying marine particle disaggregation. Because it is based on a rolling cylindrical tank, we can first operate the tank to aggregate particulate matter using solid body rotation in a similar manner to the facilities used to create marine snow (Shanks & Edmondson, 1989). Once aggregates are formed, we can then superimpose a harmonic oscillation at the tank wall to create dynamic shear within the fluid inside of the tank, thus exposing aggregates to shear without having to remove or manipulate the particles themselves. This allows very fragile flocs typical of the marine environment to be studied. The tank's optical transparency also permits imaging of the flocs using high-speed cameras and laser illumination to capture individual breakup processes. By optically tracking the position of each aggregate as a function of time, we can determine the exact time and position within the tank that causes breakup, allowing us to use analytical solutions describing the fluid motion in the tank to determine the shear causing breakup of each aggregate. Combining these advanced optical measurements with

particle tracking and image processing algorithms allows us to capture potentially large quantities of particle disaggregation events with unprecedented detail.

Figure 3-11 shows the numerically integrated particle trajectories for different boundary conditions and particle seeding locations. We simply assume the motion of a particle is the sum of its fall velocity and the local fluid velocity and that the direction of the gravity is perpendicular to the axis of the tank. The sinking velocity we assume is 5 m/day, which is representative of a wide range of particulate matter in the ocean (Jackson, 2015). The blue line in the left plots represent the wall of the roller tank, which has a radius of 5 cm. The red point is the initial location of an example particle within the flow as a demonstration. In each case, the tank starts at rest and begins rotating at time $t = 0$ s. To calculate stable trajectories, we ignored the particle size and seeded 100,000 particles randomly into the tank and integrated their position through time numerically. The calculation continued until unsteady trajectories were obtained or a simulation time of 15,000 seconds (4.2 hours) was reached. This timeframe was chosen for our simulations since it typically takes 3.5 to 4 hours to complete one experiment of in-lab marine snow preparations (Shanks & Edmondson, 1989). The shaded areas illustrated the stable regions within this time frame. A larger stable region is desirable as it will provide more aggregate samples for experimental analysis. We provide more detailed assessment of stable region in the next section. The plots on the right are zoomed-in views of the trajectories. Figure 3-11(a) is the reference trajectory of a randomly-seeded particle inside the standard roller tank design, which rotates with a constant speed. As shown in Figure 3-11(a), the particle rotates with a near-circular trajectory after an initial transient.

The oscillation frequency used for Figure 3-11(b), (c) and (d) are 0.02, 0.05 and 1 rad/s, with amplitudes of 0.25, 1 and 9 cm/s, respectively. Following the experiments described above, we observe there is no turbulence or instability pattern in the displayed cases. The case shown in Figure 3-11(b) is an example of an operating condition where the particle failed to reach a stable trajectory, as its starting point was outside of the shaded stable region. In this case, the particle settling velocity is large relative to the rotation speed (Re = 21.2 and η_R = 7.1), which causes it to migrate over time. In contrast, the trajectories shown in Figure 3-11(c) and (d) reach a quasi-stable state, where they both achieve a repeatable circular trajectory that does not migrate towards the tank wall. The fractional area of the stable region for the conditions in Figure 3-11(d) is estimated to be 96.1%, which means 96.1% of particles will not touch the tank wall if the particles are initially uniformly distributed in the roller tank. The stable region for the case in Figure 3-11(c) is 78.8%, while the stable region shown in Figure 3-11(b) represents an area of only 35.7% for the time simulated. When the periodic fluid motion is not significantly greater than the sinking velocity of the particles, a greater percentage of the particle trajectories become unstable within the simulation time. The irregular shape of the stable region shown in Figure 3-11(b) is likely due to the transient nature of the simulation. A longer simulation time leads to smaller stable regions within the tank. It is expected that the stable region for this case will eventually disappear after long periods of time.

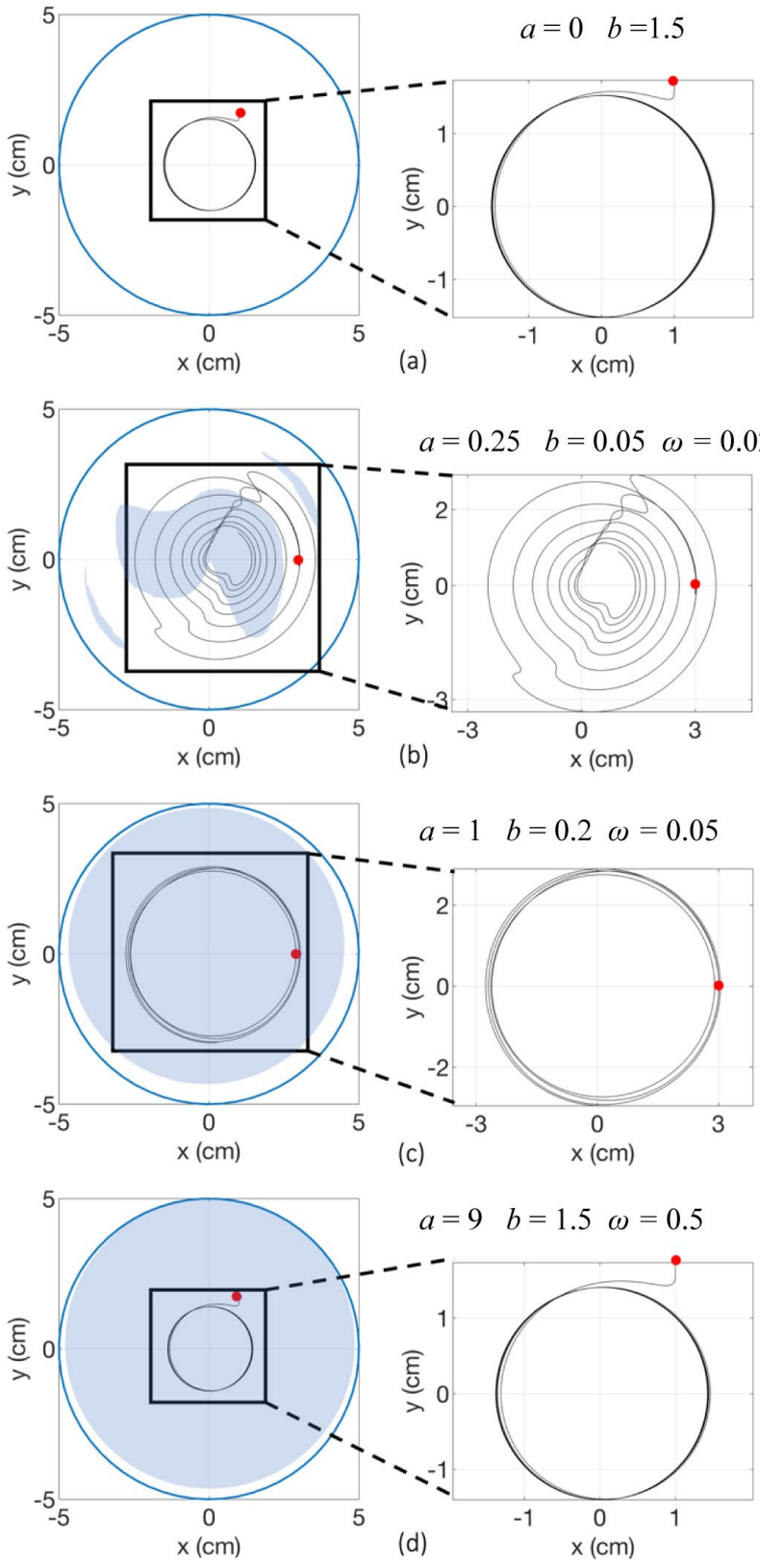
a = 0 b =1.5
y (cm)
x (cm)
(a)
a = 0.25 b = 0.05 ω = 0.02
(b)
a = 1 b = 0.2 ω = 0.05
(c)
a = 9 b = 1.5 ω = 0.5
(d)

Figure 3-11: Sample particle trajectories for (a) a constant-rotation-rate roller tank, (b-d) rotating/oscillating roller tanks with dimensionless radius η_R 7.1, 11.2 and 50.0, respectively. The Reynolds numbers Re for (b-d) are calculated to be 17.6, 2.3 and 90.0. The sinking velocity is 5 m/d (Jackson, 2015), which is a typical value in ocean.

3.3.4 Assessment of Stable Region

Jackson (2015) introduced the concept of the stable region within a roller tank that defines the region in which particles will never have contact with the tank wall. A traditional roller tank designed for aggregation has a stable region of $SR = (1 - w_s / \Omega R)^2$, where w_s is the aggregate sinking velocity, $\Omega = b/R$ is the tank rotation rate, and R is the inner radius of the tank. In contrast, defining a stable region in the disaggregation tank must consider the oscillation magnitude, a, and the oscillation frequency, ω, in addition to the constant rotation speed, b, and the tank radius, R. Furthermore, sinking velocity depends on particle size and densities (Jackson, 1994). Hence, aggregation or fragmentation ultimately affects the stable region by influencing the aggregate settling velocities. To determine tank operating conditions that would yield a sizeable stable region for a majority of the aggregates in an experiment, we investigated the influence of these variables following the Monte Carlo computational method described above. To simplify the problem, we assumed the instantaneous velocity of an aggregate was the vector addition of the local fluid velocity and the vertical sinking velocity, calculated according to Jackson (1994), regardless of its shape or structure. Then we randomly seeded 15,000 aggregates of the same size and sinking velocity into the tank and integrated their position over time

as they were exposed to the flow velocities given by Equation (3.27) in a simulated FM experiment. Two random functions distributed these monodispersed aggregates uniformly in space. The algorithm tracked each simulated aggregate until its trajectory intercepted the tank wall or the maximum simulation time is reached. Then we determined the stable region as the region bounding the starting location of all aggregates that did not impact the tank wall. We simulated up to four hours of tank operation, using a time step of 0.1 s, which more than covered the time necessary for typical fragmentation experiments.

Figure 3-12 displays the stable regions as a percentage of the tank volume and as a function of aggregate sinking velocity for the tank operating conditions used in Figure 3-9 (a = 9 cm/s, ω = 0.5 rad/s, b = 1.5 cm/s, R = 5 cm, and v = 0.01 cm^2/s). The black line shows the stable region for a traditional aggregation tank (Jackson, 2015). The rotating/oscillating conditions of the disaggregation tank result in smaller stable regions; however, large portions of the tank are still stable for aggregates with small sinking velocity. Big aggregates with a large sinking velocity inevitably have a greater chance of contacting the tank wall. We only observe a small difference in the stable region comparing three minutes and four hours of tank operating time, which indicates that wall collisions are not significantly influenced by the duration of operation in FM. To determine the influence of the tank operating conditions, we ran 94 simulated experiments, varying settling velocity from w_s = 0.006 to 0.5 cm/s (r_p = 58 μm to 2.5 mm), oscillation magnitudes from a = 0 to 15 cm/s, constant rotation rates from b = 0 to 10 cm/s, and angular frequencies from ω = 0.05 to 2 rad/s. The variation of settling speed led to a particle Reynolds number variation from 0 to 25, which covered the range of natural marine aggregates (Alldredge & McGillivary, 1991). For the tank operating conditions shown in Figure 3-9 with a particle

settling velocity of 5 m/day (0.006 cm/s), the stable region is 93.6%, which decreased as aggregate sinking velocity increased (Figure 3-12). For the same base operating conditions, varying oscillation magnitude, a, showed that the stable region varied from 93.5% to 99.2%. We also did not observe significant changes in the stable region among different rotation rates, b, and different oscillation frequencies, ω. Not surprisingly, the particle sinking velocity is the dominant factor in determining the stable region.

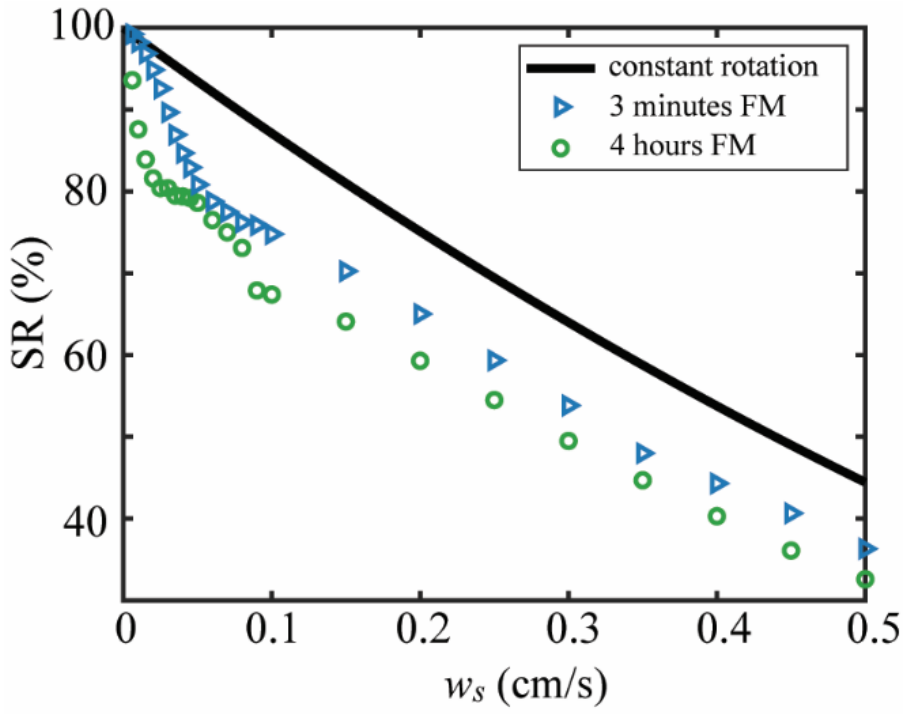

Figure 3-12: Stable regions for varying particle sinking velocities. The black line represents the stable region for a traditional aggregation tank without time limitations (Jackson, 2015). Blue and green dots are stable regions for three minutes and four hours, respectively, of tank rotation and oscillation.

3.4 Validation Disruption Experiments with Bentonite Clay

3.4.1 Experimental Methods

We have developed the experimental breakup facility as shown in Figure 3-4, which is also used here. The facility can be rotated at a slow and constant speed to simulate the differential sedimentation aggregation process (Shanks & Edmondson, 1989), or oscillated with a boundary condition of the form of Equation (3.26a) to generate fluid shear.

Bentonite clay particles readily form fractal aggregates in saline water. The fragile aggregates also easily break under the influence of fluid shear. Because bentonite flocs have seen previous investigation (Bouyer *et al.*, 2001; Rau *et al.*, 2018), we used bentonite clay particles (Naturalistix Sodium Bentonite Clay) to create aggregates in the oscillating tank facility. To fill the cylindrical tank, we first filled a larger water tank with room-temperature saline water (21 parts per thousand (ppt)), created with tap water and dissolved sea salt (Instant Ocean). We then submerged the open disaggregation tank in the larger tank and injected a solution of suspended bentonite particles through the open end of the cylinder. We quickly fixed the cylinder end cap in place underwater to prevent air bubbles from being trapped within the cylinder. To reach an overall bentonite concentration of 25 mg/L, we dispersed 3.77 g of bentonite clay particles into 300 ml of fresh water using a mechanical mixer. We used a syringe to inject 5 ml of the bentonite solution into the disaggregation tank as described above.

We created aggregates by rotating the tank at a constant rate of 2.85 RPM for approximately 4 hours and then observed their size, shape and breakup behavior using a high speed camera and laser illumination. Figure 3-4 shows the laser path and relative positions of the laser transmitter (Opus 532, Laser Quantum), high speed camera

(FASTCAM Mini AX200, Photron) and the test section. The laser had a wavelength of 532 nm and a beam diameter of 1.85 mm. We used a mirror to reflect the laser beam so that it was perpendicular to the tank axis. The beam passed through a Powell lens (75º, Edmund Optics) and a thin slit aperture to form a laser sheet that bisected the disaggregation tank. The thin slit had a thickness of 0.6 mm to minimize scattering and any diffuse reflections caused by the optical elements and tank wall. This laser sheet geometry illuminated aggregates along a central plane of the tank, allowing their azimuthal motion to be captured with the high speed camera. We observed little out-of-plane particle motion during testing.

The camera viewed the laser sheet through one end of the tank with its viewing axis perpendicular to the laser sheet. We focused the camera using a macro lens with a 200 mm focal length (AF Micro-Nikkor 200mm f/4D IF-ED). A 68 mm extension tube installed between the camera and the macro lens increased the magnification of the field of view (FOV). We estimated the FOV to be 13.5 mm × 13.5 mm (13 μm per pixel resolution with the 1024 × 1024 pixel sensor of the camera). Because this FOV was small and we were most interested in the breakup of aggregates near the tank wall, we positioned the FOV near the bottom tank wall, as shown in Figure 3-13(b). We recorded image frames as a time series at a rate of 500 fps with a shutter speed of 1/1000 s. We recorded 21,841 image frames for each experiment, which was equivalent to 43.7 s, 6.95 cycles in total.

To determine the fluid velocity and rate of shear for a specific particle breakup event, we need to know both the position and time at which that breakup event occurred. In Figure 3-13(b), a narrow curve of bright light is shown within the dashed box near the bottom of the FOV. This curve is the laser light sheet scattering from the inner wall of the cylindrical tank. Figure 3-13(a) shows the same fitting process but a different magnification rate. We

then used these center coordinates and the position of the wall to calculate the radial locations within the FOV. In this study, we quantified particle sizes by fitting an ellipse to the particle images using MATLAB. In the following sections, we report major and minor axis lengths.

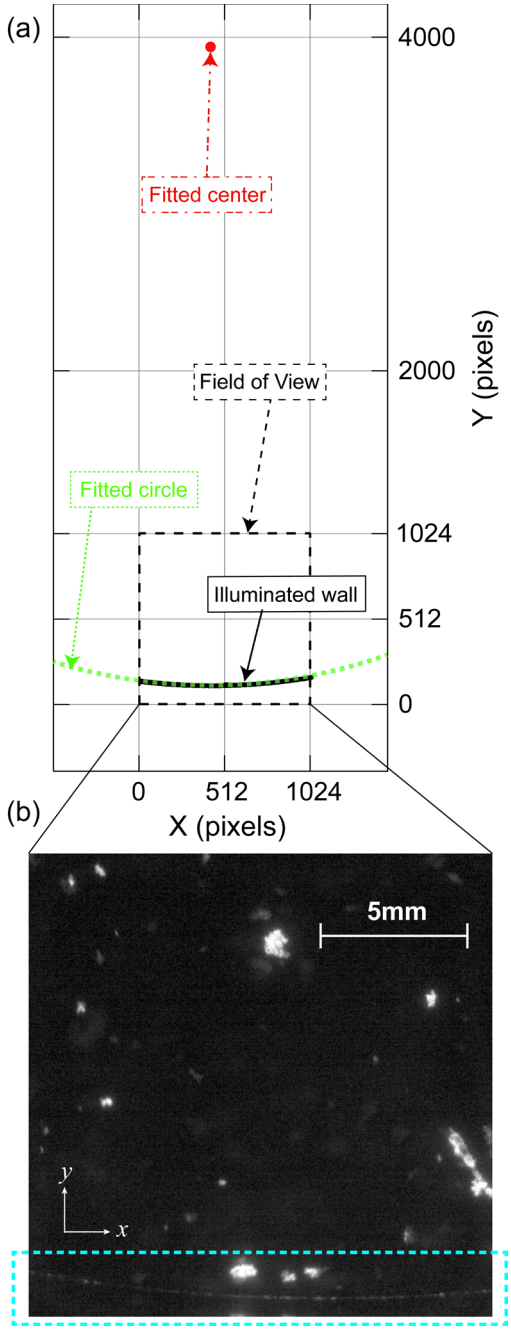

Figure 3-13: (a) The center of the cylindrical tank as determined from fitting a circle to the tank wall within the camera FOV and, (b) the illuminated bentonite aggregates and inner wall of the tank within the camera FOV.

To determine the time of each recorded image, we carefully synchronized the high speed camera recording to the tank oscillation. We defined the starting point (t = 0 s) as the time when the disaggregation tank oscillation began. To do this, we triggered the camera to record image frames at the instant the oscillating boundary condition started. We could then determine the time of each recording based on the image number and frame rate.

3.4.2 Characterization of breakup

We observed the breakup of single aggregates during the quasi-steady state motion and during the transient transition from solid body rotation to the new quasi-steady state. Figure 3-14 shows one example of breakup during the quasi-steady state, where shear forces near the wall deformed and then ruptured one aggregate. The aggregate size was small in the original FOV so Figure 3-14 displays a zoomed-in view. For reference, one full period of oscillation at these conditions is equal to 12.6 s, meaning that the shear magnitude varies with a period of 6.28 s (*i.e.* half of the period of oscillation). We can assume the flow reaches a quasi-steady state after one half period of oscillation (Song & Rau, 2020a).

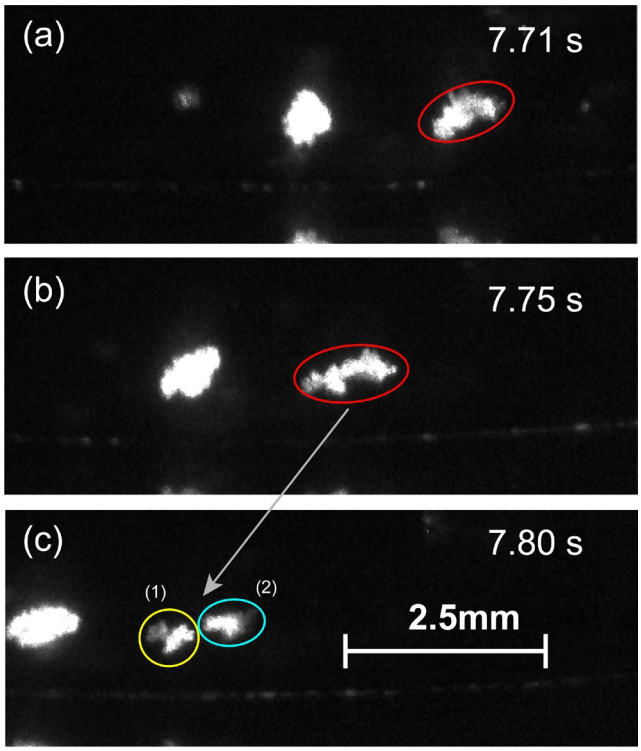

Figure 3-14: The breakup of a single aggregate into two daughter aggregates during quasi-steady state conditions.

In the first time frame t = 7.71 s (Figure 3-14(a)), we observed two aggregates. The right-most aggregate had a major axis of 765 μm and a minor axis of 338 μm, as determined by fitting an ellipse to the aggregate image. After 0.04 s (Figure 3-14(b)), the aggregate elongated along its major axis, extending to 1,010 μm. The minor axis, as a result of this stretching, reduced to 270 μm. Figure 3-14(c) then shows that this aggregate ruptured at t = 7.80 s, becoming two daughter sub-aggregates, labeled (1) and (2) in Figure 3-14(c). The size of the sub-aggregates was roughly the same, with major- and minor- axes of 484 μm × 259 μm and 529 μm × 236 μm. However, due to the limitation of this facility, we could not estimate the out-of-plane thickness or volume of the aggregate.

We calculated the radial position of this aggregate undergoing breakup by its geometric center. It was 4.93 cm away from the center of the tank. Based on this position and the phase angle of the disruption event in Figure 3-14(c), we estimated the shear rate that caused this breakup to be $16.1 \cdot 10^{-3}$ Pa based on the equation of laminar fluid shear $r\frac{d\left(u_\theta / r\right)}{dr}$. Interestingly, the other (left-most) aggregate shown in Figure 3-14(a-c) does not disrupt despite it being a similar size and experiencing a similar shear to that of the disrupting aggregate.

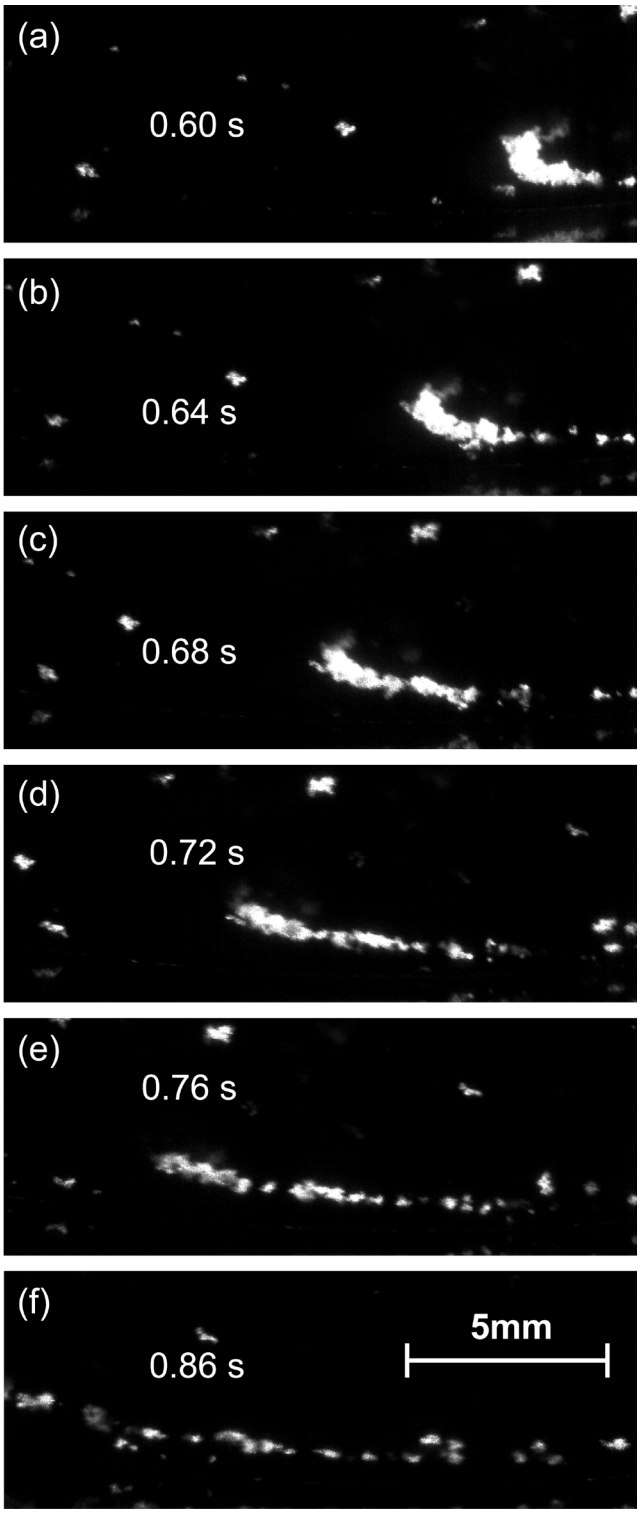

Figure 3-15: The breakup of a very large aggregate into many sub-aggregates during the transition to oscillatory conditions.

Figure 3-15 shows the breakup of a large aggregate during the transient motion that occurred just as the tank oscillation started. The large aggregate disrupted into many sub-aggregates, leaving a trail of fragments from t = 0.60 s to 0.86 s. We determined the size of this aggregate as it entered the FOV in Figure 3-15(a) by fitting an ellipse to the aggregate image. The major axis was initially 2,160 μm with the minor axis 1,260 μm. Because there was no radial shear stress in this flow configuration, the azimuthal shear quickly elongated the aggregate and shortened the minor axis, as shown in Figure 3-15(b) and (c). In this case, the aggregate was not strong enough to maintain plastic deformation under the imposed shear field. As a result, small fragments started breaking off, as shown in Figure 3-15(b-f). Once the original large aggregate had completely fragmented, all remaining sub-aggregates, shown in Figure 3-15(f), had a similar size of approximately 117 μm long. We estimated the location of this disruption in Figure 3-15 to be 4.96 cm away from the center, calculated from the geometric center of the large aggregate. The shear rate increased from $30.7 \cdot 10^{-3}$ Pa in Figure 3-15(b) to $37.5 \cdot 10^{-3}$ Pa in Figure 3-15(f).

During experimentation, aggregates tended to break apart more readily during the startup period of the oscillation than during the quasi-steady oscillation as the shear rates were much greater during this transition. This is also evident by comparing the breakup event of one aggregate into two in Figure 3-14 to the total fragmentation of a large aggregate in Figure 3-15. Before the oscillation began, aggregation through solid body rotation produced aggregates with a wide range of sizes. However, the largest aggregates in the flow typically could not survive the transition from solid body rotation to the quasi-

steady oscillation. As a result, we plan to pursue more-gentle transitions between the two states so that the breakup behavior of the largest aggregates can be studied.

3.4.3 Observation of Aggregation

One difficulty of studying particle disaggregation is that aggregation and disaggregation both occur due to fluid shear. We did observe aggregation of small particles during the breakup experiment. Figure 3-16 shows the aggregation of two sub-aggregates. The two sub-aggregates, labeled (1) and (2) in Figure 3-16(a), were initially very close to each other in Figure 3-16(a) and similar in size. Their major axes were 475 μm and 422 μm and their minor axes were 277 μm and 237 μm, respectively. In Figure 3-16(b), they came into contact due to a small difference in azimuthal velocity. We observed that both sub-aggregates also had slightly different angular velocities, which they maintained until they were fully connected. In Figure 3-16(d), they started to share the same rate of rotation and we considered this moment as the completion of this aggregation event. The newly formed aggregate had a size of 685 μm by 542 μm. At the average radial position of the two sub-aggregates, they were exposed to a shear rate of $0.35 \cdot 10^{-3}$ Pa, which is much lower than the shear rates needed to cause the breakup events that were shown in Figure 3-14 and Figure 3-15.

There are three main mechanisms to form marine aggregates which are described in Chapter 1: Brownian motion, shear contact and differential sedimentation (Jackson, 1994). Traditional aggregation tanks only include differential sedimentation through solid body rotation (Shanks & Edmondson, 1989). Figure 3-16 shows that this rotating and oscillating

facility can make aggregates from fluid shear in addition to causing breakup. Similar to the process of differential sedimentation, the aggregation due to fluid shear starts from a collision. When two or more sub-aggregates have a small enough difference in velocities and rotation rates, they collide such that surface forces can bond them together, creating one larger aggregate.

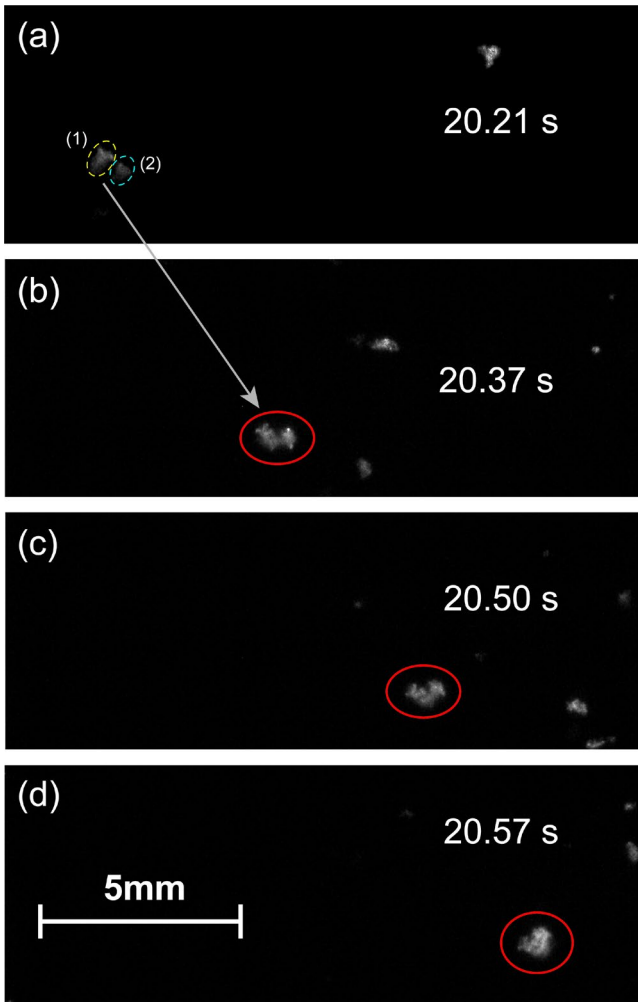

Figure 3-16: Aggregation of two smaller particles and the plastic deformation of the aggregate.

3.5 Summary

We have developed the analytical solution for the oscillatory flow inside a cylinder whose wall undergoes a harmonic oscillation, and have successfully validated the quasi-steady solution experimentally for a cylinder with a dimensionless radius of $\eta_R = 35.7$. Similar to the solution for a flat plate or the flow outside of a cylinder, we show that the amplitude of fluid velocity oscillation decreases rapidly as we move away from the wall. This decay in amplitude is accompanied by a phase lag in velocity compared to the wall boundary as distance from the wall increases. At the same time, the transient effects from the initial startup condition decay rapidly and almost vanish within the first cycle of oscillation.

Unique to our solution is the need to define two finite boundary conditions, the velocity at the outer wall and at the center of the cylinder. These boundaries result in a finite radial range and mean that the cylinder size influences the overall solution. The dimensionless radius of the cylinder, which is shown to be proportional to the product of Reynolds number and Strouhal number characterizing this flow, determines the thickness of the high velocity regions near the cylinder wall. For large cylinders, the penetration depth approaches Stokes' solution for a flat plate. If the size of the cylinder approaches that of, or is smaller than, the characteristic viscous length scale of the flow, viscous forces dominate and solid body rotation within the cylinder results.

We present a rotating and oscillating tank to study the breakup of aggregated marine particulate matter. This novel disaggregation tank provides a range of laminar shear rates

that are relevant to the ocean, with the maximum shear capabilities similar to those observed near the ocean surface due to turbulence. By tracking particle positions as a function of time, we can determine the shear rate that causes specific disruption events using the analytical solution of a viscous flow inside an oscillating cylinder.

However, a few open questions remain. The facility likely does not capture the length and time scales of turbulence observed in the natural environment. Additionally, aggregate elongation may play an important role during breakup. To further refine this experiment, we plan to develop algorithms to automatically detect events of aggregate elongation and breakup in large image datasets so that they can be statistically analyzed in the context of naturally-occurring ocean turbulence. We will also expand our particle material types to include additional inorganic and organic marine particles to best represent aggregates of relevance to coastal- and open-ocean regions. These capabilities will allow us to build a large database of aggregate disruption parameters for future modeling efforts.

Chapter 4

Statistical Analysis of Individual Phytoplankton Aggregate Breakup in Controlled Shear Flow

In this chapter, we develop an automated algorithm for particle tracking and breakup detection. With high-speed imaging techniques, we obtain individual breakup events and population statistics of cultured diatom aggregates. Most of the work is published by Song and Rau (2022).

The chapter is organized into four subsequent sections. Section 4.1 describes the preparation of diatom aggregates and methodology of the tank operation and image processing procedures. In Section 4.2, we perform an assessment of the method by investigating individual breakup events and statistical results. Additionally, we discuss the breakup strength of the diatom aggregates we used. Section 4.3 discusses the advantages and potential improvements of the facility and method. In Section 4.4, we adjust the experimental procedures and measure the time-varying responses of diatom aggregates to the shear flow. This supplemental work provides more insights into fractal dimensions and breakup rates of cultured aggregates. Lastly, Section 4.5 makes concluding remarks.

4.1 Materials and Methods

4.1.1 Experimental Facility

The experimental facility presented in Chapter 3 was adapted for additional fragmentation studies. The tank was long enough to have a two-dimensional flow along

the central tank cross-section (Song & Rau, 2020a). In Figure 4-1, an LED light panel (StudioPRO S-1200D, Fovitec) shone through a slit aperture (10 mm wide) to illuminate suspended particles along the central tank cross-section. We mounted a high-speed camera (FASTCAM Mini AX200, Photron) with its viewing axis perpendicular to the resulting light sheet. The camera captured particle motion through a macro lens with a 105 mm focal length (Sigma 105mm f/2.8 EX DG).

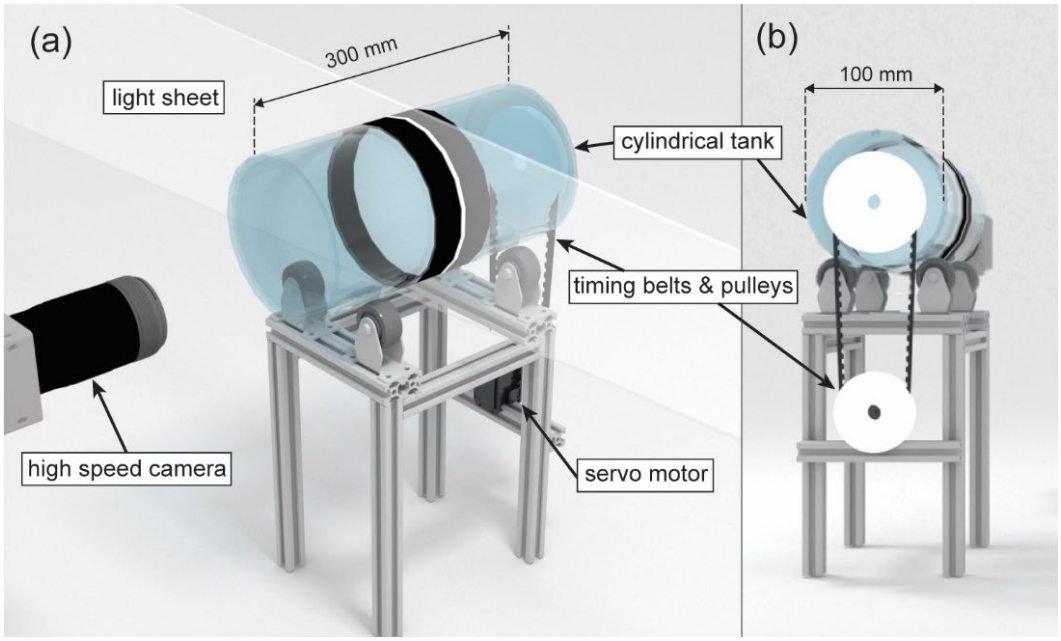

Figure 4-1: Schematic diagram of the experimental facility.

The servo motor allowed us to vary and control the tank rotation speed. The roller tank was in its Aggregation Mode (AM) when we operated the tank at a constant rotation rate. We found that the Odontella aurita aggregated quickly in AM and formed large, stable aggregates through differential sedimentation after about three hours of operation. This aggregation time is similar to the aggregation time used in prior work (Shanks &

Edmondson, 1989) and all of our fragmentation experiments started with three hours of AM operation. Once diatom aggregates were formed, we initiated the Fragmentation Mode (FM) by superimposing a harmonic oscillation to the tank rotation. This continuously varied the speed of the outer tank wall, as shown in Figure 3-9(a), which caused an oscillating laminar boundary layer to form around the tank circumference (Song & Rau, 2020a). Detailed mathematical formulations of velocity profiles, fluid shear, and stable region calculations were presented in Chapter 3. The rotation and oscillation created time-varying fluid shear due to a velocity gradient that extended inwards towards the center of the tank. This dynamic creation of velocity gradients in the tank allowed us to directly expose aggregates to hydrodynamic shear without handling or moving them to a second facility.

To perform an experiment, we first filled the cylindrical tank with cultured algae at a concentration of approximately 46,000 cells ml^{-1} and filtered seawater (Gulf of Maine Seawater, Bigelow NCMA, 30 parts per thousand (ppt) salinity), being careful to fill the tank fully so that no air was trapped after the tank end cap was secured. We could use other concentrations, but we found this level to be a good compromise between having enough algae to quickly form large aggregates while also not too many to prevent good optical access within the tank. The low concentrations and relatively small excess density of the particles also ensured that the bulk flow of the tank was not modified by the particle suspension. We then aggregated particles in AM for three hours. After we formed aggregates, the roller tank oscillated in FM while we recorded images with the high-speed camera until its memory was full.

4.1.2 Imaging Methods

Example color pictures of the experiment taken with a digital camera are shown in Figure 4-2. The phytoplankton prior to aggregation are shown in Figure 4-2(a), with Figure 4-2(b) and (c) showing the resulting aggregates after three hours of AM operation, and after 174.7 seconds of FM operation, respectively. To resolve time-varying morphological changes and breakup, we utilized a high-speed camera and bright illumination for the actual aggregate tracking experiments. We illuminated aggregates using the LED light panel and a slit aperture as described above.

The camera focused on illuminated aggregates through one end of the cylindrical tank. Figure 4-2(e) and (f) show the resulting grayscale images of the aggregates in AM and FM, respectively. To calibrate the camera magnification as it viewed through the polycarbonate and seawater, we 3D printed a circular calibration plate as shown in Figure 4-2(d). The plate had a diameter of 100 mm, with 8 mm horizontal and vertical spacings between adjacent dots. This calibration plate had a high finishing level with a tolerance of 0.002 inches (0.05 mm). Magnification varied from 10.28 px/mm at the back of the light sheet to 10.40 px/mm at the front, which gave us a mid-sheet magnification of 10.34 px/mm with an uncertainty of ± 0.57%. We used this magnification for all subsequent calculations.

We recorded image frames at a rate of 125 fps with a shutter speed of 1/1000 s. For each experiment, we recorded 21,841 image frames, equivalent to 174.7 s. The high-speed camera started recording simultaneously with the change in tank motion from AM to FM and was controlled using an Arduino Uno board. We estimated that the delay between the camera trigger signal and the actual change in the motion of the varying-speed motor was

5.5 ± 2.5 ms. The signal delay resulted in uncertainty in determining the phase angle corresponding to each image of up to 8.36×10^{-4} rad.

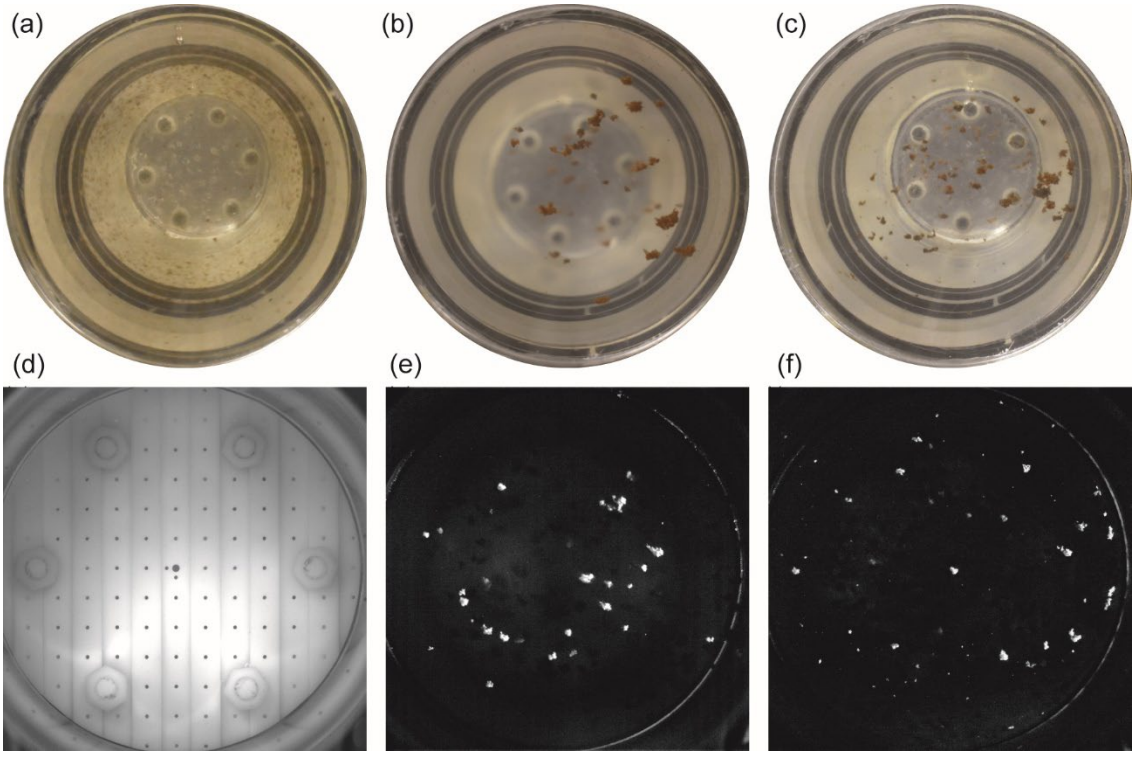

Figure 4-2: Pictures of the phytoplankton (a) prior to aggregation, (b) after three hours of aggregation in AM, and (c) after 174.7 seconds in FM. The circular calibration plate used to determine magnification is shown in (d). High-speed images used for analysis are shown in (e) for aggregates in AM and (f) aggregates after fragmentation in FM.

4.1.3 Imaging Processing Procedures

4.1.3.1 Background Removal

Time-dependent light reflections caused a nonuniform background in our experimental images, as shown in Figure 4-3(a), which complicated the particle identification and matching. Before particle identification, we removed the background of the grayscale images using the proper orthogonal decomposition (POD) method initially developed by Mendez *et al.* (2017) for particle image velocimetry. One complication occurred for particles with slight motion inside the tank, which could be mistakenly considered part of the background due to their very small displacement. To avoid this, we used every 100th image in each series for the POD analysis, which exaggerated the motion of the particles for more consistent background detection.

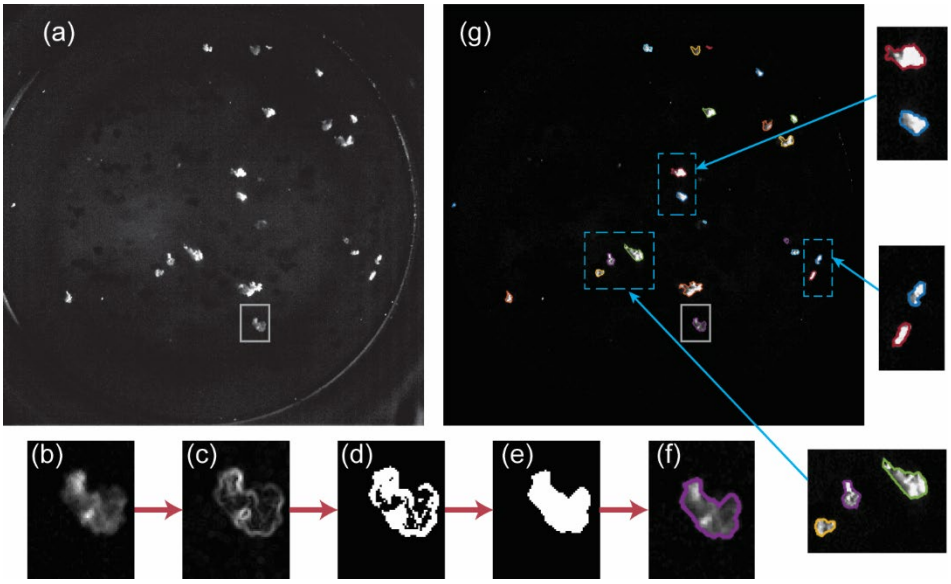

Figure 4-3: Grayscale images of aggregates (a) before applying a static mask and background removal, (b), (c), (d), (e), (f) major steps for binarization and edge detection, and (g) after the particle identification. The image in (g) shows the same aggregates as

those in (a). Samples of particles with their exterior boundaries after the identification are provided next to (g).

4.1.3.2 Particle Identification

Capturing the 2D morphology of marine aggregates is challenging given that they can deform and have fractal features that influence their illumination, as shown in Figure 4-3(a) and (b). We developed a practical binarization approach to deal with the nonuniform background and blurry aggregate boundaries to get around these issues. This method applied a locally adaptive black-and-white threshold to obtain the morphology of individual particles. First, we segmented the gray image into smaller sub-images, as shown in Figure 4-3(b), and eliminated out-of-focus particles based on their grayscale intensities. Next, we calculated the grayscale intensity gradients shown in Figure 4-3(c) and applied the local adaptive binarization (Figure 4-3(d)). After a dilation-and-erosion step (Figure 4-3(e)), we captured the shape of every particle remaining in the image. Finally, we masked all individual gray images of particles (Figure 4-3(f)) for the subsequent particle matching process. An example final image is shown in Figure 4-3(g) with a few zoomed-in particle images next to it. Further details of these image processing steps are provided in Appendix B.

4.1.3.3 Particle Matching

We developed an aggregate matching algorithm to track morphological changes and breakup events of individual aggregates over time. Before the matching began, we assigned each aggregate in the first frame of the image time series a unique identifying number. Then the algorithm searched for matches to each of these aggregates in the subsequent frames, as described below. Individual aggregates were tracked as long as matches could be identified in subsequent images. As new aggregates entered the field of view (*i.e.* aggregates that could not be found in previous frames), new unique identifying numbers were assigned. The algorithm continued in this fashion until the entire image time series was processed and all unique aggregates were identified. The four major steps of this algorithm are outlined below and also summarized in Figure 4-4(a). For ease of explanation, consider an aggregate image in one frame, called here aggregate *A*, being matched with a candidate aggregate image in another frame, called here aggregate *B*:

1. The algorithm first identified if aggregate *B* could be a potential match based on its location. More specifically, we eliminated all possible matches that would require radial motion that exceeded the maximum aggregate sinking velocity, estimated from $w_s = 2\xi r_p^{1.17}$, where the sinking velocity w_s was determined by the effective radius, r_p, and constant $\xi = 1.24$ cm$^{-0.17}$s^{-1} (Jackson, 1994).
2. The second step required that the absolute displacement between aggregate *A* and aggregate *B* be smaller than the distance determined from the maximum fluid velocity inside the tank. This step reduced the number of potential matches to only those in the near vicinity to aggregate *A*.

3. We then evaluated the remaining candidates by calculating the minimum quadratic difference (MQD) between the sub-images of aggregate *A* and all possible matches. In short, the MQD quantifies the differences in pixel intensities between two images, with the minimum value obtained where two similar grayscale patterns are most aligned. Researchers widely consider MQD for PIV displacement measurement (Merzkirch & Gui, 2000; Wieneke, 2015) and motion estimation based on computer vision (Yuan & Shen, 2008). In our matching analysis, small MQDs meant that the images of aggregate *A* and *B* had similar shapes, sizes, and intensities and was an indication of a successful match. We considered the match to be successful if the MQD was less than two times the standard deviation of the grayscale intensities of the entire gray image. We used this value as the reference background noise.
    a. If the MQD of all candidate matches was not small enough to meet the matching requirement, we then also evaluated the MQD ratio, MQD_R. We defined this parameter as the ratio of the MQD to the sum of all gray pixel intensities of both aggregate sub-images squared. We considered two aggregates matched if $MQD_R < 0.1$. In general, matching of smaller particles worked better using the MQD criterion, while using the MQD ratio had a better performance for larger aggregates that could deform from frame-to-frame. We have provided the details of how to calculate MQD and MQD_R in Appendix C.
4. A final matching step was necessary to handle the smallest observed aggregates. The images of most small aggregates were similar to one another since they were

not large enough to display very unique morphologies. Thus, it was possible that multiple small aggregates close to one another could be flagged as potential matches to a small aggregate in a previous frame. Therefore, if multiple candidates for the match to aggregate *A* were still available at this step, we simply assumed that the best match was the aggregate with the smallest MQD value.

Two illumination challenges complicated this aggregate image matching procedure. First, illuminated aggregates within the light sheet could flow next to one another, briefly causing an image of a combined aggregate. Second, large unilluminated aggregates between the light sheet and the camera could briefly obscure the camera image. To prevent these events from interfering with the tracking of illuminated aggregates, we repeated the matching algorithm described above between five subsequent frames. In other words, particles would still be matched if we lost information for up to four consecutive frames. The matching procedure described above worked well (e.g., in one experiment 642,721 aggregates were identified, which reduced to 76,357 unique aggregates after the particle matching procedure).

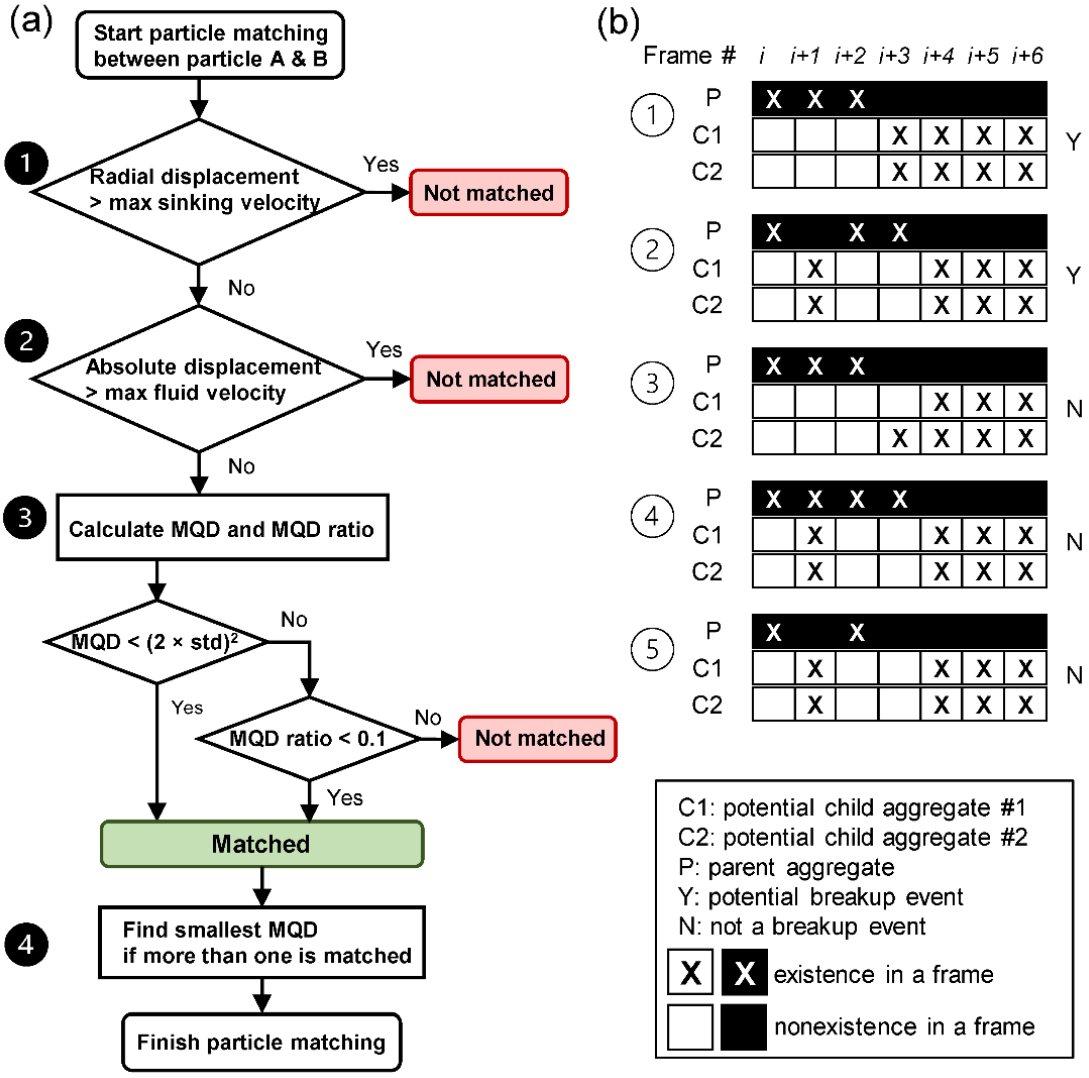

Figure 4-4: (a) a flow chart that summarizes the four major steps of our particle matching algorithm, and (b) diagrams of the time-series correlation used to detect breakup events, showing five example cases of the detection of a parent and child aggregates in the image frames.

4.1.3.4 Breakup Detection

Once the history of each aggregate was determined through the above matching algorithm, we could rely on the time-series information to detect breakup events. The basic algorithm relied on the fact that the births of two child aggregates must immediately follow the death of one parent aggregate. This case is shown schematically as Case 1 in Figure 4-4(b). In the early stages of a breakup event, the slight gap between two child aggregates could sometimes not be detected based on the illumination. This resulted in the breakup event taking multiple frames to be detected, with the child aggregates sometimes re-detected as a single parent aggregate for a few frames (up to 40 ms). Case 2 in Figure 4-4(b) illustrates a valid breakup event, including binarization and particle detection error. In these cases we assumed breakup occurred at the first frame where the two child aggregates were detected. In contrast, we ignored cases if two child aggregates were not born simultaneously (Case 3), if the parent and child aggregates appeared in the same frame (Case 4), or if all aggregates were missing in at least one frame (Case 5). Finally, we only analyzed breakup events where the lifespan of the parent and child particles was greater than 15 frames (> 0.12 s). This restriction conservatively eliminated short-lived aggregates from our analysis. The tracking lifespan of the aggregates analyzed in this study generally ranged from 15 to over 2,000 frames, with an average of 78 frames.

Despite the rigor of the breakup detection algorithm, some aggregate images were still mistakenly identified as breakup events, for example, two aggregates passing in front of or behind one another. Thus, while the algorithm efficiently identified all possible breakup events in our aggregate populations, we also performed a manual check visually for all breakup events to ensure accuracy. This was reasonable given the relatively rare occurrence

of breakup events in the time series. We provide the detailed rubric used for the manual check in Appendix D.

4.1.4 Phytoplankton Culture

We cultured Odontella aurita v minima (UTEX LB 3038) at a light intensity of 30 μmol m^{-2} s^{-1} on a 12:12 hour light/dark cycle. We used filtered seawater (Gulf of Maine Seawater, Bigelow) and f/2 medium (Sigma-Aldrich) for the nutrients. The salinity was 30 ppt. During the culturing stage and experiment, we maintained the cultures at a room temperature of 20.9 ºC (+1.2 / -2.5 ºC). We prepared the same treatment mediums using an autoclave and inoculated the culture into Erlenmeyer flasks based on their growth phase. This type of species has an average length of 45 μm and a width of 10 μm. We determine the equivalent spherical diameter of the culture used in our experiments to be 15 μm from obtained micrographs.

4.2 Assessment of the Method

4.2.1 Individual Aggregate Breakup

One of the great advantages of this experimental method is that it can capture the time-varying response of individual aggregates to shear exposure, including their morphological evolution up to and following breakup and the breakup event itself. Figure 4-5 provides one example fragmentation event of an aggregate with an equivalent diameter of 2.89 mm. Figure 4-5(a), (b), and (c) present the example sub-images of the parent aggregate and the

two child aggregates before and after breakup. We list the experimental frame number for each image for reference, with a frame number equal to one representing the first image obtained after the tank started to oscillate. For this breakup event, we observed that the shadow created by other aggregates in the front of the tank blocked the parent aggregate at a frame number from 4,588 to 4,608 (Figure 4-5(a)). This aggregate started to elongate due to the shear exposure at a frame number of 4,628 (t = 37.02 s). The breakup detection determined that this parent aggregate became two separate parts at a frame number of 4,755 (t = 38.04 s), as shown in Figure 4-5(b) and (c).

The image processing steps allowed us to calculate morphological parameters, including equivalent diameter, d_{eq}, major and minor axis length of a fitted ellipse, L_{ma} and L_{mi}, and aspect ratio, AR, where the aspect ratio was defined as the ratio of the major axis length to the minor axis length. We determined the equivalent diameter based on the projection area of an illuminated particle. Figure 4-5(d) shows the local shear rate, calculated at the aggregate centroid, the time-varying major axis length, and the time-varying aspect ratio, plotted as a function of time for the aggregate shown in Figure 4-5(a)-(c). Initially, the parent aggregate experienced low amounts of shear, which increased slightly after t = 37.02 s and then more significantly after t = 37.66 s as the aggregate settled into a near-wall region of the tank. The major axis length and aspect ratio did not increase significantly until this more considerable shear exposure, after which it elongated from L_{ma} = 2.83 mm to 5.71 mm. This corresponded to a change in aspect ratio from 1.46, representing a relatively circular shape, to 2.96, representing an elongated ellipse. The aggregate broke into two smaller pieces, similar in size, at t = 38.04 s at a shear rate of 13.91 s^{-1}.

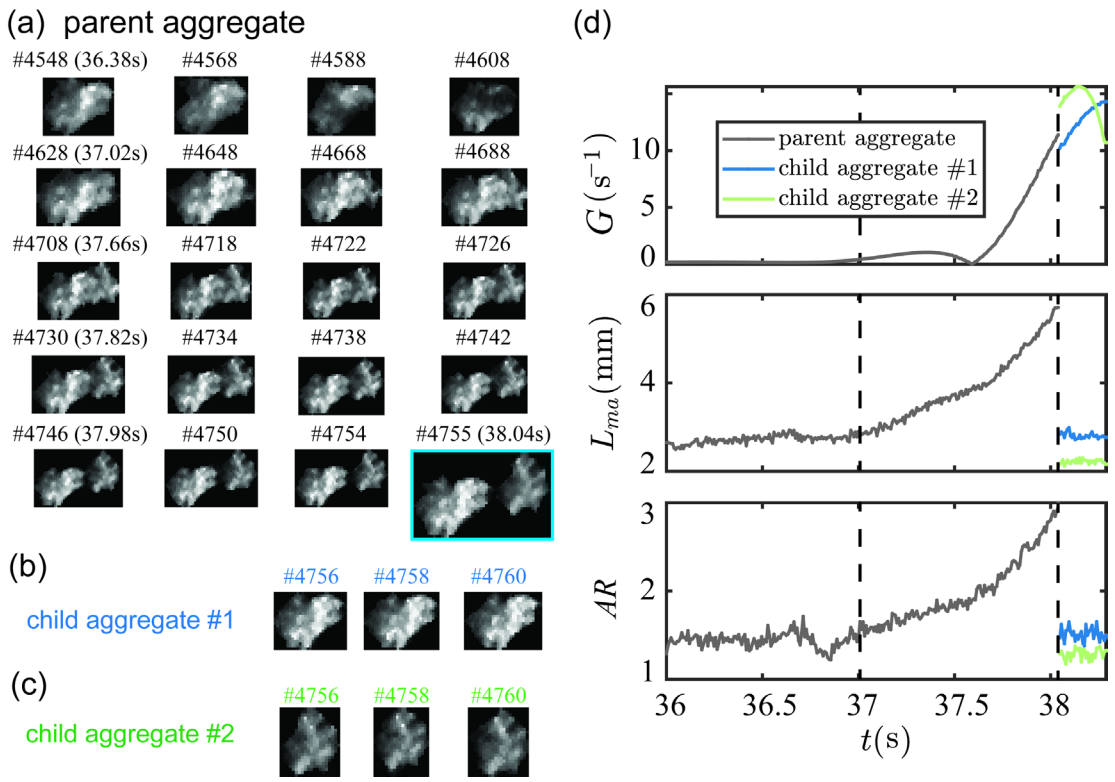

Figure 4-5: Time series of (a) a parent aggregate elongating and breaking into the two child aggregates shown in (b) and (c). The time-resolved shear exposure of the aggregate and its resulting change in major axis length and aspect ratio are shown in (d).

4.2.2 Statistical Fragmentation Results

In addition to resolving the time-varying response of individual aggregates, the automated particle tracking algorithm allows us to process many aggregates and investigate entire particle population statistics. We repeated the disaggregation experiment described above twenty-five times, starting each time with a new culture of Odontella aurita, and analyzed the resulting aggregate images. From these experiments, 180,682 aggregates were suitable (*i.e.* had the appropriate lighting and lifespan of greater than 15 frames) to be

analyzed by our breakup detection algorithm. Figure 4-6(a) displays the locations of the resulting 79 confirmed breakup events in the tank cross-section. Most breakup events occurred near the tank wall, where shear rates were high, as expected. It should be noted that we excluded any aggregates that were observed in contact with the wall from our analysis (see Appendix D). We found that wall contact was rare and did not account for any confirmed breakup events in our experiments.

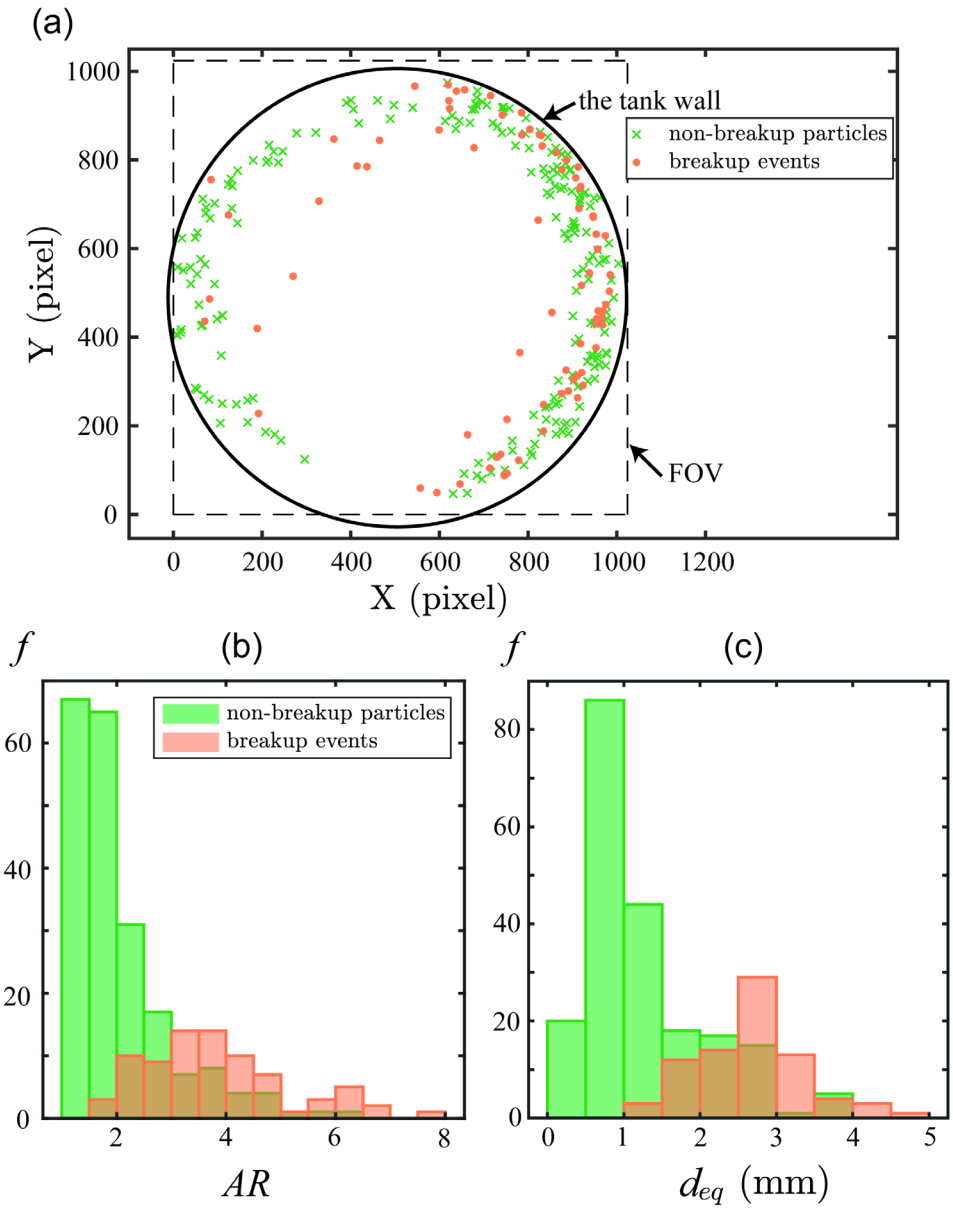

Figure 4-6: (a) locations of breakup events with 200 randomly selected non-fragmenting aggregates with similar shear exposure. Frequency histograms of (b) aspect ratios and (c) sizes of the fragmenting aggregates at breakup and the plotted non-fragmenting aggregates.

For comparison, we randomly selected 200 additional aggregates that did not fragment and also plotted them in Figure 4-6, shown as the green crosses. To have similar local fluid shear to the fragmented aggregates, we only considered non-fragmenting aggregates located within one centimeter from the tank wall. Figure 4-6(b) and (c) show the frequency histograms of aggregate aspect ratios and sizes. Disrupted aggregates had larger sizes on average and were more prone to deformation. Fragmenting aggregates tended to have higher aspect ratios than non-fragmenting aggregates, indicating that aggregate shape is an important parameter in its fragmentation, though this result was not universal. It is worth mentioning that some aggregates that had an aspect ratio of up to six did not fragment, though most aggregates with aspect ratios above three did fragment.

In addition to analyzing individual breakup events, the images acquired from the tank can be used to build snapshots of the aggregate population and its shear exposure. Figure 4-7(a) shows a pseudo color map of the distribution of aggregate sizes as a function of their instantaneous shear exposure from one experiment. Here, unique particles were sampled by taking all aggregates observed in every 100^{th} image of the high-speed image sequence, which started after three minutes of operation in FM. The population was not sampled using the time-series restrictions used to detect aggregate breakup so that aggregates with lifespans of less than 15 frames could be analyzed. A total of 146,190 unique particles are

displayed in Figure 4-7(a). Aggregate sizes ranged between 0.3 mm (our detection size limit) and 3 mm. This upper limit was based not on our optical detection method but the tank's aggregation and fragmentation conditions. The color map also shows that more particles inside the disaggregation tank were preferentially located in regions where the local shear rate was 10^{-2} to 10^{-1} s^{-1}. At shear rates higher than this, the number of large aggregates decreased, which is consistent with fragmentation. We did not observe many aggregates where the shear range was smaller than 10^{-3} s^{-1} as this region was small and experienced weak fluid motion.

From the data presented in Figure 4-7(a), we extracted traditional particle size distributions (PSD) for aggregates exposed to similar shear rates. This is similar in concept to the PSDs presented in the literature (Spicer and Pratsinis 1996; Rau *et al.* 2018; Ackleson and Rau 2020). Figure 4-7(b) shows normalized volume fractions, V_f, of aggregates for three ranges of shear exposure, where the volume fraction of each size range, $V_{f,D,\gamma} = \sum_{i\in\{D,\gamma\}} D_{eq,i}^3 \Big/ \sum_{j\in\{\gamma\}} D_{eq,j}^3$, was calculated based on the equivalent diameter and the same shear bin. The relative volume of large particles decreased with increasing shear exposure. Meanwhile, the volume fraction of smaller particles increased. This change in the volume PSD with increasing shear is consistent with other aggregate breakup studies (Rau *et al.*, 2018; Tang *et al.*, 2000).

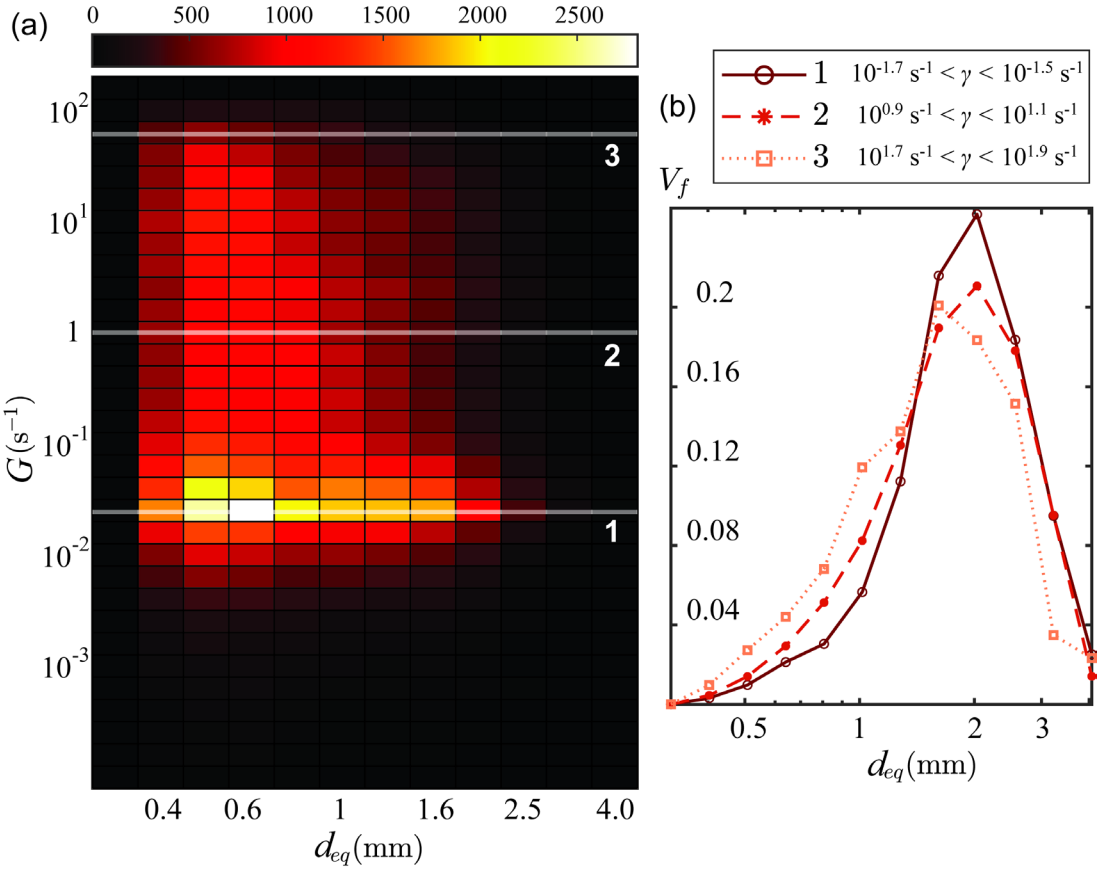

Figure 4-7: (a) a pseudo-color plot of the number of unique particles with respect to local fluid shear and equivalent diameter and (b) normalized volume fraction versus equivalent diameter for the three selected ranges of local fluid shear. The data plotted in (b) correspond to the numbered horizontal lines shown in (a).

4.2.3 Breakup Strength of Aggregated Diatoms

We determined the breakup strength of one particle, σ_b, by assuming that it was equal to the fluid stress, σ_f, experienced by that aggregate at the breakup instant, where $\sigma_f = \mu G$ was calculated at the aggregate centroid. This stress calculation is similar to that employed by

Saha *et al.* (2016). The Odontella aurita aggregates in this study displayed a wide range of strengths ($10^{-5} < \sigma_b < 10^{-1}$ N m^{-2}) even though only a fairly narrow range of aggregate diameters were sampled ($1 < d_{eq} < 5$ mm). This variability was likely due to several reasons. First, although we cultured the Odontella aurita under identical conditions and started with a fresh population for each experiment, the phytoplankton in each experiment could have varied in terms of their stress level, biopolymer (*i.e.* Transparent Exopolymer Particles production), and overall cohesiveness (Azetsu-Scott & Passow, 2004). Second, we assumed that the fluid stress was equal to the aggregate strength at the breakup instant. In some cases where the fluid stress increases more rapidly than the aggregate could respond, it is conceivable that the fluid stress exceeded the strength of the aggregate. Finally, the strength of aggregates is known to be highly dependent on their morphology, in particular their fractal dimension (Burd & Jackson, 2009). Given that aggregates from other studies, including both diatom aggregates (Alldredge *et al.*, 1990) and aggregates of polymer beads (Bache *et al.* 1997; Zaccone *et al.* 2009; Saha *et al.* 2014), have shown similar variability in strength, it is most likely that the variation in our results was largely due to variations in aggregate morphology.

In Figure 4-8 we compare our breakup results with the strengths of various types of aggregates reported in other studies (Alldredge *et al.* 1990; Bache *et al.* 1997; Zaccone *et al.* 2009; Saha *et al.* 2014; Song and Rau 2020b). Overall, the aggregate size was most important to determining aggregate strength. The breakup strength of diatom aggregates seemed to follow a larger general trend, where the strength followed a logarithmic decay as aggregate size increased. The trend appeared to also apply to different types of aggregated particles materials (clays, polymer beads, and diatoms) in addition to diatom

aggregates (Chaetoceros, Nitzschia, and Odontella aurita (this study)), which is surprising given the variability in these particle types.

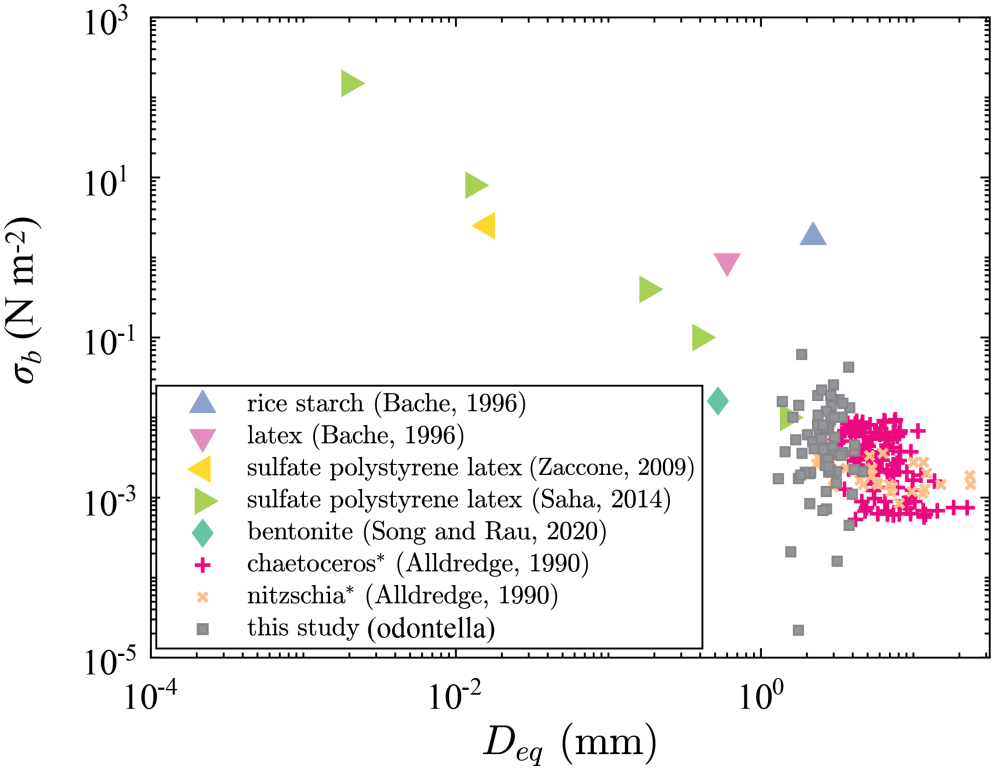

Figure 4-8: Aggregate breakup strength as a function of aggregate size for various types of aggregates from the literature.

4.3 Discussion of the Method

The rotating/oscillating tank and particle tracking methods described in this study allowed for detailed resolution of aggregate fragmentation dynamics that have not yet been shown. The method allows us to uniquely study the response of aggregate morphology to shear exposure in addition to being able to resolve conditions leading to fragmentation. It

further directs us to an important finding that deformation is of great importance to the fragmentation of marine aggregates. Unlike brittle materials, marine aggregates are easily deformed and can restructure in response to external forcing. This restructuring, which took the form of elongation in response to our laminar shear flow, occurred until the aggregate was too fragile to resist further elongation, resulting in fragmentation. As a result we observed elongated morphologies prior to most fragmentation events in both our data of individual fragmentation events and the statistical results obtained. This finding emphasizes how shape and deformation factors must be considered when attempting to model the yield strength of marine aggregates.

Compared to other experimental methods, the rotating/oscillating tank is attractive in that the transition from aggregation to fragmentation mode occurs without need for manual aggregate manipulation, which can cause potential structural changes to the fragile particles. Moreover, previous fragmentation experiments have been limited to shear rates above $O(1)$ s^{-1} (Alldredge *et al.*, 1990; Goldthwait *et al.*, 2004). Our method, in contrast, can locally resolve shear rates down to $O(10^{-5})$ s^{-1}. This capability has allowed us to observe the fragmentation of very fragile aggregates (*e.g.* $\sigma_b < 10^{-4}$ N m^{-2}, Figure 4-8). The strength of these aggregates has largely not yet been quantified in the literature.

The rotating/oscillating tank does have limitations for studying marine snow fragmentation. Within natural aquatic environments, aggregates are rarely if ever made of a single diatom species. Marine aggregates typically involve more than one type of phytoplankton along with other organic detritus and possibly inorganic minerals, all of which can affect aggregate strength. Though we can employ multiple phytoplankton species and additional materials in our tank to better simulate natural marine snow

particles, laboratory studies will never be able to duplicate the complexity of the ocean environment. However, this limitation is present in all laboratory investigations and is not unique to this method. One aspect of the rotating/oscillating tank that varies significantly from fragmentation in the actual marine environment is that it relies on laminar shear rather than turbulent flow, although the shear rates are similar to the more-turbulent regions of the ocean. Average turbulence dissipation rates likely underestimate the hydrodynamic forces that cause fragmentation of aggregates, as strong intermittent events can have a significant effect given that aggregate fragmentation occurs over very short timescales. While laminar shear is excellent for repeatability and for determining local shear rates around each aggregate, the use of laminar flow prevents us from studying fragmentation under the statistical variability of turbulence.

Experimentally, lighting nonuniformities and particle shadows can introduce uncertainty in the particle identification and matching process used with this method, as discussed above. Practically, this limits the particle concentration we can study as too many aggregates will obscure much of the illuminated central tank cross-section. Additionally, discontinuity caused by particle shadows limited the number of frames we could track particles so we could not obtain the entire history of shear and morphology from the very beginning of the tank oscillation. Saha *et al.* (2014) observed that breakage of colloidal aggregates was correlated with their exposure time to hydrodynamic forces. Future improvements that allow longer aggregate tracking could enable us to quantify time-integrated shear exposure.

We also could only resolve two dimensional aggregate shapes from the one-camera imaging system and could, thus, not measure their thickness along the axial direction of

the tank. However, because the fluid shearing was primarily one-dimensional in the azimuthal direction of the tank, which was captured by the imaging system, this method did capture the primary deformation length of the aggregates. Still, aggregates can have asymmetric shapes, so obtaining three-dimensional information of their shape and volume would be desirable for future implementations of this methodology.

The particle tracking with breakup detection would also benefit from further optimization. Our current detection size limit was not sufficient to capture the morphology of the smallest aggregates in our flow. Therefore, the current analysis focused more on morphological variations and fragmentation of large aggregates. Our breakup detection algorithm also likely under-sampled fragmentation due to our conservative implementation. Based on the pseudo color plot in Figure 4-7, the lack of large aggregates in the high-shear regions suggests that even moderately large aggregates readily fragmented when exposed to these shear rates. We developed this algorithm to ensure that all fragmentation events had enough morphology and time information to confidently analyze parent and child aggregates. The requirement that these aggregates be imaged for at least 15 consecutive frames ended up excluding many short-lived fragmentation events. Decreasing this time limit could potentially capture more breakup events in the aggregate population.

4.4 Extension of the Method to Time-Varying Particle Size Statistics

Rather than probe the deformation and breakup behavior of individual aggregates, the transient average response of an entire particle population can also be informative about

the aggregates' ability to withstand hydrodynamic forces. One downside of the methods used in Sections 4.1-4.3 is that it missed some fragmentation events due to the requirements from the particle matching and breakup detection algorithm. In addition, it is advantageous to estimate properties of the entire population, like breakup rates, which are useful in particle dynamics models.

4.4.1 Experimental Procedures

For population measurements, we used the same experimental facility shown in Figure 4-1 with the same imaging methods of background removal and particle identification. We did not apply the particle matching and breakup detection algorithms since we no longer investigated the behaviors of individual aggregates. In order to capture the population changes over an extended time period, we lengthened the experiment time in the rotating/oscillating tank from 175 s to three hours. Due to the limited camera memory and data transfer rates, we also reduced the frame rate to one frame per second. Analysis of the lifespan of aggregates within the camera's field-of-view, also discussed in relation to Figure 4-7, showed that most unique aggregates had a lifespan of less than one second within the illuminated field of view. Therefore, we could assume that the reduced frame rate of 1 Hz was sufficient to avoid double-counting aggregates without employing the aggregate matching algorithm.

Table 4-1: Time series of the entire experiment.

Tank motion	**Aggregation or fragmentation**	**Time series *t* (min)**	**Sampling time *t* (min)**
rotation + oscillation (FM)	both	-360 to -180 (three hours)	-180
rotation only (AM)	aggregation only	-180 to 0 (three hours)	0
rotation + oscillation (FM)	both	0 to 180 (three hours)	1-5, 20, 40, 60, …, 180

For the comparison to Odontella aurita (OA), we added a second algae strain Skeletonema grethae (SG) to this analysis. Table 4-1 shows the operation of the experiments and the sampling time when the camera recorded images. We used dispersed aggregates at the beginning, in which the tank only contained very small aggregates or primary diatom cells. As the fragmentation mode (FM) could also have particles collide and form aggregates, we first performed the rotating and oscillating boundary condition to form aggregates under shear conditions. We recorded 60 particle images after three hours of FM. Next, the tank underwent the aggregation mode (AM) for another three hours. Large aggregates were formed in this step and we took another 60 images. Last we operated the tank with FM for three more hours, using the boundary condition shown in Figure 3-9 (a = 9 cm/s and ω = 0.5 rad/s). Large aggregates would fragment quickly during the transition from AM to FM, so we recorded 300 images for the first five minutes of the FM operation. Due to the camera memory and upload speed, we set up a time interval of 20 minutes, after which the camera captured the particle images for 60 seconds. In summary, one

experimental measurement of aggregation and disaggregation took nine consecutive hours. Figure 4-9 shows the high-speed images of two aggregate types.

It is noted that three hours of rotation and oscillation might not be enough for the particle population to reach a steady state size distribution. In an enclosed system like the present experiment where there was no addition of particles through growth or removal through decomposition or settling, a steady-state size distribution is indicative of a balance between aggregation and disaggregation in the population balance (described in Chapter 1). Therefore, it was necessary to perform two FM operations with different initial aggregate conditions to reconcile the hysteresis error.

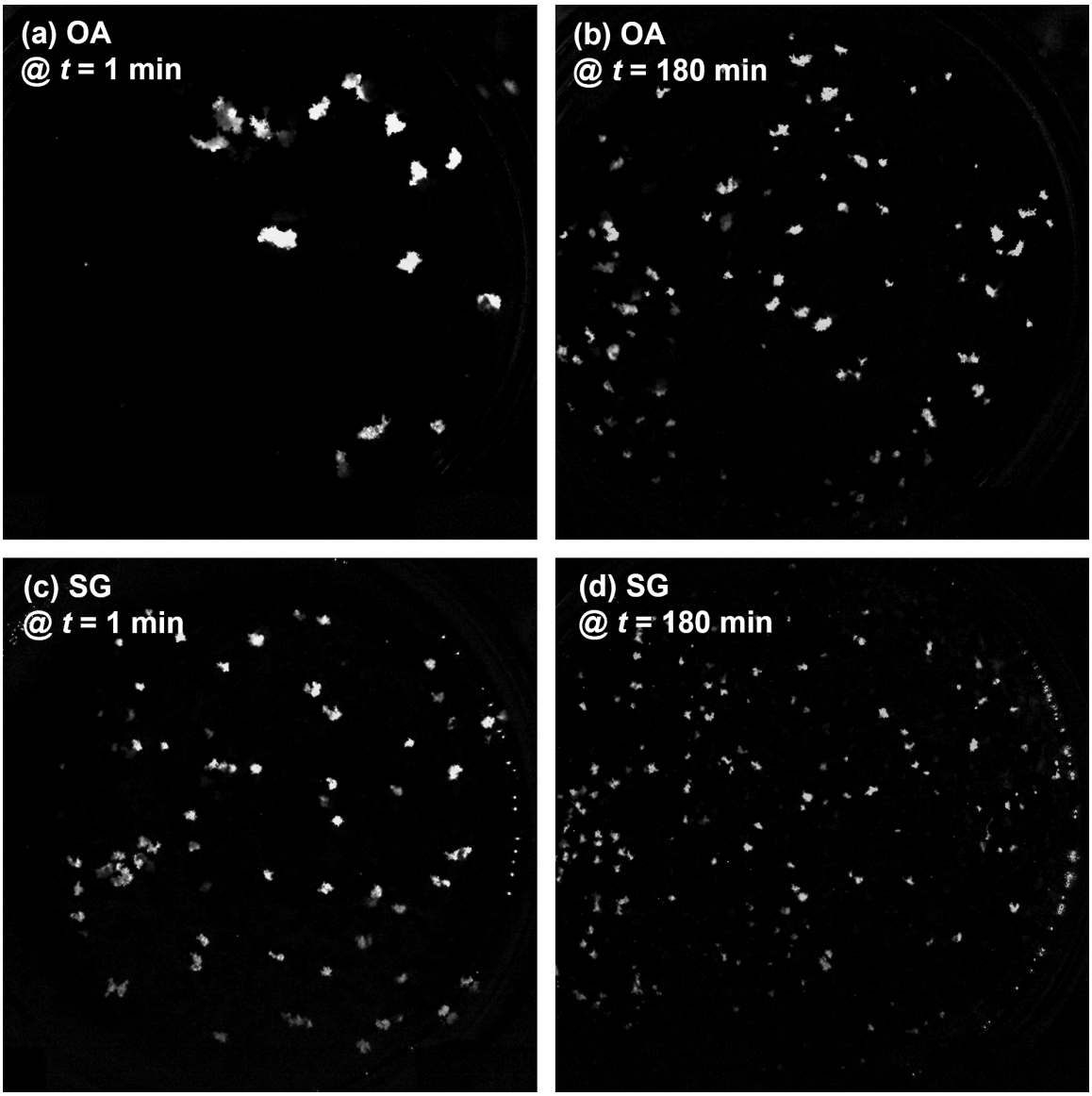

Figure 4-9: High-speed images of (a) OA aggregates after three hours of AM, (b) fragmented OA aggregates after three hours of FM, (c) SG aggregates after three hours of AM, and (d) disrupted SG aggregates after three hours of FM.

We used a hemocytometer to measure the concentration of primary cells before each experiment. Table 4-2 shows the cell counting results. The primary cell of Odontella aurita

(OA) has a larger size of 45 μm × 10 μm, while Skeletonema grethae (SG) has a length of 5 μm and a width of 3 μm on average. To have a similar solid volume of diatoms, the cell concentration of SG was roughly one order of magnitude greater than OA.

Table 4-2: Cell counting results for each experiment.

Diatom aggregate type	**Experiment #**	**Cell concentration (cell/ml)**
Odontella aurita	1	32,000
	2	49,200
	3	41,200
Skeletonema grethae	1	474,000
	2	652,500
	3	367,500

4.4.2 Determination of Fractal Dimensions of Diatom Aggregates

Figure 4-9(a) and (c) are gray images of OA and SG captured after the middle three hours of AM tank operation. Figure 4-9(b) and (d) are images recorded after the last three hours of FM operation. We observed that the two diatom aggregates had different sizes on average. OA aggregates only had a few very large aggregates after three hours of aggregation, but there were smaller and more SG aggregates. After fragmentation, OA was outnumbered by the smaller-sized SG aggregates. The images shown in Figure 4-9 do not

clarify if there are differences in the structure of the aggregate populations, which is typically denoted by the fractal dimension.

Determining fractal dimension of an aggregate population is not trivial. Lee and Kramer (2004) provided a popular, fast, and simple method for characterizing fractal dimensions from two-dimensional projection images. This method has been widely used (Soos *et al.*, 2008; Vajihinejad & Soares, 2018), but it depends on the image processing quality. Their study empirically obtained the relations between the three-dimensional fractal dimension *Df* and the two-dimensional fractal dimensions (D_2 or *Dp*). They ran numerical simulations by creating pseudo aggregates and characterized different fractal dimensions based on the image processing of aggregate morphology. The three-dimensional fractal dimension has the same definition in Chapter 1, and is written as,

$$m_i = m_1 \left(\frac{r_i}{r_1} \right)^{Df}, \tag{4.1}$$

where m_1 and r_1 are the mass and equivalent radius of a primary cell, and the subscript i represents the number of primary cells in one aggregate. D_2 can be determined if we fit a power-law relation of a projection area A_p to the major axis length L_{ma},

$$A_p \propto L_{ma}^{D_2}. \tag{4.2}$$

Similarly, another power law predicts the perimeter-based fractal dimension *Dp* from the perimeter P,

$$A_p \propto P^{2/Dp}. \tag{4.3}$$

Then Lee and Kramer (2004) applied two regression models and obtained the following relationships,

$$Df = 1.391 + 0.01\exp\left(2.164D_2\right), \tag{4.4}$$

and,

$$Df = -1.628Dp + 4.6. \tag{4.5}$$

They later compared the empirical relation with other experimental studies (Serra & Casamitjana, 1998; Tang *et al.*, 2001; Zhang & Buffle, 1996) using the light scattering or electrical sensing method and showed comparable results.

Here we develop an alternative method to estimate fractal dimensions *Df* based on mass conservation in our closed system. We observed that the total projected area of all particles varied over time, despite the fact that the total particulate mass inside the tank did not change. This behavior resulted from the fractal structures of aggregates. The mass conservation inside the tank could be written as,

$$M = \sum N(m_i)m_i = \text{constant}, \tag{4.6}$$

where M is the total mass inside the tank, m_i represents the aggregate mass formed by i primary cells, and N is the number of aggregates with a certain mass. To proceed, we made assumptions that all primary cells share the same size, shape, and mass. The OG or SG aggregates could be represented by one fractal dimension. Additionally, all aggregates with an equivalent radius of r_i have the same mass of m_i. With these assumptions and Equations (4.1) and (4.6), we can write the following,

$$M = \sum N(r_i)m_1\left(\frac{1}{r_1^{Df}}\right)r_i^{Df} = \text{constant}, \tag{4.7}$$

where m_1 and r_1 can be seen as constants. For single diatom species, where m_1 and r_1 are known and constant, Equation (4.7) can be simplified as,

$$\sum N(r_i) r_i^{Df} = \text{constant.} \tag{4.8}$$

During the experiment, we assumed diatom aggregates were thoroughly mixed within the tank after 20 minutes of rotation and oscillation. Thus, the mass of aggregates in the light sheet remained at a constant value and that Equation (4.8) was valid. For each experiment, the particle identification method would first generate the area, major axis length, perimeter, and equivalent diameter (radius) of each aggregate greater than 4 pixels (~400 μm). We determined a detection limit of 4 pixels based on the imaging system and the camera resolution. Figure 4-7(b) showed that aggregates smaller than 4 pixels had negligible volume fraction. Therefore we ignored the total mass of these small, dispersed aggregates in the analysis. We sorted aggregates using the same size ranges used in Figure 4-7(b). We calculated a total aggregate mass by varying the fractal dimension in Equation (4.8). The fractal dimension was determined, when the total mass would have the smallest time variation.

Table 4-3: Fractal dimensions of OA and SG determined by different methods. Methods D_2 and Dp represent the fractal dimensions determined by Equations (4.4) and (4.5).

Method	**High-speed imaging**		**Mass conservation**
	Method D_2 Equation 4.4	Method Dp Equation 4.5	
OA	1.74	2.14	2.19
SG	1.76	2.18	1.70

Table 4-3 compares the fractal dimensions calculated using different methods, where fractal dimensions determined by the method of mass conservation is shown in the last column. The left two columns used the empirical relations developed by Lee and Kramer (2004). We used aggregate images from the high-speed images as the image processing provided major axis length L_{ma}, perimeter P and area A_p. We found that fractal dimensions determined by Equation (4.4) were smaller than those determined by Equation (4.5) in our experiments. One reason was that our image analysis utilized a "dilation and erosion" procedure prior to particle characterization. This procedure tended to remove small curvatures and thus underestimated aggregate perimeters. For the major axis length, both methods fit an ellipse for every aggregate, which was likely another source of uncertainty. Many of them were small aggregates closer to the primary particle size. The methods using D_2 and Dp showed no difference between fractal dimensions of the OA and SG aggregates. In contrast, the method of mass conservation showed that OA aggregates had a higher fractal dimension than SG aggregates. The new method has a main source of uncertainty stemming from the pre-processing step that ignored particles smaller than 4 pixels. It likely caused higher uncertainty for SG due to the smaller aggregate size. We performed these calculations in three separate experiments and found an uncertainty in the fractal dimension of ± 0.16, which indicates that our results were relatively repeatable.

4.4.3 Discussion of Breakup Rates

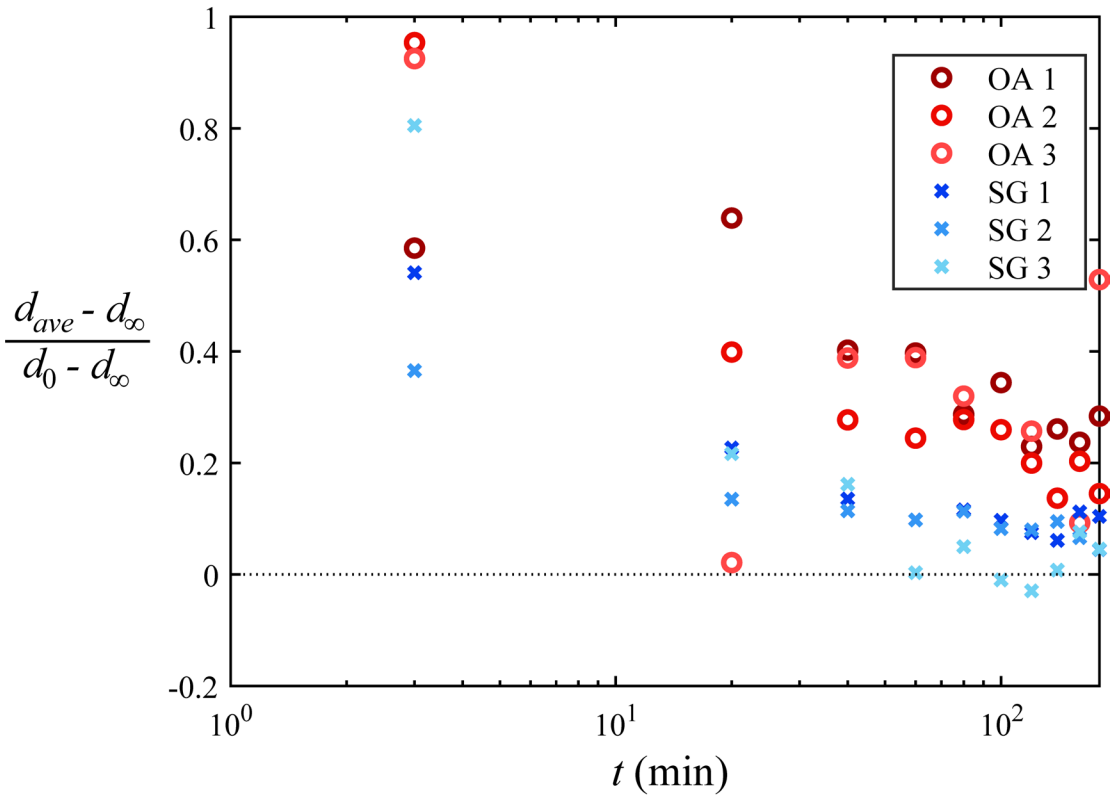

Figure 4-10: Normalized average aggregate size as a function of the tank oscillation time. The initial size (d_0) was the mean aggregate size at t = 0 and the steady-state size (d_∞) was calculated by averaging the mean aggregate size at t = -180 and t = 180. A value of one on the vertical axis represents the particle size after three hours of aggregation, and a value of zero represents the average particle size at steady state.

We can reckon that one aggregate type is more resistant to hydrodynamic forces than a different type if it takes more time than another for the population to reach a steady average size. Figure 4-10 shows the time-series mean average particle size over the last three hours of FM operation in the experiment. As shown in Table 4-1, t = 0 was when the tank started

to oscillate after three hours of AM. We normalized the particle size using the initial size d_0 (i.e. the mean aggregate size at $t = 0$, after 3 hours of AM operation) and the steady-state size d_∞ (*i.e.* the mean aggregate size expected if FM could proceed for an infinite amount of time). We did not achieve a true steady-state condition during this nine-hour experiment. The mean aggregate sizes after FM operation were not the same due to hysteresis, where the aggregate population started at different states of aggregation. Because the aggregate sizes were approaching a steady-state, we estimated the steady-state size d_∞ by averaging the mean aggregate size at t = -180 and 180 minutes, which correspond to the end of the two periods of FM operation. Three hours would be enough for the population of SG aggregates to reach a steady state as the blue symbols at t = 180 min are close to the dashed line in Figure 4-10, showing that the mean size of SG aggregates did not change substantially after three hours of rotation and oscillation. The difference for OA aggregates was larger, showing that the OA aggregates required more time to reach a steady state. Additionally, the normalized particle size trend decayed faster for SG aggregates. Therefore, the SG aggregates were likely weaker than OA aggregates when exposed to the same hydrodynamic environment.

These results could be partially explained by considering the fractal dimension of the two aggregate types. Table 4-3 shows that the fractal dimension of SG aggregates was smaller than OA aggregates during the experiment, meaning that the SG aggregates had a looser internal structure. For similar materials, a looser structure usually leads to a smaller breakup strength as there are fewer internal bonds to hold the aggregate together. Though Figure 4-10 indicates that SG broke apart more rapidly than OA, we need further investigations to extract the breakup kernel required for a population balance model.

4.5 Summary

We have described a novel rotating/oscillating tank for aggregation and disaggregation studies. The oscillatory shear flow has shown great potential to mimic the unsteady conditions in the ocean environment to study the detailed dynamics of aggregates and other suspended materials. The magnitude of shear that the tank produces can be made comparable to that of different ocean environments by adjusting the rotating and oscillating boundary conditions. Potentially, this novel tank could be used for studying particles in very different environments, including everything from coastal sediment particles experiencing oscillatory waves above the seabed to slowly settling organic aggregates in the open ocean.

Overall, the image processing and particle matching algorithm allowed us to track individual particles as a function of time and our breakup detection method was simple and efficient. However, the required processing time was limited by the need to manually verify each breakup event. We recommend minor improvements to the experimental facility that will improve the functionality of these algorithms. Specifically, reducing the tank length to avoid the visual obscuration caused by particles in the front of the tank will increase the tracking length and improve breakup detection, so long as the shorter length does not invalidate the two-dimensional flow assumption along the central plane. This modification will also allow the imaging system to track a greater percentage of the particles in the tank at one time and, in conjunction with refining our breakup detection thresholds, will facilitate the capture of a greater number of breakup events in a given aggregate population.

We also plan to employ a new high-speed imaging system with greater imaging magnification, which will decrease the aggregate size detection limit. It should be noted that the presented method can be used to capture long-term population changes as well as the short-duration fragmentation events presented above. Though the memory capacity of the imaging system determines the overall data collection length, lower-speed imaging systems with continuous recording or the acquisition of population snapshots in time can be used to measure the evolution of population size spectra for much longer than the 175 s recordings acquired in these experiments.

In the future, we will continue exploring more biophysics with this novel method. In particular, we hope to investigate the role of shear history in the breakup of aggregates in addition to the influence of aggregate makeup and structure on overall aggregate strength. In addition to allowing us to study fragmentation, this method also provides a means to acquire large datasets of aggregate deformation in response to shear. The strain characteristics of these aggregates could potentially be used to extract additional mechanical properties of the aggregates and their cohesive component particles.

Chapter 5

Fragmentation Strength Characterization of Marine Diatom Aggregates and Colloidal Flocs in Oscillatory Shear Flow

In this chapter, we implement fragmentation experiments over four types of aggregates: two diatom species, Odontella aurita and Skeletonema grethae, and two plastic microspheres, sulfate polystyrene and polyethylene. The bonding theory of microplastic polymers is well established, so we compare their breakup behaviors and strength by exposing algae aggregates and polymer flocs to similar hydrodynamic conditions. This chapter enhances our understanding of the biological bonding strength and fractal structures of the phytoplankton aggregates. The first two sections of this chapter will be soon submitted to a journal publication.

This chapter is organized into four subsequent sections. Section 5.1 describes the upgraded experimental facility, the imaging method, and preparation of various aggregates. This section also provides a calculation of bonding forces between plastic microspheres based on the XDLVO theory and a force balance model of adhesion interactions at breakup. Section 5.2 presents the results of deformation and fragmentation of four aggregate types. Additionally, it discusses fractal structures and viscoelastic behaviors of formed aggregates. Section 5.3 summarizes results and findings from my laboratory fragmentation experiments and addresses suggestions for future laboratory and field experiments.

5.1 Materials and Methods

5.1.1 Experimental Facility

The aggregate fragmentation experiments were performed in the rotating and oscillating roller tank developed by the authors (Song & Rau, 2022), which was slightly modified here, as shown in Figure 5-1. The facility consisted of a double-sided cylindrical roller tank made of acrylic with each side having an inner diameter of 100 mm, a wall thickness of 5 mm, and a length of 100 mm. Only one half of the roller tank was used for the experiments presented. We decreased the length of the tank from 300 mm, as used in (Song & Rau, 2022) to 100 mm to reduce the visual obscuration caused by overlapping particle images, which increased our ability to continuously track aggregate and identify breakup events. We determined that the secondary flow generated by the end of the tank would not influence the flow motion along the light slit aperture based on the characteristic boundary layer thickness of a laminar flow over a rotating disk (von Kármán, 1921). A customized timing pulley installed at the outside wall was located 70 mm from the end of the tank (Figure 5-1(b)). A timing belt connected the tank to another timing pulley attached to the motor with an adjustable gear ratio that could range from 0.21 to 0.76. We controlled the tank motion following the same procedure explained previously (Song & Rau, 2022). An LED light panel (StudioPRO S-1200D, Fovitec) illuminated the suspended particles by shining through the side of the tank through a 10 mm slit aperture, located 30 mm from the visualization-end of the tank (Figure 5-1(a)). A high-speed camera (FASTCAM Mini AX200, Photron) with a 105 mm macro lens of (Sigma 105mm f/2.8 EX DG) captured the aggregate motion.

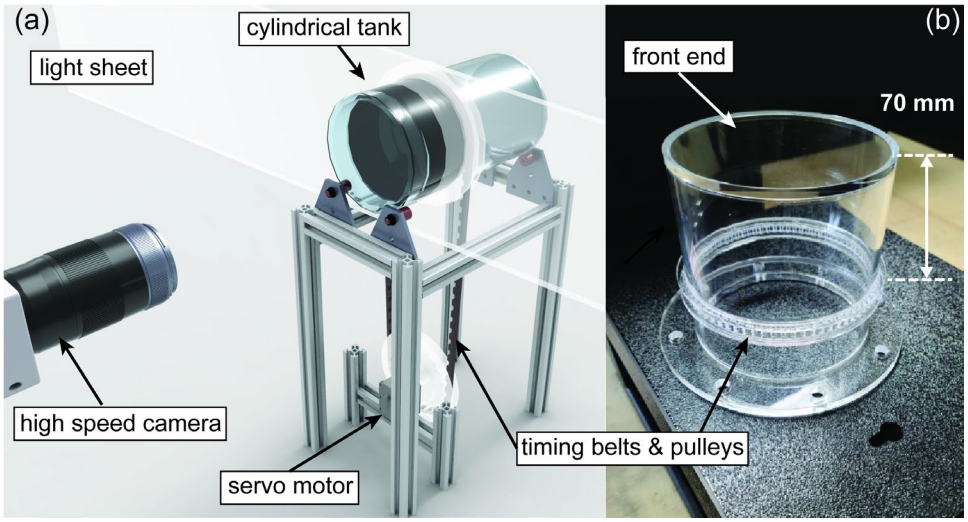

Figure 5-1: (a) schematic diagram of the experimental facility, and (b) a picture of the one-half of the two-sided roller tank.

We performed aggregation and fragmentation experiments following protocols developed by the authors (Song & Rau, 2022). Briefly, when in Aggregation Mode (AM), the roller tank rotated with a constant rotation rate, b. Once aggregates were formed, we superimposed a sinusoidal oscillation to the constant rotation to operate in Fragmentation Mode (FM). The new boundary condition at the tank wall in FM was $u_R(t) = a \cdot \sin(\omega t) + b$, where a was the oscillation amplitude, ω the angular frequency, and t time. This condition created an oscillating boundary layer on the tank wall with shear rates of 10^2 s^{-1} or lower, which were determined through an analytical solution of the laminar fluid motion (Song & Rau, 2020a).

5.1.2 Imaging Methods

The camera focused on aggregates illuminated by the LED light panel. We utilized a 3D-printed circular calibration plate to measure the imaging magnification ratio at the mid-plane of the 10 mm slit aperture. Experiments with Odontella aurita (OA) had a 10.34 px/mm ± 0.06 px/mm magnification, while experiments with the other three aggregate types (SG, PS, and PE) had a magnification ratio of 10.93 px/mm ± 0.07 px/mm.

Each experiment recorded 21,841 image frames, acquired at a rate of 125 fps (frames per second) for OA, SG, and PE. Due to the fast deformation of PS aggregates, we used higher image frame rates of 250, 500, and 1000 fps during various experiments to capture their deformation behavior. The shutter speed was 1/1000 s for all aggregate types. We utilized the same method of background removal, particle identification, particle matching, and breakup detection described in detail by Song and Rau (2022) with a particle detection threshold of 4 pixels. We only analyzed aggregates that could be continuously tracked for at least 0.12 s for fragmenting aggregates and 1 s for non-fragmenting aggregates. The time history provided by these time limits were to ensure confidence in the detection, or lack thereof, of a breakup event (Song & Rau, 2022).

Song and Rau (2022) found that OA aggregates regularly elongated prior to breakup. To characterize this deformation further, we developed one additional image processing feature to detect the weakest point of a deformed aggregate. We considered two scenarios, either that an aggregate in projection had a “dumbbell” shape, indicating necking between two larger ends, or that the aggregate was shaped like an ellipse. We assumed the weakest point of the aggregate was located at the thinnest point of the neck. For the ellipse-shaped aggregates, we instead took the minimum Feret diameter to represent the most fragile

connection. These measurements are discussed further below. To identify the neck thickness, we analyzed binarized images of each aggregate and found their minimum thickness in the direction perpendicular to their major axes. It should be noted that one deformed aggregate could have more than one neck. In such cases, we used the smallest neck, where the neck size resolution was one pixel.

5.1.3 Preparation of Aggregates

We used the same roller tank to form and fragment aggregates. Table 1 summarizes the types of aggregates with their sizes, cell counts, and salt solutions. Table 1 also lists the time required for aggregation and the tank rotation parameters used for aggregation and fragmentation. We varied the constant rotation speed, b, to accommodate the different excess densities of the various types of particles, with higher densities requiring faster rotation rates to minimize wall impacts. The oscillation magnitude for fragmentation experiments using OA, SG, and PE created a maximum laminar shear rate of 10^2 s^{-1} that is similar to the surface ocean. The inner regions of the tank provided fluid shear more typical to the mixed layer (Song & Rau, 2022). We used a smaller oscillation magnitude for the more fragile PS flocs, for which the flow had a maximum shear rate of only 16.5 s^{-1}.

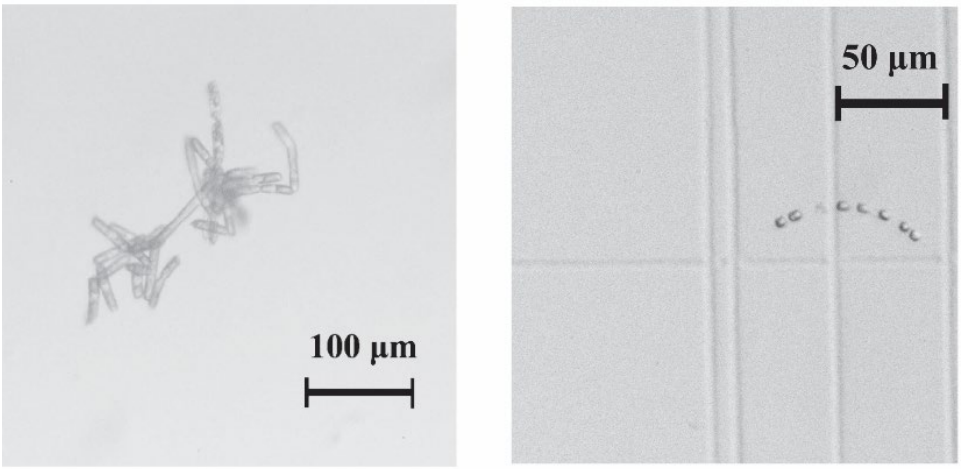

Figure 5-2: Microscopic images of Odontella aurita (left) and Skeletonema grethae (right).

Figure 5-2 shows micrographs of cultured Odontella aurita v minima (UTEX LB 3038) and Skeletonema grethae (CCMP 775), which were cultured using f/2 medium for nutrients and laboratory-made artificial seawater (Kester *et al.*, 1967) with a salinity of 30 ppt. We prepared the artificial seawater from deionized water by passing it through 5, 1, and 0.2 µm filters followed by an ultraviolet water purifier (HQUA-OWS-12). We used a light intensity of 30 µmol/m^2s^1 on a 12:12 hour light/dark cycle and cultured all samples at a room temperature of 20.9 ºC (+2.3 / -4.4 ºC). We maintained their growth phase by splitting the mediums into Erlenmeyer flasks at a regular rate. Odontella aurita cells have an average length of 45 µm and a width of 10 µm. Skeletonema grethae cells are smaller and have a size of only 3 µm × 5 µm on average. We used a hemocytometer to estimate cell concentrations and maintained similar solid volume concentrations between experiments. We created the aggregation of algae aggregates by rolling them in artificial seawater AM for three hours.

To provide comparable aggregates that had quantifiable interparticle forces, we used two types of colloidal microplastic particles destabilized in salt solutions to promote aggregation. We prepared polystyrene (PS) aggregates from surfactant-free monodisperse white sulfate latex beads (Interfacial Dynamics Corp., Catalog No. S37223, 8% weight by volume). The mean diameter was 3 μm. First, we diluted 1 mL of latex solution into 50 mL of deionized water. Then we transferred them into the disaggregation tank and fully destabilized them by adding calcium chloride at a concentration of 0.5 M. The resultant solution viscosity increased to 0.0111 cm^2/s (Abdulagatov & Azizov, 2006; Wahab & Mahiuddin, 2001). The resulting concentration of PS microspheres in the disaggregation tank was 6.7×10^6 cells/mL. Two days of rolling in AM formed PS flocs with sizes of up to two millimeters. The experiment required this long aggregation time due to the small excess density of PS (1055 kg/m^3) compared to the salt solution (1038 kg/m^3) (Wahab & Mahiuddin, 2001), combined with the small size of the PS microspheres.

We used dry powder of white polyethylene (PE) microspheres (Cospheric, WPMS-1.45) to form a second type of polymer flocs. The diameters ranged from 53 μm to 63 μm and their density was 1450 kg/m^3. Without surfactants, the hydrophobic polyethylene was difficult to disperse in water solutions despite its large excess density. To obtain suspended flocs, we used a magnetic stirrer to blend 1 g of PE powder in deionized water. Six hours of mixing dispersed most of the PE particles. Still, a small but non-negligible number of PE particles stayed on the water surface and could not be used in fragmentation experiments, which is why the particle concentration in Table 1 is listed as less than 8,500 cells/mL. We used high concentrations of NaCl to minimize the electrostatic repulsive

forces to permit aggregation. The tank also operated with a high rate of constant rotation to account for the large particle density and avoid wall contact.

Table 5-1: Sizes, cell concentrations, and experimental conditions of four types of aggregates. Breakup conditions are parameters used for controlling the servo motor and have a resolution of 0.229 rpm.

Types of aggregates	**Size (μm)**	**Cell conc. (cells/ml)**	**Saltwater**	**Agg. time**	**Tank rotation parameters**		
					b	*a*	*ω*
Odontella aurita (UTEX LB 3038)	45 × 10*	~46,000	filtered artificial seawater (30 ppt)	3 hrs	25	125.1 150.8	0.5
Skeletonema grethae (CCMP 775)	3 × 5*	~450,000	filtered artificial seawater (30 ppt)	3 hrs	15	125.1	0.5
Sulfate polystyrene	3	6.7×10^6	0.5 M $CaCl_2$	2 d	5.4	21.6	0.5
Polyethylene	53-63	< 8,500	0.5 M NaCl; 1.0 M NaCl	3 hrs	50	125.1	0.5

*The size for diatom cells is major × minor axis length.

5.1.4 Extended Derjaguin–Landau–Verwey–Overbeek (XDLVO) Theory

We applied the XDLVO theory to estimate the interparticle forces holding the plastic aggregates together. The extended Derjaguin-Landau-Verwey-Overbeek (XDLVO) theory quantitively describes the influence of van der Waals forces F^{LW}, electrostatic forces F^{EL}, and Lewis acid-base forces F^{AB} on the interaction among plastic microspheres (van Oss,

2008). XDLVO interaction forces decay with a separation distance l in the configuration of two spheres of equal radius R_s. The expression used to calculate the van der Waals force F^{LW} (van Oss, 2008) is given as

$$F^{LW} = \frac{A_{131} R_s}{12(l - l_0)^2}, \tag{5.1}$$

where A_{131} is the Hamaker constant for two surfaces of the same materials, denoted by 1 (in this case either PE or PS) interacting through a different medium, denoted by 3 (in this case water), and l_0 = 0.157 nm is the minimum equilibrium distance. We used Hamaker constants of plastics A_{11} and water A_{33} to calculate A_{131} using the expression $A_{131} = \left(\sqrt{A_{11}} - \sqrt{A_{33}}\right)^2$ (van Oss, 2006). In our study, we employed A_{33} = 3.7 × 10^{-20} J (Freitas, 1999), A_{11} = 7.6 × 10^{-20} J for PE (Freitas, 1999; Shams *et al.*, 2020), and A_{11} = 6.5 × 10^{-20} J for PS (Israelachvili, 2011). We determined A_{131} as 6.9 × 10^{-21} J for PE dispersions and 3.9 × 10^{-21} J for PS.

The expression for the electrostatic force F^{EL} as a function of the separation distance l is,

$$F^{EL} = -2\pi\varepsilon_1\varepsilon_0 R_s \varphi_0^2 \ln\left[1 + \exp\left(\kappa\left(l_0 - l\right)\right)\right], \tag{5.2}$$

where ε and ε_0 are the dielectric constant of water and the permittivity of free space, estimated to be 80 (at 20 °C) and 8.854 × 10^{-12} C/Vm (Elimelech *et al.*, 1995), respectively. We can write the colloid surface potential φ_0 into the following form,

$$\varphi_0 = \zeta\left(1 + \frac{z}{R_s}\right)\exp\left(\kappa z\right), \tag{5.3}$$

where z is the distance between the particle surface and the slipping plane, which ranges from 0.3 to 0.5 nm, and ζ is the zeta potential. The symbol κ in Equations (5.2) and (5.3) is the inverse Debye length subjected to the aqueous solutions. We write the expression as (Israelachvili, 2011),

$$\frac{1}{\kappa} = \sqrt{\frac{\varepsilon kT}{4\pi e^2 \sum v_i^2 n_i}}, \tag{5.4}$$

where k is the Boltzmann's constant, T represents absolute temperature, e is the electronic charge, v_i is the valency of each ionic species, and n_i is the number of ions of each ion specie.

The classic DLVO theory did not consider hydrophobic attractions or hydrophilic repulsions (van Oss, 2008). Van Oss proposed a remedy to consider the polar interaction energies using the Lewis acid-base approach. It is a short-range force, and the working range usually is smaller than 8 nm (Brant, 2002; van Oss, 2008). We used the exponential decay model proposed by van Oss (2008),

$$F^{AB} = -\pi R_s \Delta G^{AB} \exp\left[\left(l_0 - l\right)/\lambda\right], \tag{5.5}$$

where ΔG^{AB} is the free polar potential energy for a geometric configuration of two parallel flat plates. The symbol λ is the decay length, where we chose λ = 0.6 nm for water (van Oss, 2006). We used ΔG^{AB} = -102 mJ/m^2 for PE particles without surfactants (van Oss, 2008). The PS microspheres had sulfate modifications on their surface to become stabilized in water solutions, so we performed a detailed calculation of ΔG^{AB} based on contact angle measurements for PS, the details of which are included in Appendix E. We found that the polar energy for sulfate PS was notably weaker than PE, in which the Lewis acid-base free energy for PS was -16.6 mJ/m^2 (-102 mJ/m^2 for PE). This value was consistent with our

observations in the experiment, as PS particles formed a more stable suspension in deionized water, while PE particles showed strong hydrophobicity.

5.1.5 Necking Stress Model of Deformed Aggregates

Analysis of fragmentation required investigation of the forces that act on an aggregate in the laminar oscillatory flow of the facility. To develop a hydrodynamic force model, we assumed only a one-way coupling from the fluid to the aggregate (Raju & Meiburg, 1997). In other words, we assumed that the fluid flow was negligibly influenced by the aggregates. To show that an aggregate's center of mass followed the fluid motion, we calculated a characteristic Stokes number *St* for our aggregates,

$$ST = \frac{\left(\rho_p - \rho_f\right) d_c^{\,2} U}{18 \mu L}, \tag{5.6}$$

where the excess density ρ_p-ρ_f represented the density difference between the aggregates and solution, where μ was the fluid viscosity. It was challenging to measure the density of the diatom aggregates without knowing their porosity, so we estimated the excess density of diatom aggregates to be smaller than 3.25×10^{-3} g/cm^3 following the measurements conducted by Zetsche *et al.* (2020), who calculated the apparent excess density using the Stokes drag equation. We used the magnitude of tank oscillation (a) as the characteristic velocity scale U, and the characteristic boundary layer thickness $(\nu/\omega)^{1/2}$ (Song & Rau, 2020a) as the length scale L, where ν was the kinematic viscosity of tank fluid. We estimated the mean size of the tracked aggregates from our experimental images to be on the order of 1 mm. With the parameters listed above, the Stokes numbers for all

experiments was smaller than one, confirming that the analyzed aggregates approximately tracked the fluid motion in the tank. Thus we could assume the velocity of a non-fragmenting particle using the fluid velocity calculated at its center of mass.

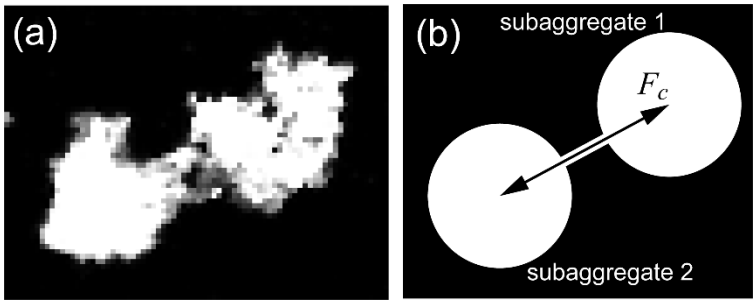

Figure 5-3: (a) grayscale image of a deformed aggregate, and (b) schematic model of a "dumbbell" aggregate, where the coupling force F_c represents the inter-subaggregate force.

Next, we assumed that the deformed aggregates prone to fragmentation had a "dumbbell" shape with a thin neck between two larger clumps. Figure 5-3(a) shows one example grayscale image of a deformed SG aggregate, while Song and Rau (2022) observed this regular deformation prior to fragmentation of OA aggregates. For analysis, we assumed that breakup occurred when the tensile stress acting on the neck due to fluid forces exceeded a critical strength value shown as F_c in Figure 5-3(b). To estimate fluid forces acting on the aggregate, we performed a Maxey-Riley force analysis (Maxey & Riley, 1983) on the two separate subaggregates of the "dumbbell". The Maxey-Riley equation is a second order force balance equation that applies the Newton's second law to describe the motion of an inertia particle in the fluid flow. The equations governing particle motions at a critical breakup condition are,

$$\rho_p V_1 \frac{\partial u_{p,1}}{\partial t} = \rho_p V_1 \frac{\partial u_p}{\partial t} =$$
$$3\pi\mu d_1 (u_{f,1} - u_p) + V_1 \left(\rho_p - \rho_f\right)\vec{g} + \rho_f V_1 \frac{\partial u_{f,1}}{\partial t} + \frac{1}{2}\rho_f V_1 \left(\frac{\partial u_{f,1}}{\partial t} - \frac{\partial u_p}{\partial t}\right) + F_B - F_c$$
$$\rho_p V_2 \frac{\partial u_{p,2}}{\partial t} = \rho_p V_2 \frac{\partial u_p}{\partial t} = \tag{5.7}$$
$$3\pi\mu d_2 (u_{f,2} - u_p) + V_1 \left(\rho_p - \rho_f\right)\vec{g} + \rho_f V_2 \frac{\partial u_{f,2}}{\partial t} + \frac{1}{2}\rho_f V_2 \left(\frac{\partial u_{f,2}}{\partial t} - \frac{\partial u_p}{\partial t}\right) + F_B + F_c$$

where subscripts 1 and 2 represent the two subaggregates in one "dumbbell", V, d, and u_f are volume, diameter, and corresponding fluid velocity of each, and u_p is aggregate velocity at its center of mass. The F_B term represents the Basset force (Crowe *et al.*, 2011), which accounts for the forcing history of the particle, and F_c is the coupling force that holds two subaggregates together. For a critical breakup condition, we assumed that there was no relative displacement of subaggregates to the parent aggregate, so the particle velocities of subaggregates $u_{p,1}$ and $u_{p,1}$ are the same as the parent aggregate u_p. The right-hand side of the equations represents the forces acting on the aggregate. The first term is the Stokes drag, where we approximated each subaggregate as an equivalent sphere to determine its fluid drag. We then neglected the second term, the buoyancy force, due to the small excess density of the aggregates. The next two terms represent a pressure gradient force that accounts for the acceleration of aggregates and the displaced fluid. The Basset force term describes unsteady effects and was neglected because we assumed no temporal delay in the development of the boundary layer around the aggregates (Parker *et al.*, 1972; Raju & Meiburg, 1997). Therefore, we can simplify Equation (5.7) and solve for the coupling force F_c at the instant of breakup as,

$$F_c = \frac{d_1^3 d_2^3}{d_1^3 + d_2^3} \cdot \left[3\pi\mu \left(\frac{u_{f,1} - u_p}{d_1^2} - \frac{u_{f,2} - u_p}{d_2^2} \right) + \frac{\pi}{4} \rho_f \left(\frac{\partial u_{f,1}}{\partial t} - \frac{\partial u_{f,2}}{\partial t} \right) \right]. \quad (5.8)$$

Based on the above equation, the forces that drive the particle motion and lead to fragmentation are the viscous Stokes drag and the pressure gradient effects.

To estimate the coupling stress within non-fragmenting aggregates for comparison, we made further simplifications to Equation (5.8). These non-fragmenting aggregates either only deformed slightly into a dumbbell shape with a thick neck or remained ellipsoidal. We assumed that these aggregates were made up of two equal-sized subaggregates held together with a larger contact area, and that the velocity difference could be calculated from the local instantaneous shear rate G, the aggregate size d, and the orientation angle ϕ between the particle's major axis and the streamwise direction of fluid motion. These assumptions simplified the coupling force for an ellipsoidal aggregate in Equation (5.8) can be written as

$$F_c = \frac{3\pi}{2} \mu G d^2 \sin\phi + \frac{\pi}{8} \rho_f d^4 \frac{\partial G}{\partial t} \sin\phi, \quad (5.9)$$

We obtained the shear rate G using the analytical description of the laminar flow and the orientation angle ϕ using the image analysis methods developed by Song and Rau (2022).

5.2 Results of Deformation and Breakup

5.2.1 Shear Rates of Aggregated Diatom and Plastic Microspheres at Breakup

We performed breakup experiments for OA, SG, PS, and PE and observed fragmentation of OA, SG, and PS aggregates. PE aggregates did not break at the shear rates produced in

our disaggregation tank. The automated particle tracking algorithm identified and tracked 180,682 (OA), 114,549 (SG), 94,571 (PS), and 31,980 (PE) aggregates. OA, SG, and PE aggregates ranged from several hundred microns to up to five millimeters, while the largest size of PS flocs was approximately two millimeters in equivalent circular diameter. Our breakup detection algorithm obtained 79, 75, and 51 breakup events for OA, SG, and PS, which we manually confirmed in the images prior to analysis. It should be noted that the breakup events were conservatively identified. During experimentation, we visually observed more breakup events than are reported. These events were ultimately rejected due to inappropriate lighting or insufficient lifespan in the image timeseries. It should be emphasized that many breakup events using PS were also not counted due to the small particle size and our detection size limit of 4 pixels (~ 200 μm in diameter).

Figure 5-4 summarizes breakup results with various aggregated materials reported in this study and from the literature (Alldredge *et al.*, 1990; Bache *et al.*, 1997; Saha *et al*., 2014; Song & Rau, 2020b; Zaccone *et al.*, 2009). Equivalent dissipation rates, $\hat{\varepsilon}$ calculated from $\hat{\varepsilon} = G^2\nu$, are also plotted. The disrupted algae aggregates from this study had equivalent diameters ranging from 1 mm to 5 mm, while the smallest fragmented PS aggregate detected had a diameter of 300 μm. The shear rates at breakup in this study showed a wide range, reaching as high as 10 s^{-1}, similar to values observed in a surf zone (George *et al*., 1994), though breakup was also observed at shear values below 10^{-1} s^{-1} for both algae and PS aggregates, equivalent to shear caused by a turbulence dissipation rate of less than 10^{-8} W/kg. This value is representative of the median dissipation rate at ~20-30 m depths in the open ocean but has also been observed in short bursts at depths of 200

m (Franks *et al.*, 2022). Given that our observed breakup events typically occurred from less than one second of shearing, even these short bursts may be important to the disaggregation of sinking marine snow.

Comparing all of the breakup results in Figure 5-4 across material types and aggregate sizes, the shear rate at breakup seemed to follow a logarithmic decay as aggregate size increased. Sonntag and Russel (1986) and Higashitani *et al.* (2001) described a decline of breakup strength that followed a power law for microplastic flocs and simulated aggregated spheres, meaning that generally the disruption of smaller flocs required stronger fluid stress. In our study, both the OA and SG algae aggregates broke at similar sizes and shear rates despite having distinct primary cell sizes. PS aggregates broke at similar shear rates but also at smaller sizes, which indicated that their interparticle bonding was weaker than that of the OA and SG aggregates.

We did not observe fragmentation of PE aggregates even though they were similar in size to the OA, SG, and PS aggregates, which means that the bonding stress of PE used in this experiment was stronger than the other aggregate types. In Appendix F, we applied the XDLVO theory to calculate the primary bonding force within PE and PS flocs. As high salt concentrations screened electrostatic repulsions, primary attractive forces were equal to the sum of van der Waals forces and Lewis acid-base forces. The attractive force for PE flocs was estimated to be two orders of magnitude stronger than PS flocs, assuming similar interparticle separation distances. This result was due to stronger hydrophobicity and a larger primary particle size of the PE particles. Assuming that the interparticle separation distances between the aggregates are ~10 nm for both the PE and PS (Gregory, 1981; Israelachvili & Tabor, 1972; Li *et al.*, 2011; Tabor & Winterton, 1969), we estimate the

interparticle force to be approximately 5×10^{-12} N for PS and 2×10^{-10} N for PE (see Figure F-1). Given that PE and PS aggregates appear to be both stronger and weaker, respectively, than the algae aggregates shown in Figure 5-4, we expect that the interparticle bonding forces including the biological sticky content (TEP) holding the OA and SG aggregates together lie in between these two values.

Shear rates at breakup can represent characteristic flow conditions, but it should be emphasized that breakup strength also depends on the size and morphology of aggregates (Burd & Jackson, 2009), especially the elongation and necking behavior. The large range of shear at breakup in our results, shown in Figure 5-4, was likely due to variations in aggregate morphology. Another reason that could have caused the variability was that fluid stress likely exceeded the critical strength of aggregates in some cases. Additionally, biological factors such as varying production of transparent exopolymer (Azetsu-Scott & Passow, 2004) could have affected the overall cohesiveness of the diatoms.

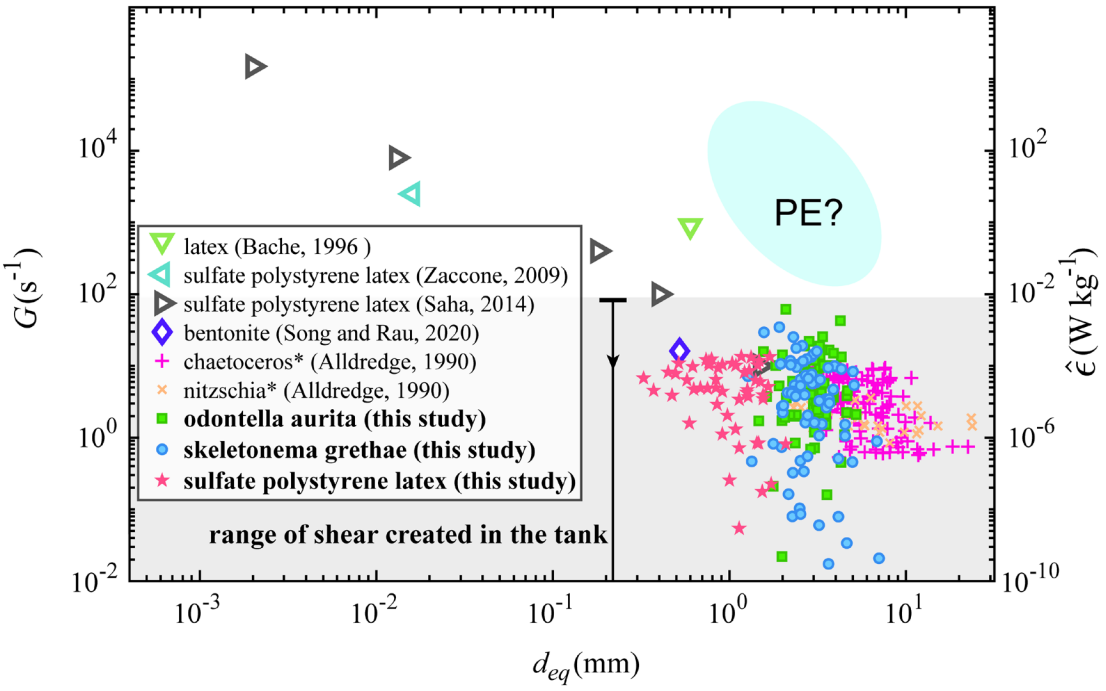

Figure 5-4: Shear rates at breakup as a function of aggregate size for various material types from other literature and this study (the current experimental shear range plotted as the shaded area). Equivalent dissipation rates are also plotted. Fragmentation of PE flocs was not observed during the experiment, so shear rates for PE are estimated based on the size range detected in the experiment. Shear rates in studies marked with * are calculated from turbulence dissipation rates.

5.2.2 Morphology and Fragmentation Behaviors

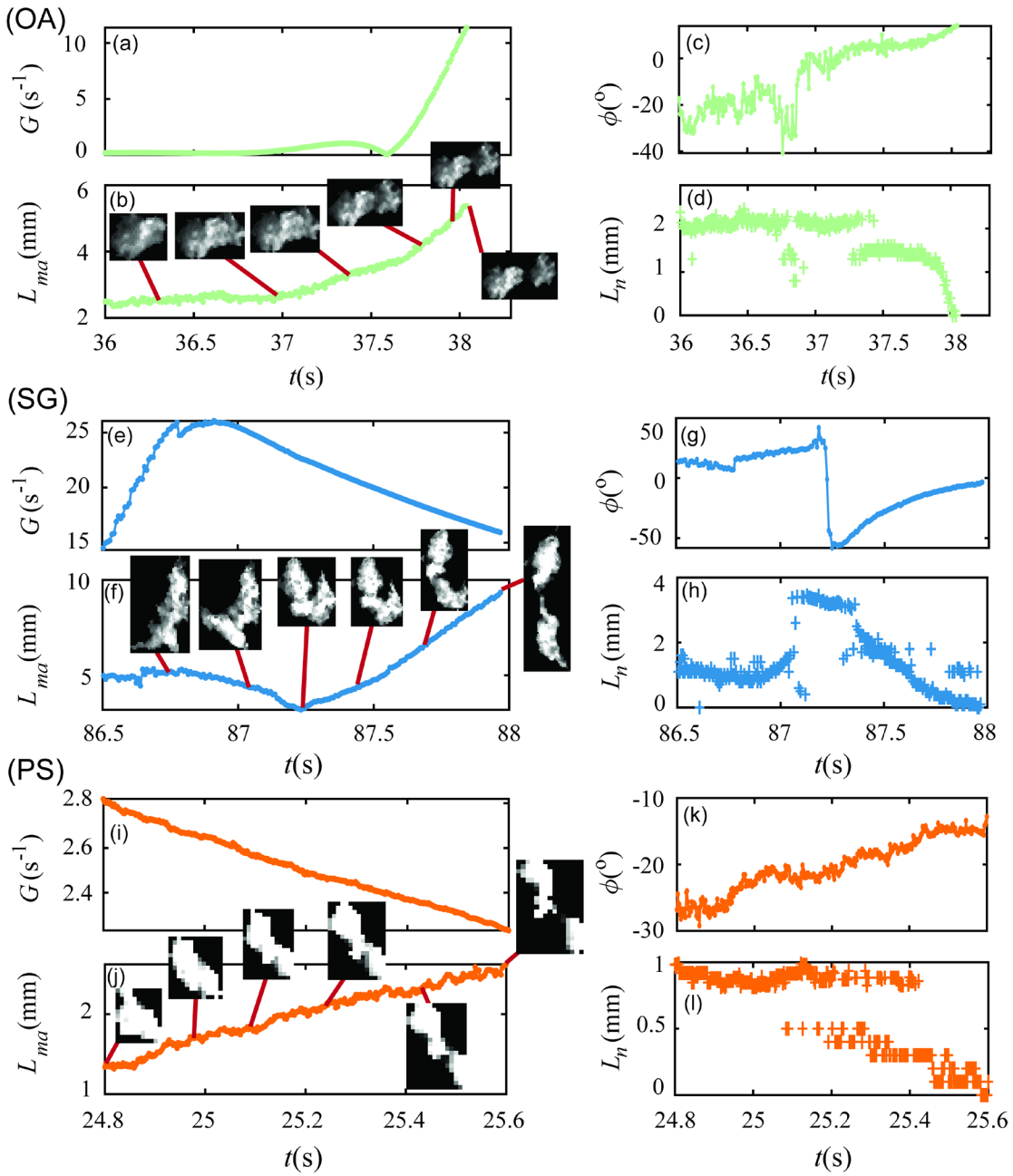

Figure 5-5: Lagrangian time series of OA, SG, and PS aggregates. The time-resolved shear exposure, changes in major axis length, orientation angle, and neck size are shown respectively.

Figure 5-5 illustrates the importance of the time-varying deformation of the aggregates prior to breakup. The figure shows three example breakup events of OA, SG, and PS aggregates with their sub-images obtained from particle tracking. We plot their shear exposure and morphological evolutions, including major axis length L_{ma}, orientation angle ϕ, and neck size L_n. The time is listed for reference, with t = 0 s equal to the first image after the tank started to oscillate. The fragmented OA aggregate (Figure 5-5(a)-(d)) initially had a major axis length of 2.24 mm. This aggregate began to elongate due to shear exposure at t = 37.02 s, and we observed a notable necking behavior starting at t = 37.28 s. The major axis length increased, and the neck became thinner with the increase in shear rates (Figure 5-5(d)). At t = 38.04 s, this aggregate broke into two separate parts. The SG aggregate shown in Figure 5-5(e)-(h) underwent a re-orientation prior to breakup. Two connected parts started to fold as the major axis length decreased from 5.32 mm to 3.27 mm. We also observed a drastic change in its orientation angle, which was followed by stretching. Multiple necks occurred during the elongation, but only one developed into the fracture at t = 87.97 s. The PS aggregate experienced a decaying shear exposure before its breakup. At t = 25.08 s, a neck emerged, which thinned until fragmentation occurred at t = 25.61 s.

In total, we observed 205 breakup events, which allow us to provide a summary of some of their common characteristics. First, a monotonic increase in fluid shear was not necessary for fragmentation. Second, we found that all fragmentation events underwent substantial elongation in their major axis length, with over 95% of them accompanied by necking that continued until breakup. This characteristic deformation led to the assumption of our ‘dumbbell’ shape model for the force analysis described below. Moreover, the torque from the hydrodynamic forces tended to align the aggregates’ major axes with the

streamlines of the flow. This can be seen in Figure 5-5(c), (g), (k) as the orientation angle of the aggregates reduced in magnitude as they elongated prior to breakup.

In addition to disrupted aggregates, we also sampled unbroken aggregates and compared their morphology under shear. We randomly selected 3,879 OA aggregates, 3,870 SG aggregates, and 2,300 PS aggregates that were tracked continuously for more than one second and did not break. We did not sample PE aggregates because we could not confirm if they reached a critical condition in which a deformed aggregate was near breakup. For each sampled aggregate, we measured a ratio of the aggregate's neck size L_n to its minimum Feret diameter d_{Fmin}, defined as $\beta = L_n / d_{Fmin}$. The minimum Feret diameter describes the smallest breadth along a specified direction in the particle's projection (Merkus, 2009), but it fails to capture thin regions of concave shapes. A floc always has a β ratio of unity if it has a convex shape, as shown with $\beta = 1$ in Figure 5-6(c). We calculated the time-varying β ratios of all of the sampled aggregates. Assuming that the minimum β value represented the point at which the aggregate was nearest breakup, we compiled the minimum β ratios for all aggregates of one particle type (PS, OA, or SG) and took the 1st percentile to be representative of the critical necking for the entire aggregate population, β_{crit} (*i.e.* the amount of necking possible for that aggregate type before it would fragment). This analysis revealed that OA and SG had similar critical necking ratios, β_{crit} = 0.138 and 0.134, respectively, while PS aggregates had a significantly higher value of β_{crit} = 0.237. The larger ratio of the PS flocs means that these aggregates required thicker necks with more interparticle bonds, relative to their size, to avoid fragmentation. Figure 5-6 schematically shows the difference in these critical shapes between PS flocs (Figure 5-6(a)) and the

diatom aggregates (Figure 5-6(b)). Most PE flocs did not show necking behaviors at all and had a convex shape, shown in Figure 5-6(c).

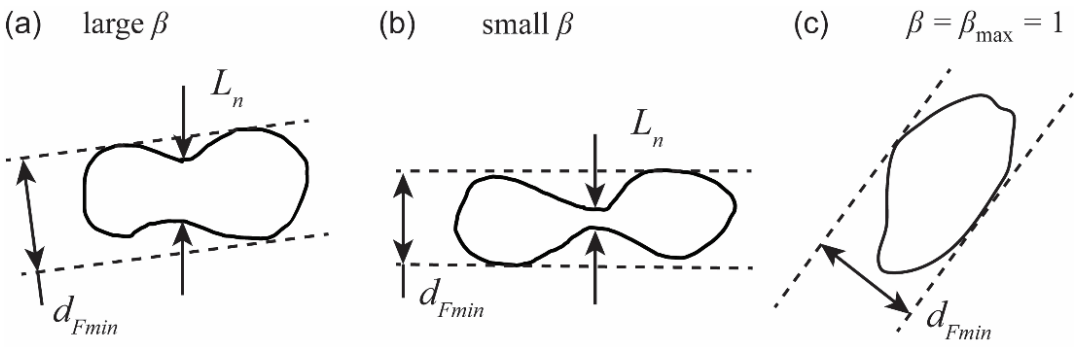

Figure 5-6: Schematic diagram showing the neck size and minimum Feret diameter.

5.2.3 Fractal Structures and Decay of Breakup Strength with Size

Equations (5.8) and (5.9) with other literature (Kranenburg, 1994; Matsuo & Unno, 1981) show that the breakup force caused by fluid drag scales as the square of characteristic length scale. Sonntag and Russel (1986), Zaccone *et al.* (2009), and Rau *et al.* (2018) showed a logarithmic decay of breakup strength with floc size. If we assume that an aggregate's strength is determined by the number of primary particle contacts at its fracture plane, the strength would be expected to decrease with increasing aggregate porosity (or decreasing fractal dimension). Various strength-size relationships for aggregates have been reported in the literature. We used a size exponent x to relate the breakup stress σ_y and the particle length scale. Bremer *et al.* (1989) and Kranenburg (1994) reckoned that very few particles linked aggregates together. Their assumption of only one bonding unit led to a size exponent of x = -2, which gave,

$$\sigma_y \sim d_{eq}^{-2}. \tag{5.10}$$

However, their study did not account for any particle deformation or necking. Additionally, experimental work done by Saha *et al.* (2016) obtained a size exponent of x = -1.6 for microplastic aggregates over a wide size range (10^1 to 10^3 μm). To derive strength-size relationships for our data, we assumed that aggregates of the same type shared a similar fractal dimension *Df* (Burd & Jackson, 2009; Jiang & Logan, 1991), defined as,

$$m = m_1 \left(\frac{d}{d_1} \right)^{Df}, \tag{5.11}$$

where primary particles have identical diameters and masses of d_1 and m_1. The symbols d and m are the diameter and mass of the aggregate. Next, we calculated the solid volume fraction of an aggregate, written as,

$$1 - \varphi = \frac{m}{m_{Df=3}} = \left(\frac{d}{d_1} \right)^{Df-3}, \tag{5.12}$$

where φ represents the porosity of aggregates and $m_{Df=3}$ is the mass of the aggregate if it were completely solid. If we assume aggregates have a uniform internal structure, the contact area at the neck of a deformed aggregate scales with the volume fraction of solids 1- φ. Then, the critical necking stress σ_n as a function of the neck size d_n can be written as,

$$\sigma_n = \sigma_1 \left(\frac{d_n}{d_1} \right)^{Df-3}, \tag{5.13}$$

where σ_1 represents the adhesive stress between two primary particles. This equation shows that the stress required to break apart a deformed aggregate is a function of its interparticle bond strength and its porosity. It is noted that *Df* = 1 represents the case of a linear aggregate with only one bond, which reduces to the exponent of x = -2 derived in previous

studies (Bremer *et al.*, 1989; Kranenburg, 1994). Equation (5.13) also shows that the necking stress reduces to just the interparticle bond strength for a solid aggregate ($Df = 3$), which would be representative of the tensile fracture strength in a solid material.

We used both the non-fragmenting aggregates, discussed in Section 5.2.2, and disrupted aggregates to estimate the critical necking stress as a function of aggregate size. For the fragmenting particles, we assumed the necking stress just prior to breakup was the critical value. For all breakup events, we plot the pseudo necking stress calculated from the breakup force using Equation (5.8) and their pseudo neck size calculated from the critical necking ratio β_{crit}. We could not define a characteristic neck size for disrupted aggregates as the neck size decreased to zero. To estimate the strength of the deforming, but not fragmenting aggregates, we calculated the maximum necking stress experienced by the aggregates discussed in Section 5.2.2 over the time they were tracked using the simplified force expression in Equation (5.9) and their neck size. If a neck was not detected, we replaced the neck size with the minimum Feret diameter. We only analyzed deforming aggregates so any aggregates with an aspect ratio of $AR < 2$ were rejected, where the aspect ratio was defined as the major-to-minor axis ratio of an ellipse fitted to the aggregate image. Next, we grouped them into logarithmically spaced size bins commonly used in instruments for particle size measurements (*e.g.* LISST-HOLO2, Sequoia Scientific) and picked the top 10^{th} percentile in necking stress for each size bin, which we assumed was approaching the critical necking stress required for breakup for each aggregate size class. Figure 5-7 plots the necking stress of these nearly broken particles with that of the disrupted aggregates, and the predicted necking stress versus the neck size using Equation (5.13) and four example fractal dimensions. We used the primary cohesive stress of $\sigma_1 = 1$ Pa for PS

aggregates, which was obtained from the XDLVO analysis assuming an interparticle force of 10^{-11} N and a particle size of 3 μm. We estimated the primary cohesive stress to be approximately σ_1 = 10 Pa for the algae aggregates to plot Equation (5.13) in Figure 5-7(a) and (b). This value qualitatively makes sense relative to the predicted interparticle forces of the PS and PE particles if the algae contact areas are approximately 10^{-11} m^2. Overall, the critical necking stress for the OA and SG aggregates showed a decaying trend with increasing aggregate size and fractal dimensions of 1.5~2.0. The strength-size relation of the PS aggregates was similar, but shifted to lower strengths given their weaker interparticle bonds.

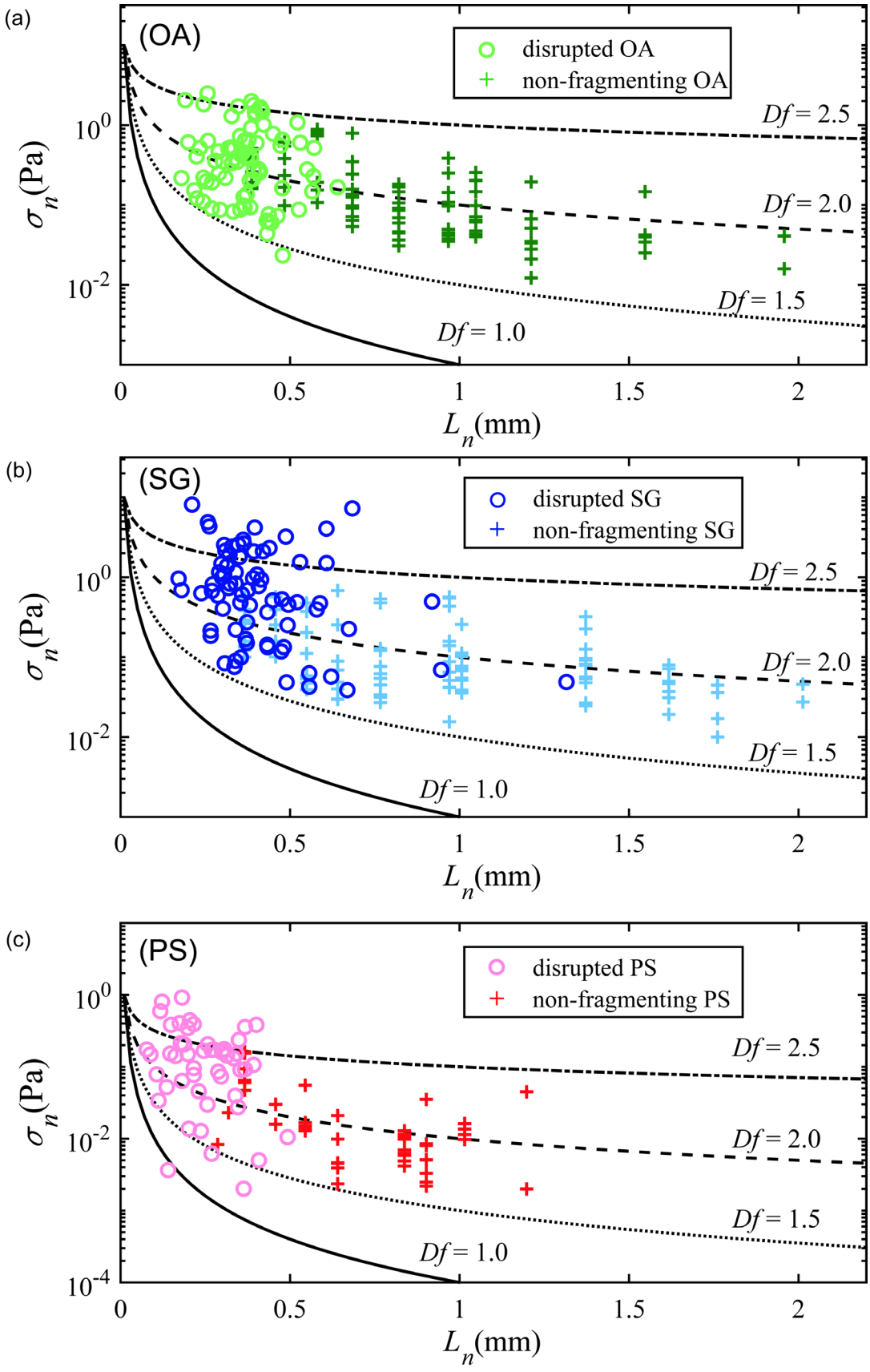
(a)
(OA)
disrupted OA
non-fragmenting OA
Df = 2.5
Df = 2.0
Df = 1.5
Df = 1.0
σ_n(Pa)
10^0
10^{-2}
0
0.5
1
1.5
2
L_n(mm)
(b)
(SG)
disrupted SG
non-fragmenting SG
Df = 2.5
Df = 2.0
Df = 1.5
Df = 1.0
σ_n(Pa)
10^0
10^{-2}
0
0.5
1
1.5
2
L_n(mm)
(c)
(PS)
disrupted PS
non-fragmenting PS
Df = 2.5
Df = 2.0
Df = 1.5
Df = 1.0
σ_n(Pa)
10^0
10^{-2}
10^{-4}
0
0.5
1
1.5
2
L_n(mm)

Figure 5-7: Necking stress as a function of the neck size for non-fragmenting (+) and fragmenting aggregates (○). The four black curves represent size-dependent necking stress predicted by Equation (5.13) for varying fractal dimensions.

5.2.4 Accumulated Stress of Aggregates and Colloid Flocs

This study uniquely resolved the details of dynamic aggregate fragmentation. It allowed us to couple the morphological evolutions to the time-varying fluid force and highlighted the importance of elongation and necking before breakup. To quantify the total deformation of an aggregate, we estimated the aggregate strain $\varepsilon = \left(L_{ma} - d_{eq}\right)/d_{eq}$ by assuming each aggregate was initially shaped like a perfect sphere. While a simplification, it is true that the aggregates in these experiments had more spherical shapes after purely AM tank operation, whereas the elongation primarily occurred during the fragmentation process. We also defined a particle Reynolds number $\mathrm{Re} = d_{eq}^2 G/\nu$, using equivalent circular diameter d_{eq} as the characteristic length scale. The velocity scale was the velocity difference across the particle and can be written as $d_{eq}G$. This Reynolds number definition roughly compares the relative importance of the inertial terms in Equations (5.8) and (5.9) to the viscous drag terms acting on the aggregates. Figure 5-8 shows the aggregate strain as a function of the particle Reynolds number for the disrupted aggregates, where the symbol color denotes if the aggregate experienced either increasing or decreasing shear prior to breakup, defined as an increase or decrease of at least 10% over the previous second. Figure 5-8 shows that there is little difference in the deformation of aggregates at Reynolds numbers less than

~fifteen, where the viscous drag force governed the fragmentation. At higher Reynolds numbers, we observed differences as inertia played a more important role in the breakup mechanism. Diatom aggregates seemed to reach higher strain (*i.e*. they elongated more) when exposed to decreasing shear. We could not find PS aggregates at these higher Reynolds numbers for comparison due to their small sizes. As aggregates deform, the internal stress caused by fluid forces fractures internal bonds and causes restructuring. The aggregate strain, thus, is representative of an aggregate's state of fragility. Deformation continues to occur if aggregates can still rearrange their internal bonds with continued forcing. Increasing shear exposure means that the aggregates experienced a growing hydrodynamic force as they elongated and weakened. This led to less overall deformation as the hydrodynamic forces quickly exceeded the strength of the weakening aggregate. Conversely, aggregates exposed to decreasing shear experienced a weakening hydrodynamic force as they elongated. This allowed these aggregates to restructure and elongate for longer before the decreasing hydrodynamic forces exceeded the aggregate strength. The hydrodynamic force calculation provided by Equations (5.8) and (5.9) does not fully explain this transient behavior since the model assumes a dynamic equilibrium at the point of breakup and ignores the temporal evolution leading up to that point. Moreover, models assuming rigid particles also cannot account for fragmentation under a decreasing shear condition. The time variation of aggregate strength likely provides a plausible explanation for breakup under these conditions and will be important for parameterization of disaggregation in unsteady (*i.e*. turbulent) flows.

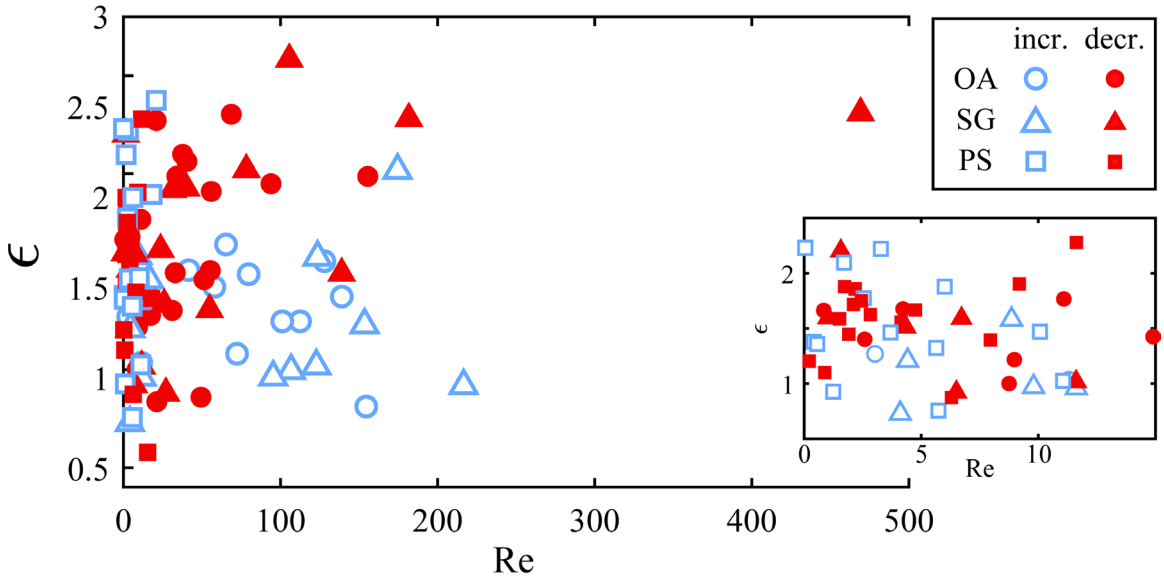

Figure 5-8: Aggregate strain as a function of particle Reynolds number for aggregates of OA (○●), SG (△▲), and PS (□■). Blue hollow symbols (○△□) represent disrupted aggregates with increasing shear exposure, and red solid symbols (●▲■) represent decreasing shear exposure.

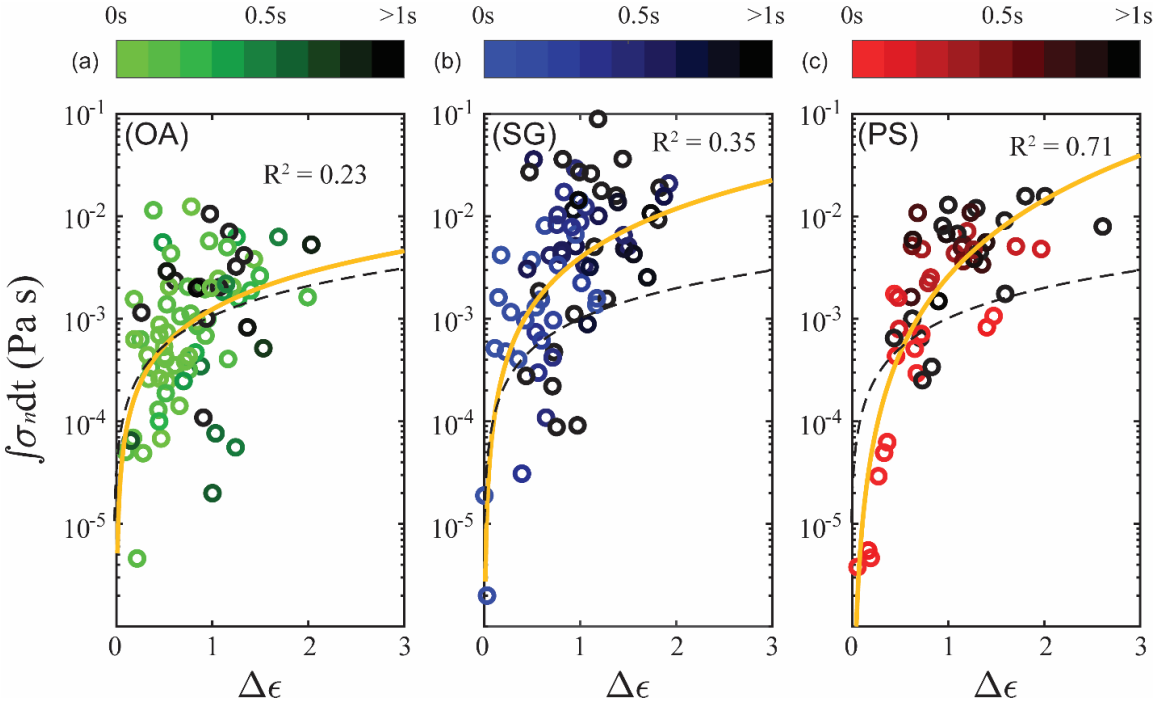

Figure 5-9: Accumulated internal stress as a function of strain difference at breakup, plotted in semilogarithmic scale. The color shading of every individual breakup event is scaled by total exposure time from a frame with the smallest strain to breakup. The yellow line indicates the best correlation, and the black dashes line represents the linear relation for water.

As the above results showed, the breakup of aggregates required forcing over time and a weakening of their internal bonding network. To investigate this further, we plot the accumulated internal stress of each aggregate against its strain difference in Figure 5-9. Comparably, Saha *et al.* (2016) proposed a similar breakup mechanism due to drag stress accumulation. Since we could not track the entire forcing history of each aggregate from the point FM started to the point of breakup, we calculated the integrated stress and strain

difference using only the measured lifespans of each aggregate. We defined the strain difference, $\Delta\varepsilon$, as the difference between the smallest strain measured for each aggregate and its strain at breakup. To characterize the accumulated internal stress, we integrated the instantaneous necking stress, (defined as the instantaneous force expressed in Equation (5.9) divided by the instantaneous neck area) from the time frame with the smallest strain to breakup. We observed that the cumulative internal stress was positively correlated with total deformation of disrupted aggregates. Similar accumulations of internal stress caused algae aggregates (Figure 5-9(a) and (b)) to deform less than PS flocs (Figure 5-9(c)). Yellow lines in Figure 5-9 represent a power fit from a linear regression of the scattered data. PS flocs in Figure 5-9(c) showed the strongest correlation ($R^2 = 0.71$) on a logarithmic scale, but algae aggregates displayed a weaker trend ($R^2 = 0.23$ for OA and 0.35 for SG). PS flocs had a better linear regression likely because of more homogeneous structures and more uniform interparticle forces compared to OA and SG. The possibility of more-varied cohesive content (*e.g.* transparent exopolymer particles) in the algae aggregates could also explain their variability.

The time integration of the stress is representative of the total amount of fractured bonds in an aggregate. The strain difference quantifies the rearrangement of internal bonding networks, so we expect it to be positively correlated to the stress accumulation. We compared the aggregate deformation behaviors with that of a parcel of Newtonian fluid (water), shown as the black dashed line in Figure 5-9. In a Newtonian fluid, the viscous stress is a linear function of its strain rate. If we relate the integration of internal stress to the strain difference, $\int \sigma_n dt \sim \Delta\varepsilon^n$, a Newtonian fluid has an exponent of $n = 1$. The

exponent for the PS flocs was $n = 2.47$, and best correlations for OA and SG are 1.19 and 1.58, greater than 1 as well. Comparisons between the yellow and black lines generally show that the aggregates deformed less than a Newtonian fluid would have under similar cumulative stresses. This is expected given that Newtonian fluids have free molecules and continuous structures, allowing easier and more homogeneous strain deformation. However, the exponent $n > 1$ for the PS aggregates with a relatively strong correlation indicates that the apparent viscosity of PS flocs increases as stress increases. This behavior is similar to a shear thickening fluid. The weak correlations for the algae aggregates show that more complex interactions are governing their deformation. Therefore, the effective properties of an algae aggregate could display characteristics of elasticity, plasticity, and viscosity, *i.e.*, the internal stress could be a function of both strain and strain rate, $\sigma \sim f\left(\varepsilon, \partial\varepsilon/\partial t\right)$.

The shade of each fragmentation event is also plotted based on the total strain time used in the integration. There was no evident relation in exposure time for PS flocs, which indicates that strong shear with short time exposure had a similar effect on the breakup of PS flocs to a case with small shear and a long time exposure. OA and SG aggregates behaved similarly, but we observed that longer shear exposure generally tended to cause more deformation.

5.3 Summary

In this chapter, we performed fragmentation experiments on four different aggregate types: OA, SG, PS, and PE. We utilized a rotating and oscillating roller tank to expose aggregates to laminar oscillatory shear flow and captured the Lagrangian time series of individual aggregates. Similar fluid shear caused the breakup of OA, SG, and PS flocs but failed to disrupt PE flocs. The unique problem of interparticle adhesive strength between marine algae cells stemmed from the stickiness of EPS, in which we had to consider the biological sticky content more than the classic colloidal aggregation theory. The result uncovered the cohesive strength of OA and SG aggregates between PE microspheres that were much stronger than those and the PS particles. The XDLVO theory confirmed the relative strength of the plastic aggregates, which also bounded the interparticle adhesive forces of the OA and SG aggregates investigated. All types of disrupted aggregates had to experience large enough shear and underwent a substantial elongation with subsequent necking in order to fragment. In addition to analyzing fragmenting aggregates, we analyzed thousands of deformed, non-fragmenting aggregates and found that the ratio of their neck size to aggregate width was smallest for the PS aggregates. A simplified analysis of the hydrodynamic forces acting on the elongating aggregates allowed us to define the time-varying stresses leading to deformation and breakup. We found that this transient forcing played a crucial role in the fragmentation process. . The aggregates showed a decay of breakup strength with neck size that was primarily a result of the porous structures of the aggregates. To describe this behavior, we derived an expression relating the bonding stress between primary particles to the breakup stress required to fragment an aggregate.

Our experimental methodology had some limitations in that we could only resolve a two-dimensional aggregate projection from the single camera system. Thus, we could not measure the aggregate thickness along the axial direction of the tank. Our camera resolution was also not capable of resolving the primary particle sizes for the SG and PS samples. Both effects, plus limited camera recording time, prevented us from obtaining the entire shear and morphological history of the aggregates. Additionally, our particle tracking method only allowed us to confirm a small number of breakup events with high confidence and we observed many more breakup events than were reported. A longer recording time is desirable for future implementations.

Despite these limitations, this study has demonstrated many important aspects of the transient deformation and fragmentation process. In particular, this study demonstrates the importance of exposure time. High enough shear can undoubtedly disrupt aggregates, but low-magnitude shearing can also cause fragmentation if the exposure time is sufficient to cause aggregate restricting and deformation. Figure 5-4 shows that breakup events occurred at very low shear rates. In the context of the deformation results, it is likely that these events were preceded by deformation resulting in a fragile floc that could be fragmented by a very low shear rate. It is important to discuss this time exposure in the context of the duration of shear events in the ocean. It should be emphasized that the maximum experiment time was less than three minutes. Natural phytoplankton aggregates can easily be exposed to low values of shear for hours or even longer. For example, Franks *et al.* (2022) have observed that the median dissipation rates were smaller than 10^{-8} W/kg in the upper 100 m, and that 99% of observations had dissipation rates less than 10^{-6} W/kg. The turbulence intensity decreased rapidly with depth and the most frequent turbulence

levels were low enough that breakup caused by high shear cannot be dominant. Low shear but long time exposure likely provides a feasible explanation for aggregate fragmentation in an environment of low turbulent dissipation energy. Further investigations should be implemented for evidence of fragmentation due to low shear in the mixed layer.

This chapter revealed that aggregates have some fluid-like behavior. However, their loose and porous structures of connected primary particles still move with limited freedom. Future investigations should expose individual aggregates to a more controlled hydrodynamic environment to further clarify these properties. The breakup strength expression (Equation (5.13)) provides the possibility of obtaining an equivalent interfacial effect for aggregates from fractal dimension and primary particle bonding strength. Fractal dimensions are typically used to describe large populations of aggregates (Burd & Jackson, 2009; Jiang & Logan, 1991; C. P. Johnson et al., 1996), but the aggregate-to-aggregate variation will always cause outliers in statistical analyses. More investigations are desired in order to quantify the expected aggregate-to-aggregate variability within aggregates of varying particle types.

Chapter 6

Conclusions and Future Work

This dissertation presented the development of the in-situ disaggregation system and described the laboratory experiments for a comprehensive study on the fragmentation of marine snow particles. This final chapter of the dissertation summarizes the work completed regarding each objective in Section 6.1. Next, in Section 6.2, we draw major conclusions and state broader impacts and research contributions to the science community. Finally, Section 6.3 addresses the recommended future research directions.

6.1 Summary of Research Objectives and Tasks

Objective 1: Improve and develop a new in-situ disaggregation system.

Task 1.1 implement and verify the system with autonomous control during field deployments.

Task 1.2 confirm the existence of aggregates and fragmentation in the mixed layer.

We developed a new in-situ disaggregation system and have implemented the fragmentation experiments in two recent field deployments in the Northeastern United States CS and Lake Tahoe. The new iDAS with portable power supplies had an autonomous control system that allowed for measurement down to 200 m. Chapter 2, with Appendices G and I, describes the concept and detailed design of the system. Using a variable speed thruster, we created turbulent pipe flows inside a tube and exposed naturally occurring aggregates to calibrated turbulence dissipation rates. The measurement in the

Northeastern United States CS captured images of marine snow aggregates at a depth of 200 m. The reconstruction of holograms additionally provided the structures of natural aggregates. We processed the particle size spectra under varying flow conditions and found a decrease in volume fractions of large particles with increasing turbulence intensities. The response of the particle size spectra further revealed that naturally formed aggregates could break due to exposure to turbulence. Another deployment in Lake Tahoe compared populations of suspended particles at two field stations. We did not see the fragmentation of particles at the near-shore station, likely because of upwelling. The offshore station showed distinct changes in particle size statistics between laminar and turbulent flow conditions. The result in Lake Tahoe indicated that freshwater aggregation could be as important as that in the ocean.

Objective 2: Design a laboratory facility for studying disaggregation.

> **Task 2.1** develop an experimental facility that has a controlled fluid flow that exposes formed aggregates to calibrated hydrodynamic shear forces.
> **Task 2.2** create phytoplankton aggregates in the laboratory and expose them to hydrodynamic forces.
> **Task 2.3** Capture breakup events using high-speed imaging techniques and develop an image processing method to automatically analyze a large number of breakup events.

We have designed a novel rotating and oscillating tank to form and disrupt aggregates in the same facility. This novel tank facility superimposes a harmonic oscillation to a constant rotation speed at the tank wall and generates a viscous oscillatory flow inside. We developed an analytical solution to the laminar flow configuration and performed a particle image velocimetry experiment to validate the flow regime. The laminar flow condition is an extension of Stokes' second problem. In the quasi steady flow, the oscillation magnitude

decreases at an exponential rate as we move away from the tank wall. We also expressed transient motions when we started to oscillate the tank from a stagnant condition or solid body rotation. We further characterized the flow using the product of two dimensionless variables, the Reynolds number and the Strouhal number, which defined the thickness of the high-velocity region.

Given proper boundary conditions, the tank could create fluid shear of a similar order of magnitude as the ocean. We also assessed particle trajectories and stable regions by assuming a constant particle settling speed. The result showed that most particles would not have contact with the tank wall, which was in favor of aggregation and breakup experiments in the tank. Disruption experiments using bentonite clay flocs confirmed the performance of the rotating and oscillating tank.

We cultured diatoms and formed phytoplankton aggregates in the laboratory. In order to study the disruption behavior of formed aggregates, we have developed a high-speed-imaging-based algorithm that can automatically capture breakup events within the tank. This algorithm was designed to study unique aggregates and consisted of four major parts: background removal, particle identification, particle matching with tracking, and breakup detection. With the algorithm, we successfully captured many breakup events of Odontella aurita aggregates. The result showed the significance of morphological evolution prior to the breakup, as every disrupted aggregate had to undergo a substantial elongation and be exposed to large enough fluid shear. Therefore, we should no longer model marine aggregates as brittle materials in a simple shear flow. Additionally, this novel method has many advantages. First, we do not need to manually extract formed aggregates and put them into either a shear flow or a turbulent environment. Second, the method allows

coupling the hydrodynamic force with the particle morphology. This tank can expose aggregates to a wide range of shear forces, as we also observed breakup events with a very small shear force comparable to the mixed layer. Moreover, this method tracks many particles simultaneously, allowing for statistical analysis over both non-fragmenting particles and disrupted aggregates.

In addition to the listed tasks, we have conducted supplemental experiments by rotating and oscillating the tank for a long time period. Running this rotating and oscillating tank for several hours could have inside aggregates reach a population balance between aggregation and breakup. The time-varying population characteristics also reflected the breakup strength of aggregates. We used mass conservation to develop a simple imaging method to determine the fractal dimension of formed aggregates. Two diatom species, Odontella aurita and Skeletonema grethae, showed different fractal dimensions. Skeletonema grethae aggregates had a smaller fractal dimension, which indicated more loose structures. These aggregates also had faster fragmentation rates, as Odontella aurita required more than three hours to balance aggregation and breakup.

Objective 3: characterize the breakup strength of laboratory-made aggregates.

Task 3.1 develop a force balance model to predict the fluid force on aggregates.
Task 3.2 characterize the disaggregation of a wide range of aggregate materials, including algae and microplastics.
Task 3.3 use XDLVO theory and microplastic particles to estimate the cohesive force within algae aggregates.
Task 3.4 clarify the effects of biological bonding in algae aggregates by comparing the morphology and breakup behaviors of marine snow to flocs of plastic microspheres.

We have performed fragmentation experiments on four different material types: Odontella aurita, Skeletonema grethae, sulfate polystyrene, and polyethylene. The experiment utilized the facility and image processing method completed in Objective 2. We successfully captured breakup events of OA, SG, and PS aggregates but failed to disrupt PE flocs, which revealed a stronger cohesive interaction within the PE flocs. Fragmented PS flocs exposed to similar fluid shear had a smaller size than OA or SG aggregates. Therefore, the two plastic colloidal flocs bounded the strength of the two diatom aggregates. Additionally, the XDLVO theory calculated the primary bonding force between two microspheres without biological effects. The theory predicted a larger adhesive force for PE flocs. Breakup results and the XDLVO theory gave us an idea of the primary bonding force between algae cells.

This study uniquely provided a detailed dynamic resolution of particle fragmentation. We summarized the morphological behavior of all disrupted aggregates prior to the breakup. Unlike brittle materials, these soft aggregates had to undergo substantial fluid shear and a significant elongation with a re-orientation. More importantly, necking was necessary for all disruption events.

Moreover, we modified the Maxey-Riley equation and added one coupling force term to explain the fragmentation. In brief, we performed force analyses separately and assumed that two subaggregates were bounded by a tensional force. This model allowed for estimating the necking stress for tensioned aggregates. By incorporating non-fragmenting particles during the experiment, we found that the power law relation of the breakup strength to particle size originated from porous structures of aggregates. The breakup stress was also related to the fractal dimension of aggregates and their primary bonding stress

estimated from the XDLVO theory. Additionally, the time-varying morphology and neck forces also revealed viscoelastic behavior of aggregates.

6.2 Primary Research Contributions

From the objectives and tasks in this dissertation, the following primary conclusions and research contributions are drawn regarding the work completed:

1. We have developed an in-situ disaggregation system that can be operated remotely and expose aggregates to varying flow conditions.
2. We found that marine snow aggregates could fragment due to controlled turbulence at a depth of 200 m in the Northeastern United States Continental Shelf.
3. We found aggregated phytoplankton not uniformly distributed in Lake Tahoe. Aggregation also plays an important role in the sedimentation process in a freshwater body.
4. We provided an analytical solution to a viscous flow inside a cylinder whose wall undergoes a harmonic oscillation along its axial direction. The Reynolds number and Strouhal number characterize the oscillatory shear flow inside a cylindrical tank and determine the thickness of high-speed flow regions.
5. Given proper boundary conditions, the rotating/oscillating tank can provide laminar oscillatory flow and generate shear in a similar order of magnitude to the ocean. It does not require any manipulation prior to fragmentation studies and enriches the toolset needed for the community.

6. The rotating/oscillating tank with developed particle tracking algorithms could provide a Lagrangian time series of particle morphology and shear exposure. Among many breakup events, we found that small laminar shear comparable to the mixed layer could also cause the breakup.
7. Laboratory-made Odontella aurita aggregates required more time to reach a steady state in which aggregation was balanced with breakup. Faster breakup rates correspond to less compact structures.
8. Laboratory-made diatom aggregates were stronger than sulfate polystyrene flocs but weaker than polyethylene flocs. Microplastic flocs had more homogeneous structures and inter-particle forces than algae aggregates.
9. Necking and elongation behaviors were important to aggregate disruption in a shear flow. Deformed algae aggregates could stay intact with a smaller neck size.
10. The breakup stress followed a power law decay with the aggregate size due to the porous structures. A fractal dimension representing the porosity of a population could relate the primary bonding stress between two cells to the cohesive force within aggregates.
11. Accumulation of the internal stress was responsible for the total deformation and caused the breakup. The time-varying breakup behaviors showed viscoelastic behavior.

6.3 Recommended Future Research Directions

Based on the dissertation work, we are recommending the following research directions. Chapter 2 describes the implementation of the in-situ disaggregation system. We are proposing two improvements for aggregate fragmentation. First, we will integrate the measurements of ambient particle size spectra and backscattering signals to do a mass normalization, which will solve the problem if any sudden circulation alters the ambient particle population. Second, we are developing a new code for reconstructing the holograms we acquired. The current processing with HOLO Batch cannot accurately capture the morphology of marine particles and has a very high uncertainty, even though it has already shown fragmentation due to higher turbulence intensities. In the future, a new hologram reconstruction algorithm will replace the HOLO Detail. Better particle image quality will allow us to identify aggregates and diatom species, and more importantly provide more reliable particle size statistics. Additionally, we are going to incorporate the disaggregation results with other datasets collected by our collaborators. Chemical and biological analyses will provide more insights into the entire environmental study. Specifically, we have collaborators studying the TEP content (transparent exopolymer particles), which are biological gels that form natural aggregates. Knowing the TEP concentrations will facilitate our understanding of aggregate formation and its mechanical strength against ambient turbulence. Also, other collaborators during the deployment in the Northeastern United States CS are investigating the bacteria groups, dissolved organic carbon, particulate organic carbon, suspended particulate matter, and many other variables in the ocean. We will have a better understanding of the natural aggregates after compiling datasets on the physics, chemistry, and biology of the environment.

Chapter 2 also describes varying particle size distributions due to different turbulent flow conditions. As better particle imaging techniques and improved reconstruction algorithms obtain the size spectra more accurately, we can obtain the maximum stable aggregate size for a given turbulence dissipation rate. A force balance model can further couple the hydrodynamic force with the bonding force within the aggregate. This method can alternatively apply statistics of large populations to predict the strength of natural marine aggregates.

Chapter 3 develops a promising experimental facility that can expose laboratory-made aggregates to calibrated laminar flow. It will be a great advancement if we can expose laboratory-made aggregates to turbulent flows and keep the capability of coupling the forces with morphology. Turbulent flows are more representative of a natural aqueous environment than laminar flows. Future measurements can greatly benefit from a calibrated turbulence tank and 3D-PTV techniques. Current particle identification and matching algorithms can be modified to adapt to the new experimental setups. Additionally, two or more cameras can also provide 3D information on aggregates. The tumbling and rotation can be important to the morphological analysis. It will also be interesting to study the aggregate-flow interactions. Large aggregates affect the surrounding fluid flow, which also influences the drag force and added mass force.

Chapter 4 describes the experiments of time-varying particle statistics, which has great potential to calibrate the breakup rates of aggregates. Future work can design a closed system with calibrated flow conditions. We can apply similar sampling and illumination methods but expose aggregates to isotropic homogeneous turbulent flows. Then the population balance model described in Chapter 1 can extract the aggregation term and

predict the fragmentation rate for a given population. The breakup rate can be proven to be a function of the ambient flow condition and bonding strength of particles.

Chapter 5 reveals the viscoelasticity of individual aggregates. It is challenging to consider the stress-strain relationship without relaxation. Also, the time-varying fluid shear introduces more variables and makes the problem more difficult. In the future, we can consider devices using Couette flows, which can expose aggregates to a more controlled hydrodynamic environment. Furthermore, we can also attempt to measure the aggregates in a rheometer or a viscometer, enhancing our understanding of their mechanical properties.

We are also considering introducing more material types in laboratory experiments. It will be interesting to combine inorganic minerals like bentonite clay with more than one type of algae species. Interactions with different material types potentially generate distinct characteristics of deformation and fragmentation. We will also learn more about the TEP content. Future work related to these transparent gel-like particles will provide more insights into the formation of aggregates.

Appendix A. Derivation of Viscous Fluid Flow inside an Oscillating Tank with a Sine Wall Boundary Condition

Here we are demonstrating the derivation of the oscillatory flow inside a cylinder whose wall experiences an oscillation in the form of a sine function. Instead of Equation (2a), we have a different boundary condition at the wall,

$$u_\theta = a \cdot \sin(\omega t) \text{ at } r = R,\ t \geq 0, \tag{A.1}$$

Using the same nondimensionalization process, and then applying the Laplace transform, this boundary condition is written as

$$F\left(\eta_R, s\right) = \frac{1}{s^2+1} \text{ at } \eta = \eta_R, \tag{A.2}$$

Solving the modified Bessel function in Equation (2.7), with boundary conditions shown in Equation (2.8b) and Equation (A.2), the dimensionless velocity after an inverse Laplace transform now becomes,

$$f\left(\eta, \tau\right) = \frac{1}{2\pi i}\int_{c-i\infty}^{c+i\infty} \frac{1}{s^2+1} \cdot \frac{I_1(\eta\sqrt{s})}{I_1\left(\eta_R\sqrt{s}\right)} \cdot \exp\left[s\tau\right] ds. \tag{A.3}$$

We then apply the Residue Theorem and sum up all non-zero residues to obtain a similar analytical solution. The solution for the dimensionless velocity for this boundary condition also contains a quasi-steady and transient part and is written as

$$f(\eta,\tau)=\sum \mathrm{Res}[g,z]=\frac{1}{2}\left[\exp[i(\tau-\pi/2)]\frac{I_1\left(\eta\sqrt{i}\right)}{I_1\left(\eta_R\sqrt{i}\right)}+\exp[-i(\tau-\pi/2)]\frac{I_1\left(\eta\sqrt{-i}\right)}{I_1\left(\eta_R\sqrt{-i}\right)}\right]$$
$$+\sum_n^{\infty}\exp\left[z_{0,n}\tau\right]\frac{4z_{0,n}^{\frac{1}{2}}}{(z_{0,n}^2+1)\eta_{R?}}\cdot\frac{I_1\left(\eta\sqrt{z_{0,n}}\right)}{I_0\left(\eta_R\sqrt{z_{0,n}}\right)+I_2\left(\eta_R\sqrt{z_{0,n}}\right)}.$$

(A.4)

Here, we observe that the quasi-steady part is the same as the analytical solution for the cosine boundary condition except for a phase offset of $\pi/2$. Additionally, the transient part has a different numerator due to the gentle starting condition provided by the sine oscillation instead of the sudden starting condition created by the cosine function.

Appendix B. Major Steps of Binarization for Aggregate Identification

In Chapter 4, we outline procedures to identify particles with the major steps shown in Figure 4-3. Here we provide additional details of each processing step, with specific user-defined inputs summarized in Table B-1:

1. *Determining aggregate sub-images*: We found that processing each aggregate image separately helped account for non-uniformities in the lighting and resulted in more consistent aggregate identification and sizing. To determine aggregate sub-images, we zeroed out all pixels whose grayscale intensity was less than the brightest 5%, based on a histogram of all pixel grayscale intensities in each image after masking and background removal. This procedure ensured that each sub-image would have a black boundary. Then we eliminated any remaining bright areas smaller than 16 pixels, assuming that aggregates smaller than this were too small to resolve accurately with our imaging system. We then extracted rectangular sub-images that were the smallest boxes containing each of the remaining illuminated areas. An example sub-image containing one aggregate is shown in Figure 4-3(b).
2. *Eliminating out-of-focus aggregates*: The high-speed camera sometimes captured aggregates outside but near the light sheet. These out-of-focus aggregates generally had pixels with uniform brightness that were not as bright as those in the light sheet, but were still bright enough to pass through the 5% threshold described above. In-focus aggregate images, in contrast, were either all bright pixels or a combination of bright and dull connected pixels, depending on morphology. Using this image characteristic as a means to gauge particle focus, we retained all aggregate images

where at least the nine brightest pixels passed Ostu's cutoff binarization threshold (Otsu, 1979), calculated from the entire gray camera image, and eliminated all remaining aggregates. This retained all aggregate images where we were confident that at least some portion of the aggregate was located within the light sheet. We also required that the intensity of the in-focus pixels be at least 50% of the highest intensity observed in the gray image. This last condition was necessary if the Otsu's threshold happened to be very small for a given camera image, which occurred in images with sparse aggregate populations.

3. *Aggregate edge detection*: To detect the edges of the aggregates, we applied a Sobel gradient operator (Sobel & Feldman, 1968), as shown in Figure 4-3(c), followed by a local adaptive binarization step, Figure 4-3(d). To finalize the conversion of the aggregate image into a binary form, we dilated and then eroded the bright areas by two pixels and filled any remaining holes, which had the effect of connecting and filling bright regions within one aggregate without increasing the overall outer dimensions. An example result is shown in Figure 4-3(e). Figure 4-3(f) shows the resulting aggregate outline compared to the original raw image.
4. *Aggregate grayscale image masking*: Finally, we masked the individual gray images for the particle matching procedure. We used the binary images described above for aggregate size and morphology measurements. However, the grayscale intensities of each aggregate were useful for matching aggregates between camera frames. As described in Appendix C, we used each binary sub-image as a mask to inform which grayscale pixels should be retained to isolate the raw aggregate image for the matching algorithm. An example final image is shown in Figure 4-3, where we

extracted the grayscale aggregate images from the raw image based on their location and the corresponding binary aggregate mask.

Table B-1: User-defined image processing parameters.

Processing step	Parameter	Value used
1	Gray value cutoff threshold	5%
1	Area cutoff threshold	16 pixels
2	In-focus area cutoff threshold	9 pixels
3	Edge dilation and erosion size	2 pixels

Appendix C. MQD and MQD_R Calculation for Particle Matching

As described in the manuscript, the third step of the particle matching algorithm relied on the calculation of the MQD and MQD ratio, MQD_R, to ultimately determine match success. Chapter 4 shows three successful aggregate matchings with different criterions fulfilled. We implemented the calculation procedure as follows:

1. In the first frame under consideration, we generated an interrogation window g_1 for the aggregate being matched. This window was the aggregate's sub-image expanded by 8 pixels on each side. In the next frame, the interrogation window of a possible match, g_2, was taken as the sub-image of the possible matching aggregate. These interrogation windows are shown in the left two columns in Figure C-1.
2. Before we calculated the MQD, we rejected candidates if their interrogation windows, g_2, were larger than the g_1 interrogation window after expansion, which meant that the aggregate in the second frame was substantially larger than that in the first frame and could, thus, not be a match.
3. We then calculated the quadratic difference between the two grayscale interrogation windows as follows,

$$QD(m,n) = \frac{1}{M_2 \cdot N_2} \sum_{i=0}^{M_2-1} \sum_{j=0}^{N_2-1} \left[g_2(i,j) - g_1(i+m, j+n) \right]^2 \tag{C.1}$$

where M_2 and N_2 were the maximum number of x and y pixels in the g_2 interrogation window, respectively. Varying the values of m and n allowed us to find the position

where the two interrogation windows best matched (*i.e.* the position where the QD was minimized).

We determined a match between two aggregates if the MQD was smaller than two times the standard deviation of grayscale intensities in the entire gray camera image. This criterion was sufficient to match the aggregates shown in Cases 1 and 2 in Figure C-1, as it represented the aggregate with the most-similar grayscale image. We found that the MQD matching procedure alone would sometimes fail for the largest aggregates, particularly if the aggregate rotated or deformed substantially between frames. The resulting variation in the aggregate image led to higher MQD values and a failed match. To take into account the larger size of the aggregates, we considered one alternative variable if the initial matching criterion failed. This criterion was the MQD ratio, MQD_R, defined as,

$$MQD_R = \frac{M_2 \cdot N_2 \cdot MQD}{\sum_{i=1}^{M_1}\sum_{j=1}^{N_1} g_1(i,j)^2 + \sum_{i=1}^{M_2}\sum_{j=1}^{N_2} g_2(i,j)^2}. \tag{C.2}$$

Equation (C.2) compares the MQD to the sum of the squared grayscale intensities from both interrogation windows, which helps to accommodate the aggregate size in the matching procedure. With this ratio, a large aggregate could meet a lower threshold (*i.e.* a higher MQD value) and still be considered a valid match, as shown as Case 3 in Figure C-1. This modification worked for the large aggregates as their unique size and morphologies made them less likely to be mis-matched with other aggregates in the flow. When aggregates met these conditions, we employed a threshold of $MQD_R < 0.1$ to indicate a successful match.

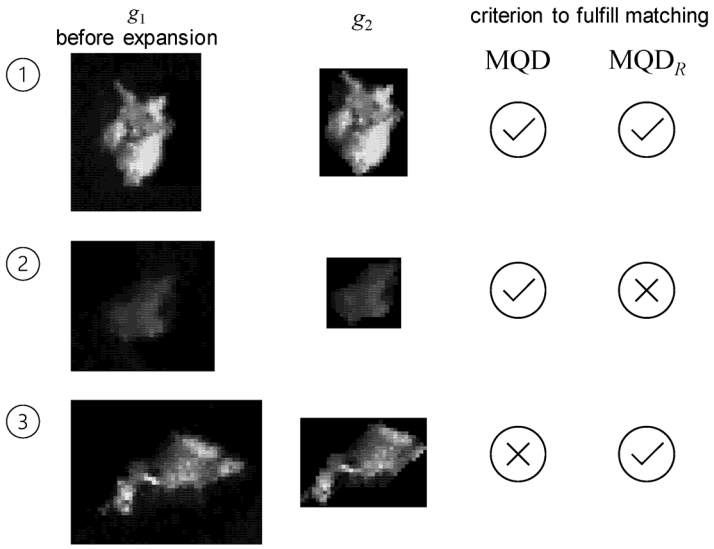

Figure C-1: Three examples of successful particle matchings using different matching criterions. Particle images are shown contained within their interrogation windows (g_1, and g_2) used for the matching procedure.

Appendix D. Manual Check Rubric to Verify Breakup

We concluded the breakup detection algorithm with a manual check to ensure that only actual breakup events were reported. The automated breakup algorithm significantly reduced this workload by identifying all possible breakup events (e.g., 55 breakup events were found out of 642,721 total particles in one experiment). With this shortlist, we could then quickly confirm visually if actual breakup occurred using the following rubrics:

1. Any aggregation event detected by the algorithm (*i.e.* two aggregates becoming one larger aggregate) could not occur right before a given breakup event (within the lifespan of the parent aggregate) since we could not determine if the aggregation was complete or not.
2. The aggregate could have no contact with the tank wall.
3. Any shadow passing by the aggregate could not cause discontinuity in the binarization.
4. Child aggregates had to have a visual connection and share a common orbit and rotation prior to breakup. This criterion eliminated small aggregates close to one another that then moved apart, which could erroneously be detected as a breakup event.
5. Two child aggregates must have a similar grayscale intensity. Different illumination conditions resulted from different depths along the viewing axis, which meant that two aggregates with very different intensities were likely not product of a breakup event.

Ultimately if we could make no specific determination, a breakup event was labeled as suspected and removed from the analysis. These uncertain events represented only 16% of all the potential breakup events detected by the algorithm.

Appendix E. Lewis Acid-Base Energy of Sulfate Polystyrene Microspheres

The PS microspheres in this study are stabilized by sulfate charges, which notably changes the hydrophobic properties. Therefore, we use results from contact angle measurements to determine the Lewis acid-base energy ΔG^{AB}. For the contact angle measurement with single liquid, we refer to the Young Dupre Equation (van Oss, 2008) that links the contact angle θ to polar surface free energy ΔG_{SL} between solid and liquid,

$$-\Delta G_{SL} = \gamma_L \left(1+\cos\theta\right) = 2\left(\sqrt{\gamma_S^{LW}\gamma_L^{LW}} + \sqrt{\gamma_S^+\gamma_L^-} + \sqrt{\gamma_S^-\gamma_L^+}\right), \tag{E.1}$$

where subscripts S or L represents solids or liquids, and γ_L, γ^{LW}, γ^+ and γ^- are liquid surface tension, Lifshitz-van der Waals surface energy (apolar energy), electron accepticity, and electron donicity, respectively. Researchers also implemented contact angle measurements at fluid interfaces to predict the surface energy of materials (Maestro *et al.*, 2014; Snoeyink *et al.*, 2015). Neglecting the equilibrium spreading pressure and any absorption of components from the fluid phases, the equation for measurements at fluid interfaces (Landau & Lifshitz, 1987; Neumann *et al.*, 2010) is given as,

$$\gamma_{p,f_1} - \gamma_{p,f_2} - \gamma_{f_1,f_2}\cos\theta = 0, \tag{E.2}$$

where f_1 and f_2 represent the bottom and upper fluid phases, $\gamma_{p,f}$ is particle-fluid interfacial tension and γ_{f_1,f_2} is the interfacial tension between the fluid phases. The fluid-fluid interfacial tension γ_{f_1,f_2} consists of apolar and polar components and is given as,

$$\gamma_{f_1,f_2} = \left(\sqrt{\gamma_{f_1}^{LW}} - \sqrt{\gamma_{f_2}^{LW}}\right)^2 + 2\left(\sqrt{\gamma_{f_1}^+\gamma_{f_1}^-} + \sqrt{\gamma_{f_2}^+\gamma_{f_2}^-} - \sqrt{\gamma_{f_1}^+\gamma_{f_2}^-} - \sqrt{\gamma_{f_1}^-\gamma_{f_2}^+}\right). \tag{E.3}$$

Van Oss (2008) mentioned at least three contact angle determinations with different liquids to solve three unknowns, γ^{LW}, γ^{+}, and γ^{-}. Maestro *et al.* (2014) measured contact angles of sulfate polystyrene latex microspheres with a mean diameter of 2.9 μm using gel trapping techniques with methanol. They observed contact angles of 76° and 120° at the air-water interface and water-octane interface. Snoeyink *et al.* (2015) applied the same technique and obtained 116° at the water-glycerol interface for sulfate PS particles with a mean size of 1.0 μm. We employ these results from the three measurements since our PS particles have the same surface modification and similar mean size. With the values in Table E-1, we compute the γ^{LW}, γ^{+}, and γ^{-} for sulfate PS microspheres to be 47.6, 1.34, and 15.86 mJ/m^2, respectively. The last procedure is to calculate the polar surface energy of PS particles in water, which can follow the equation (van Oss, 2006),

$$\Delta G_{131}^{AB} = -4\left(\sqrt{\gamma_1^+} - \sqrt{\gamma_3^+}\right)\left(\sqrt{\gamma_1^-} - \sqrt{\gamma_3^-}\right), \tag{E.4}$$

where subscripts 1 and 3 represent plastic particles and water. We obtained ΔG^{AB} = -16.6 mJ/m^2 for sulfate PS microspheres.

Table E-1: Surface energy γ_L, γ^{LW}, γ^{+}, and γ^{-} values for water, octane, and glycerol, in mJ/m^2 (van Oss, 2008).

Liquids	γ_L	γ^{LW}	γ^{+}	γ^{-}
Octane	21.6	21.6	0	0
Water	72.8	21.8	25.5	25.5
Glycerol	64.0	34.0	3.92	57.4

Appendix F. Aggregation Kinetics Characterization of Polystyrene and Polyethylene Microspheres

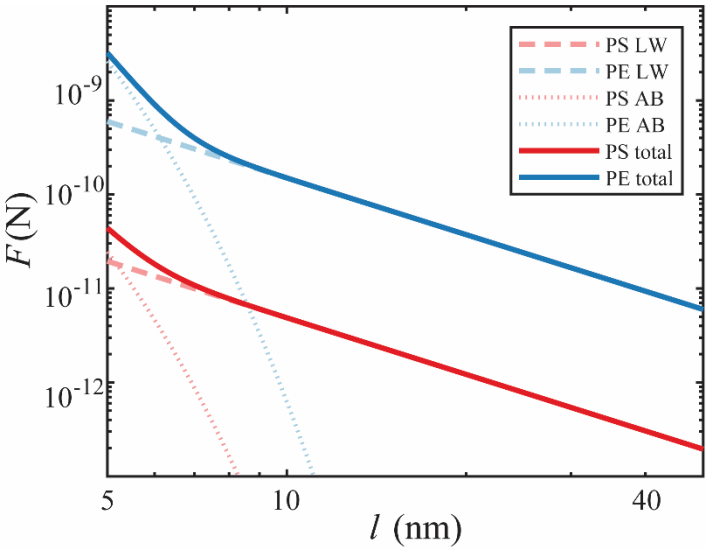

Figure F-1: Interfacial interaction forces of PS and PE microspheres during the experiment. Solid lines represent the attraction force of two material types between primary particles. Dashed lines are components of the van der Waals and Lewis acid-base forces.

The salt concentrations used in this study were all high enough to effectively screen the electrostatic repulsive force component in the XDLVO analysis. More explicitly, using $CaCl_2$ and NaCl in our experiments with the given concentrations, the Debye lengths in Equation (5.4) were smaller than one nanometer. Therefore the repulsive force was negligible regardless of the surface potential on microspheres. Figure F-1 plots the attraction interaction with the van der Waals force and Lewis acid-base force as functions of separation distance. The Lewis acid-base force rapidly diminished with the separation distance l, while the van der Waals interaction decayed at a lower rate. The larger size and

stronger hydrophobicity of PE microspheres contributed to the stronger adhesive force between primary particles. In other words, detachment of two primary PE microspheres required more powerful hydrodynamic forces than PS bonds. It is noted that the assumed characteristic length scale of separation distance was on the order of 10 nm for both polymer types. The separation distance depends on the surface roughness (S. Li *et al.*, 2011) and the fluid lubrication forces between particle surfaces (Davis *et al.*, 1986) and is not trivial to determine; however 10 nm is an accepted value for similar microparticles in the literature (Gregory, 1981; Israelachvili & Tabor, 1972; Li *et al.*, 2011; Tabor & Winterton, 1969). The attractive force between microspheres was $O(10^{-11}$ N) for PS and $O(10^{-10}$ N) for PE at a separation distance of 10 nm.

Appendix G. Wiring and Pinout Connections on the iDAS

Table F-1 shows the wiring diagram including a 9V battery, one RTC, a pressure, a micro SD card board, and the thruster. The RTC and the pressure sensor operate at 5 V and use the same serial communication of I2C (inter-integrated circuit). The RTC contains a separate 3V lithium coin cell battery (CR1220) and keeps track of time after a programmed calibration. The pressure and temperature sensor can measure up to 30 bar (~300 m depth) with a temperature range of -40 ºC to 125 ºC. It provides a pressure resolution of 200 mbar and a temperature resolution of 1 ºC. The micro SD at 5 V creates a log file of thruster speed, real time, pressure and temperature. Figure F-1 provides the pinout connections in detail.

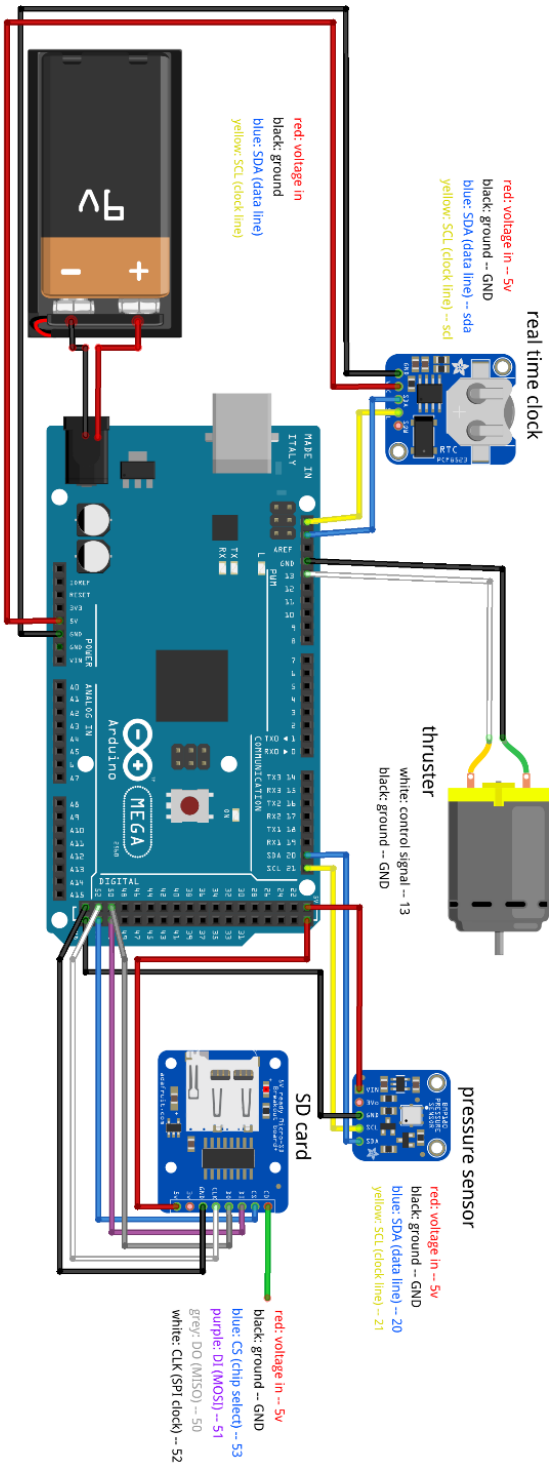

Figure G-1: Wiring diagram of an ESC, a real time clock, a pressure sensor, and a SD card module on an Arduino Mega control board.

Table G-1: Pinout connections on Arduino Mega board.

Sensor	Sensor pin	Board pin	Wire color	Description
Thruster	WHITE	13	White	T200 control signal
	BLACK	GND	Black	Ground
Real time clock	VCC	5V	Red	Input voltage
	GND	GND	Black	Ground
	SDA	SDA	Blue	Data line
	SCL	SCL	Yellow	Time line
Pressure sensor	VCC	5V	Red	Input voltage
	GND	GND	Black	Ground
	SDA	20	Blue	Data line
	SCL	21	Yellow	Time line
Micro SD	5V	5V	Red	Input voltage
	GND	GND	Black	Ground
	CS	53	Blue	Chip select
	DI	51	Purple	Master out slave in (data input)
	DO	50	Gray	Master in slave out (data output)
	CLK	52	White	Clock for serial peripheral interface (SPI)

References

Abdulagatov, I. M., & Azizov, N. D. (2006). Viscosity of aqueous calcium chloride solutions at high temperatures and high pressures. *Fluid Phase Equilibria*, *240*(2), 204–219. https://doi.org/10.1016/j.fluid.2005.12.036

Ackleson, S. G., & Rau, M. J. (2020). A method to measure marine particle aggregate disruption in situ. *Limnology and Oceanography: Methods*, *18*(11). https://doi.org/10.1002/lom3.10391

Agrawal, Y. C., & Pottsmith, H. C. (2000). Instruments for particle size and settling velocity observations in sediment transport. *Marine Geology*, *168*(1–4), 89–114. https://doi.org/10.1016/S0025-3227(00)00044-X

Agrawal, Y. C., Whitmire, A., Mikkelsen, O. A., & Pottsmith, H. C. (2008). Light scattering by random shaped particles and consequences on measuring suspended sediments by laser diffraction. *Journal of Geophysical Research*, *113*(C4), C04023. https://doi.org/10.1029/2007JC004403

Ai, L., & Vafai, K. (2005). An investigation of stokes' second problem for non-Newtonian fluids. *Numerical Heat Transfer; Part A: Applications*, *47*(10), 955–980. https://doi.org/10.1080/10407780590926390

Alldredge, A. L., & Gotschalk, C. (1988). In situ settling behavior of marine snow1. *Limnology and Oceanography*, *33*(3), 339–351. https://doi.org/10.4319/lo.1988.33.3.0339

Alldredge, A. L., Granata, T. C., Gotschalk, C. C., & Dickey, T. D. (1990). The physical strength of marine snow and its implications for particle disaggregation in the ocean. *Limnology and Oceanography*, *35*(7), 1415–1428. https://doi.org/10.4319/lo.1990.35.7.1415

Alldredge, A. L., & McGillivary, P. (1991). The attachment probabilities of marine snow and their implications for particle coagulation in the ocean. *Deep Sea Research Part A. Oceanographic Research Papers*, *38*(4), 431–443. https://doi.org/10.1016/0198-0149(91)90045-H

Alldredge, A. L., Passow, U., & Logan, B. E. (1993). The abundance and significance of a class of large, transparent organic particles in the ocean. *Deep-Sea Research Part I*. https://doi.org/10.1016/0967-0637(93)90129-Q

Alldredge, A. L., & Silver, M. W. (1988). Characteristics, dynamics and significance of marine snow. *Progress in Oceanography*, *20*(1). https://doi.org/10.1016/0079-6611(88)90053-5

Antonucci, D. C., & Schaumburg, F. D. (1975). Environmental Effects of Advanced Wastewater Treatment at South Lake Tahoe. *Journal (Water Pollution Control Federation)*, *47*(11), 2694–2701. http://www.jstor.org/stable/25038423

Aumont, O., Ethé, C., Tagliabue, A., Bopp, L., & Gehlen, M. (2015). PISCES-v2: an ocean biogeochemical model for carbon and ecosystem studies. *Geoscientific Model Development*, *8*(8). https://doi.org/10.5194/gmd-8-2465-2015

Azetsu-Scott, K., & Passow, U. (2004). Ascending marine particles: Significance of transparent exopolymer particles (TEP) in the upper ocean. *Limnology and Oceanography*, *49*(3), 741–748. https://doi.org/10.4319/lo.2004.49.3.0741

Bache D. H., Johnson C, McGilligan J. F., & Rasool E. (1997). A conceptual view of floc structure in the sweep floc domain. *Water Science and Technology*, *36*(4). https://doi.org/10.1016/S0273-1223(97)00418-6

Bakewell, H. P., & Lumley, J. L. (1967). Viscous sublayer and adjacent wall region in turbulent pipe flow. *Physics of Fluids*, *10*(9), 1880–1889. https://doi.org/10.1063/1.1762382

Berger, W. (1988). Ocean carbon flux: global maps of primary production and export production. *Biogeochemical Cycling and Fluxes between the Deep Euphotic Zone and Other Oceanic Realms*, *88*, 131–176.

Boström, M., Deniz, V., Franks, G. V., & Ninham, B. W. (2006). Extended DLVO theory: Electrostatic and non-electrostatic forces in oxide suspensions. *Advances in Colloid and Interface Science*, *123–126*, 5–15. https://doi.org/10.1016/j.cis.2006.05.001

Bouyer, D., Line, A., Cockx, A., & Do-Quang, Z. (2001). Experimental analysis of floc size distribution and hydrodynamics in a jar-test. *Chemical Engineering Research and Design*, *79*(8), 1017–1024. https://doi.org/10.1205/02638760152721587

Brant, J. (2002). Assessing short-range membrane–colloid interactions using surface energetics. *Journal of Membrane Science*, *203*(1–2), 257–273. https://doi.org/10.1016/S0376-7388(02)00014-5

Bremer, L. G. B., van Vliet, T., & Walstra, P. (1989). Theoretical and experimental study of the fractal nature of the structure of casein gels. *Journal of the Chemical Society, Faraday Transactions 1: Physical Chemistry in Condensed Phases*, *85*(10), 3359. https://doi.org/10.1039/f19898503359

Briggs, N., Dall'Olmo, G., & Claustre, H. (2020). Major role of particle fragmentation in regulating biological sequestration of CO2 by the oceans. *Science*, *367*(6479), 791–793. https://doi.org/10.1126/science.aay1790

Burd, A. B., & Jackson, G. A. (2009). Particle Aggregation. *Annual Review of Marine*

Science, *1*(1), 65–90. https://doi.org/10.1146/annurev.marine.010908.163904

Cael, B. B., Cavan, E. L., & Britten, G. L. (2021). Reconciling the Size-Dependence of Marine Particle Sinking Speed. *Geophysical Research Letters*, *48*(5). https://doi.org/10.1029/2020GL091771

Carr, S. A., Liu, J., & Tesoro, A. G. (2016). Transport and fate of microplastic particles in wastewater treatment plants. *Water Research*, *91*, 174–182. https://doi.org/10.1016/j.watres.2016.01.002

Collins, J. R., Edwards, B. R., Thamatrakoln, K., Ossolinski, J. E., Ditullio, G. R., Bidle, K. D., Doney, S. C., & Van Mooy, B. A. S. (2015). The multiple fates of sinking particles in the North Atlantic Ocean. *Global Biogeochemical Cycles*, *29*(9), 1471–1494. https://doi.org/10.1002/2014GB005037

Crowe, C. T., Schwarzkopf, J. D., Sommerfeld, M., & Tsuji, Y. (2011). *Multiphase Flows with Droplets and Particles*. CRC Press. https://doi.org/10.1201/b11103

da Costa, J. P., Santos, P. S. M., Duarte, A. C., & Rocha-Santos, T. (2016). (Nano)plastics in the environment – Sources, fates and effects. *Science of The Total Environment*, *566–567*, 15–26. https://doi.org/10.1016/j.scitotenv.2016.05.041

Davis, R. H., Serayssol, J.-M., & Hinch, E. J. (1986). The elastohydrodynamic collision of two spheres. *Journal of Fluid Mechanics*, *163*, 479–497. https://doi.org/10.1017/S0022112086002392

Derjaguin, B., & Landau, L. (1993). Theory of the stability of strongly charged lyophobic sols and of the adhesion of strongly charged particles in solutions of electrolytes. *Progress in Surface Science*, *43*(1–4), 30–59. https://doi.org/10.1016/0079-6816(93)90013-L

Dettinger, M. D. (2013). Projections and downscaling of 21st century temperatures, precipitation, radiative fluxes and winds for the Southwestern US, with focus on Lake Tahoe. *Climatic Change*, *116*(1), 17–33. https://doi.org/10.1007/s10584-012-0501-x

Dillon, T. M., & Caldwell, D. R. (1980). The Batchelor spectrum and dissipation in the upper ocean. *Journal of Geophysical Research*, *85*(C4). https://doi.org/10.1029/JC085iC04p01910

Durkin, C. (2015, November 25). *Surface phytoplankton and sinking particles offshore of Rhode Island*. Durkin Lab at Moss Landing Marine Laboratories.

Durkin, C. A., Estapa, M. L., & Buesseler, K. O. (2015). Observations of carbon export by small sinking particles in the upper mesopelagic. *Marine Chemistry*, *175*, 72–81. https://doi.org/10.1016/j.marchem.2015.02.011

Eckstein, A. C., Charonko, J., & Vlachos, P. (2008). Phase correlation processing for DPIV measurements. *Experiments in Fluids*, *45*, 485–500. https://doi.org/10.1007/s00348-008-0492-6

Eckstein, A., & Vlachos, P. (2009a). Improved DPIV accuracy using advanced windowing techniques. *2008 Proceedings of the ASME Fluids Engineering Division Summer Conference, FEDSM 2008*. https://doi.org/10.1115/FEDSM2008-55152

Eckstein, A., & Vlachos, P. P. (2009b). Assessment of advanced windowing techniques for digital particle image velocimetry (DPIV). *Measurement Science and Technology*, *20*(7). https://doi.org/10.1088/0957-0233/20/7/075402

Eckstein, A., & Vlachos, P. P. (2009c). Digital particle image velocimetry (DPIV) robust phase correlation. *Measurement Science and Technology*, *20*(5). https://doi.org/10.1088/0957-0233/20/5/055401

Elimelech, M., Gregory, J., Jia, X., & Williams, R. A. (1995). *Particle Deposition & Aggregation*. Elsevier. https://doi.org/10.1016/B978-0-7506-7024-1.X5000-6

Erdogan, M. E. (2000). Note on an unsteady flow of a viscous fluid due to an oscillating plane wall. *International Journal of Non-Linear Mechanics*, *35*(1), 1–6. https://doi.org/10.1016/S0020-7462(99)00019-0

Falgout, Z., Chen, Y., & Guildenbecher, D. R. (2019). Improving the spatial dynamic range of digital inline particle holography. *Applied Optics*, *58*(5), A65. https://doi.org/10.1364/AO.58.000A65

Fowler, S. W., & Knauer, G. A. (1986). Role of large particles in the transport of elements and organic compounds through the oceanic water column. *Progress in Oceanography*, *16*(3), 147–194. https://doi.org/10.1016/0079-6611(86)90032-7

Franks, P. J. S., Inman, B. G., MacKinnon, J. A., Alford, M. H., & Waterhouse, A. F. (2022). Oceanic turbulence from a planktonic perspective. *Limnology and Oceanography*, *67*(2), 348–363. https://doi.org/10.1002/lno.11996

Freitas, R. A. (1999). *Nanomedicine, Volume I: Basic Capabilities*. Landes Bioscience.

Friedlingstein, P., O'Sullivan, M., Jones, M. W., Andrew, R. M., Gregor, L., Hauck, J., Le Quéré, C., Luijkx, I. T., Olsen, A., Peters, G. P., Peters, W., Pongratz, J., Schwingshackl, C., Sitch, S., Canadell, J. G., Ciais, P., Jackson, R. B., Alin, S. R., Alkama, R., … Zheng, B. (2022). Global Carbon Budget 2022. *Earth System Science Data*, *14*(11), 4811–4900. https://doi.org/10.5194/essd-14-4811-2022

Fuchs, H. L., Mullineaux, L. S., & Solow, A. R. (2004). Sinking behavior of gastropod larvae (*Ilyanassa obsoleta*) in turbulence. *Limnology and Oceanography*, *49*(6). https://doi.org/10.4319/lo.2004.49.6.1937

George, R., Flick, R. E., & Guza, R. T. (1994). Observations of turbulence in the surf zone. *Journal of Geophysical Research*, *99*(C1). https://doi.org/10.1029/93JC02717

Glasgow, L. A., & Luecke, R. H. (1980). Mechanisms of Deaggregation for Clay-Polymer Flocs in Turbulent Systems. *Industrial & Engineering Chemistry Fundamentals*, *19*(2), 148–156. https://doi.org/10.1021/i160074a003

Goldthwait, S., Yen, J., Brown, J., & Alldredge, A. (2004). Quantification of marine snow fragmentation by swimming euphausiids. *Limnology and Oceanography*, *49*(4). https://doi.org/10.4319/lo.2004.49.4.0940

Graham, G. W., & Nimmo Smith, W. A. M. (2010). The application of holography to the analysis of size and settling velocity of suspended cohesive sediments. *Limnology and Oceanography: Methods*, *8*(1), 1–15. https://doi.org/10.4319/lom.2010.8.1

Gregory, J. (1981). Approximate expressions for retarded van der waals interaction. *Journal of Colloid and Interface Science*, *83*(1), 138–145. https://doi.org/10.1016/0021-9797(81)90018-7

Gross, T. F., & Nowell, A. R. M. (1985). Spectral Scaling in a Tidal Boundary Layer. *Journal of Physical Oceanography*, *15*(5). https://doi.org/10.1175/1520-0485(1985)015<0496:SSIATB>2.0.CO;2

Gruber, N., & Galloway, J. N. (2008). An Earth-system perspective of the global nitrogen cycle. *Nature*, *451*, 293–296. https://doi.org/10.1038/nature06592

Hall, P. (1978). Linear stability of flat Stokes layers. *Proc R Soc London Ser A*, *395*(1697). https://doi.org/10.1098/rspa.1978.0037

Hamaker, H. C. (1937). The London—van der Waals attraction between spherical particles. *Physica*, *4*(10), 1058–1072. https://doi.org/10.1016/S0031-8914(37)80203-7

Hehner, M. T., Gatti, D., & Kriegseis, J. (2019). Stokes-layer formation under absence of moving parts - A novel oscillatory plasma actuator design for turbulent drag reduction. *Physics of Fluids*, *31*(051701). https://doi.org/10.1063/1.5094388

Henson, S. A., Sanders, R., Madsen, E., Morris, P. J., Le Moigne, F., & Quartly, G. D. (2011). A reduced estimate of the strength of the ocean's biological carbon pump. *Geophysical Research Letters*, *38*(4). https://doi.org/10.1029/2011GL046735

Higashitani, K., Iimura, K., & Sanda, H. (2001). Simulation of deformation and breakup of large aggregates in flows of viscous fluids. *Chemical Engineering Science*. https://doi.org/10.1016/S0009-2509(00)00477-2

Hinze, J. O. (1955). Fundamentals of the hydrodynamic mechanism of splitting in

dispersion processes. *AIChE Journal*, *1*(3), 289–295. https://doi.org/10.1002/aic.690010303

Howlett, J., Abramowitz, M., & Stegun, I. A. (1966). Handbook of Mathematical Functions. In *The Mathematical Gazette*. https://doi.org/10.2307/3614753

Hsu, J. P., & Glasgow, L. A. (1983). Floc size reduction in the turbulent environment. *Particulate Science and Technology*, *1*(2), 205–222. https://doi.org/10.1080/02726358308906366

Israelachvili, J. N. (2011). *Intermolecular and Surface Forces*. Elsevier. https://doi.org/10.1016/C2011-0-05119-0

Israelachvili, J. N., & McGuiggan, P. M. (1988). Forces Between Surfaces in Liquids. *Science*, *241*(4867), 795–800. https://doi.org/10.1126/science.241.4867.795

Israelachvili, J. N., & Tabor, D. (1972). The measurement of van der Waals dispersion forces in the range 1.5 to 130 nm. *Proceedings of the Royal Society of London. A. Mathematical and Physical Sciences*, *331*(1584), 19–38. https://doi.org/10.1098/rspa.1972.0162

Jackson, G. A. (1994). Particle trajectories in a rotating cylinder: implications for aggregation incubations. *Deep-Sea Research Part I*, *41*(3), 429–437. https://doi.org/10.1016/0967-0637(94)90089-2

Jackson, G. A. (1995). Comparing observed changes in particle size spectra with those predicted using coagulation theory. *Deep-Sea Research Part II*, *42*(1), 159–184. https://doi.org/10.1016/0967-0645(95)00010-N

Jackson, G. A. (2015). Coagulation in a rotating cylinder. *Limnology and Oceanography: Methods*, *13*(4), 194–201. https://doi.org/10.1002/lom3.10018

Jarvis, P., Jefferson, B., Gregory, J., & Parsons, S. A. (2005). A review of floc strength and breakage. *Water Research*, *39*(14), 3121–3137. https://doi.org/10.1016/j.watres.2005.05.022

Jiang, Q., & Logan, B. E. (1991). Fractal Dimensions of Aggregates Determined from Steady-State Size Distributions. *Environmental Science and Technology*, *25*(12), 2031–2038. https://doi.org/10.1021/es00024a007

Johnson, C. P., Li, X., & Logan, B. E. (1996). Settling Velocities of Fractal Aggregates. *Environmental Science & Technology*, *30*(6). https://doi.org/10.1021/es950604g

Johnson, R. E. (1988). Steady-state coating flows inside a rotating horizontal cylinder. *Journal of Fluid Mechanics*, *190*, 321–342. https://doi.org/10.1017/S0022112088001338

Kármán, T. V. (1921). Über laminare und turbulente Reibung. *ZAMM - Journal of Applied Mathematics and Mechanics / Zeitschrift Für Angewandte Mathematik Und Mechanik*, *1*, 233–252. https://doi.org/10.1002/zamm.19210010401

Kerczek, C. Von, & Davis, S. H. (1974). Linear stability theory of oscillatory Stokes layers. *Journal of Fluid Mechanics*, *62*(4), 753–773. https://doi.org/10.1017/S0022112074000929

Kester, D. R., Duedall, I. W., Connors, D. N., & Pytkowicz, R. M. (1967). Preparation Of Artificial Seawater1. *Limnology and Oceanography*, *12*(1), 176–179. https://doi.org/10.4319/lo.1967.12.1.0176

Kim, N. H. (2018). Particulate Fouling and On-Line Cleaning of Ferric Oxide Particles in Internally Enhanced Tubes. *Heat Transfer Engineering*, *39*(1), 40–50. https://doi.org/10.1080/01457632.2017.1280285

Kiørboe, T. (2001). Formation and fate of marine snow: small-scale processes with large-scale implications. *Scientia Marina*, *65*(S2). https://doi.org/10.3989/scimar.2001.65s257

Kirilenko, A. P., & Sedjo, R. A. (2007). Climate change impacts on forestry. *Proceedings of the National Academy of Sciences*, *104*(50), 19697–19702. https://doi.org/10.1073/pnas.0701424104

Kranenburg, C. (1994). The Fractal Structure of Cohesive Sediment Aggregates. *Estuarine, Coastal and Shelf Science*, *39*(5), 451–460. https://doi.org/10.1006/ecss.1994.1075

Kusters, K. A. (1991). *The influence of turbulence on aggregation of small particles in agitated vessels*. Eindhoven University of Technology.

Kwon, E. Y., Primeau, F., & Sarmiento, J. L. (2009). The impact of remineralization depth on the air–sea carbon balance. *Nature Geoscience*, *2*(9). https://doi.org/10.1038/ngeo612

Landau, L. D., & Lifshitz, E. M. (1987). *Fluid Mechanics*. Elsevier. https://doi.org/10.1016/C2013-0-03799-1

Laruelle, G. G., Roubeix, V., Sferratore, A., Brodherr, B., Ciuffa, D., Conley, D. J., Dürr, H. H., Garnier, J., Lancelot, C., LeThiPhuong, Q., Meunier, J. D., Meybeck, M., Michalopoulos, P., Moriceau, B., Ni Longphuirt, S., Loucaides, S., Papush, L., Presti, M., Ragueneau, O., … Van Cappellen, P. (2009). Anthropogenic perturbations of the silicon cycle at the global scale: Key role of the land-ocean transition. *Global Biogeochemical Cycles*, *23*(4). https://doi.org/10.1029/2008GB003267

Lee, C., & Kramer, T. A. (2004). Prediction of three-dimensional fractal dimensions using

the two-dimensional properties of fractal aggregates. *Advances in Colloid and Interface Science*, *112*(1–3), 49–57. https://doi.org/10.1016/j.cis.2004.07.001

Lee, K., Stoffyn-Egli, P., & Owens, E. H. (2002). The OSSA II Pipeline Oil Spill: Natural Mitigation of a Riverine Oil Spill by Oil–Mineral Aggregate Formation. *Spill Science & Technology Bulletin*, *7*(3–4), 149–154. https://doi.org/10.1016/S1353-2561(02)00056-7

Li, K. W., & Marfatia, A. C. (1971). Stokes second problem for the cylinder. *Journal of Fluids Engineering, Transactions of the ASME*, *93*(2), 326–328. https://doi.org/10.1115/1.3425238

Li, S., Marshall, J. S., Liu, G., & Yao, Q. (2011). Adhesive particulate flow: The discrete-element method and its application in energy and environmental engineering. *Progress in Energy and Combustion Science*, *37*(6), 633–668. https://doi.org/10.1016/j.pecs.2011.02.001

Li, T., Zhu, Z., Wang, D., Yao, C., & Tang, H. (2007). The strength and fractal dimension characteristics of alum-kaolin flocs. *International Journal of Mineral Processing*. https://doi.org/10.1016/j.minpro.2006.09.012

Maestro, A., Guzmán, E., Ortega, F., & Rubio, R. G. (2014). Contact angle of micro- and nanoparticles at fluid interfaces. *Current Opinion in Colloid & Interface Science*, *19*(4), 355–367. https://doi.org/10.1016/j.cocis.2014.04.008

Malkiel, E., Abras, J. N., & Katz, J. (2004). Automated scanning and measurements of particle distributions within a holographic reconstructed volume. *Measurement Science and Technology*, *15*(4), 601–612. https://doi.org/10.1088/0957-0233/15/4/001

Mari, X., Passow, U., Migon, C., Burd, A. B., & Legendre, L. (2017). Transparent exopolymer particles: Effects on carbon cycling in the ocean. *Progress in Oceanography*, *151*, 13–37. https://doi.org/10.1016/j.pocean.2016.11.002

Matsuo, T., & Unno, H. (1981). Forces Acting on Floc and Strength of Floc. *Journal of the Environmental Engineering Division*, *107*(3), 527–545. https://doi.org/10.1061/JEEGAV.0001174

Maxey, M. R., & Riley, J. J. (1983). Equation of motion for a small rigid sphere in a nonuniform flow. *Physics of Fluids*, *26*(4), 883. https://doi.org/10.1063/1.864230

McCave, I. N. (1984). Erosion, transport and deposition of fine-grained marine sediments. *Geological Society Special Publication*, *15*, 35–69. https://doi.org/10.1144/GSL.SP.1984.015.01.03

McNutt, M. (2013). Climate Change Impacts. *Science*, *341*(6145), 435–435.

https://doi.org/10.1126/science.1243256

Mendez, M. A., Raiola, M., Masullo, A., Discetti, S., Ianiro, A., Theunissen, R., & Buchlin, J.-M. (2017). POD-based background removal for particle image velocimetry. *Experimental Thermal and Fluid Science*, *80*. https://doi.org/10.1016/j.expthermflusci.2016.08.021

Merkus, H. G. (2009). *Particle Size Measurements* (Vol. 17). Springer Netherlands. https://doi.org/10.1007/978-1-4020-9016-5

Merzkirch, W., & Gui, L. (2000). A comparative study of the MQD method and several correlation-based PIV evaluation algorithms. *Experiments in Fluids*, *28*(1). https://doi.org/10.1007/s003480050005

Middelburg, J. J. (2011). Chemoautotrophy in the ocean. *Geophysical Research Letters*, *38*(24). https://doi.org/10.1029/2011GL049725

Muller-Karger, F. E. (2005). The importance of continental margins in the global carbon cycle. *Geophysical Research Letters*, *32*(1). https://doi.org/10.1029/2004GL021346

Neumann, A. W., David, R., & Zuo, Y. (2010). *Applied Surface Thermodynamics* (A. W. Neumann, R. David, & Y. Zuo (eds.)). CRC Press. https://doi.org/10.1201/EBK0849396878

O'Neil, P. V. (2011). Advanced engineering mathematics. In *Cengage learning*.

Otsu, N. (1979). A Threshold Selection Method from Gray-Level Histograms. *IEEE Transactions on Systems, Man, and Cybernetics*, *9*(1). https://doi.org/10.1109/TSMC.1979.4310076

Owen, R. B., & Zozulya, A. A. (2000). In-line digital holographic sensor for monitoring and characterizing marine particulates. *Optical Engineering*, *39*(8), 2187. https://doi.org/10.1117/1.1305542

Parker, D. S., Kaufman, W. J., & Jenkins, D. (1972). Floc breakup in turbulent flocculation processes. *ASCE J Sanit Eng Div*, *98*(1), 79–99.

Passow, U. (2002a). Transparent exopolymer particles (TEP) in aquatic environments. *Progress in Oceanography*, *55*(3–4), 287–333. https://doi.org/10.1016/S0079-6611(02)00138-6

Passow, U. (2002b). Transparent exopolymer particles (TEP) in aquatic environments. *Progress in Oceanography*, *55*(3–4), 287–333. https://doi.org/10.1016/S0079-6611(02)00138-6

Pope, S. B. (2001). *Turbulent Flows*. IOP Publishing.

Raju, N., & Meiburg, E. (1997). Dynamics of small, spherical particles in vortical and stagnation point flow fields. *Physics of Fluids*, *9*(2), 299–314. https://doi.org/10.1063/1.869150

Rau, M. J., Ackleson, S. G., & Smith, G. B. (2018). Effects of turbulent aggregation on clay floc breakup and implications for the oceanic environment. *PLoS ONE*, *13*(12). https://doi.org/10.1371/journal.pone.0207809

Rayleigh, Lord. (1911). On the motion of solid bodies through viscous liquid. *The London, Edinburgh, and Dublin Philosophical Magazine and Journal of Science*, *21*(126), 697–711. https://doi.org/10.1080/14786440608637084

Renier, N., & Durkin, C. (2016, August 30). *The Biological Pump*. Https://Nrenier.Com/.

Rivero, M., Garzón, F., Núñez, J., & Figueroa, A. (2019). Study of the flow induced by circular cylinder performing torsional oscillation. *European Journal of Mechanics, B/Fluids*, *78*, 245–251. https://doi.org/10.1016/j.euromechflu.2019.08.002

Rumpf, H. (1962). The Strength of Granules and Agglomerates. *Agglomeration*, 379–413.

Saha, D., Babler, M. U., Holzner, M., Soos, M., Lüthi, B., Liberzon, A., & Kinzelbach, W. (2016). Breakup of Finite-Size Colloidal Aggregates in Turbulent Flow Investigated by Three-Dimensional (3D) Particle Tracking Velocimetry. *Langmuir*, *32*(1), 55–65. https://doi.org/10.1021/acs.langmuir.5b03804

Saha, D., Soos, M., Lüthi, B., Holzner, M., Liberzon, A., Babler, M. U., & Kinzelbach, W. (2014). Experimental characterization of breakage rate of colloidal aggregates in axisymmetric extensional flow. *Langmuir*, *30*(48), 14385–14395. https://doi.org/10.1021/la502686b

Salam, M. A., & Noguchi, T. (2005). Impact of Human Activities on Carbon Dioxide (CO2) Emissions: A Statistical Analysis. *The Environmentalist*, *25*(1), 19–30. https://doi.org/10.1007/s10669-005-3093-4

Santschi, P. H. (2018). Marine colloids, agents of the self-cleansing capacity of aquatic systems: Historical perspective and new discoveries. *Marine Chemistry*, *207*, 124–135. https://doi.org/10.1016/j.marchem.2018.11.003

Scarano, F. (2002). Interative image deformation methods in PIV. *Measurement Science and Technology*, *13*(1). https://doi.org/10.1088/0957-0233/13/1/201

Schlichting, H. (1979). *Boundary layer theory: Seventh edition.*

Schlichting, Herman. (1979). Boundary-Layer Theory 7th ed. In *McGraw-Hill*. https://doi.org/10.1119/1.1971812

Serra, T., & Casamitjana, X. (1998). Structure of the Aggregates During the Process of

Aggregation and Breakup Under a Shear Flow. *Journal of Colloid and Interface Science*, *206*(2), 505–511. https://doi.org/10.1006/jcis.1998.5714

Shams, M., Alam, I., & Chowdhury, I. (2020). Aggregation and stability of nanoscale plastics in aquatic environment. *Water Research*, *171*, 115401. https://doi.org/10.1016/j.watres.2019.115401

Shanks, A. L., & Edmondson, E. W. (1989). Laboratory-made artificial marine snow: a biological model of the real thing. *Marine Biology*, *101*(4), 463–470. https://doi.org/10.1007/BF00541648

Smayda, T. J. (1971). Normal and accelerated sinking of phytoplankton in the sea. *Marine Geology*, *11*(2), 105–122. https://doi.org/10.1016/0025-3227(71)90070-3

Smith, S. J., & Friedrichs, C. T. (2011). Size and settling velocities of cohesive flocs and suspended sediment aggregates in a trailing suction hopper dredge plume. *Continental Shelf Research*, *31*, 50–63. https://doi.org/10.1016/j.csr.2010.04.002

Snoeyink, C., Barman, S., & Christopher, G. F. (2015). Contact Angle Distribution of Particles at Fluid Interfaces. *Langmuir*, *31*(3), 891–897. https://doi.org/10.1021/la5040195

Sobel, I., & Feldman, G. (1968). A 3 × 3 Isotropic Gradient Operator for Image Processing. *Stanford Artificial Project*, 271–272.

Song, Y., & Rau, M. J. (2020a). Viscous fluid flow inside an oscillating cylinder and its extension to Stokes' second problem. *Physics of Fluids*, *32*(4), 043601. https://doi.org/10.1063/1.5144415

Song, Y., & Rau, M. J. (2020b, July 13). Disruption Behavior of Aggregates in a Rotating/Oscillating Cylindrical Tank and Implications for Particle Transport in the Ocean. *Volume 2: Fluid Mechanics; Multiphase Flows*. https://doi.org/10.1115/FEDSM2020-20237

Song, Y., & Rau, M. J. (2022). A novel method to study the fragmentation behavior of marine snow aggregates in controlled shear flow. *Limnology and Oceanography: Methods*, *20*(10), 618–632. https://doi.org/10.1002/lom3.10509

Song, Y., & Rau, M. J. (2019). Characterization of Aggregate Disruption Using Organic Marine Particles and Particle Tracking Measurements in Rotating/Oscillating Aggregation Tanks. *Volume 5: Multiphase Flow*, *5*, 1–7. https://doi.org/10.1115/AJKFluids2019-5499

Sonntag, R. C., & Russel, W. B. (1986). Structure and breakup of flocs subjected to fluid stresses. I. Shear experiments. *Journal of Colloid And Interface Science*. https://doi.org/10.1016/0021-9797(86)90175-X

Soos, M., Moussa, A. S., Ehrl, L., Sefcik, J., Wu, H., & Morbidelli, M. (2008). Effect of shear rate on aggregate size and morphology investigated under turbulent conditions in stirred tank. *Journal of Colloid and Interface Science*, *319*(2), 577–589. https://doi.org/10.1016/j.jcis.2007.12.005

Spicer, P. T., Keller, W., & Pratsinis, S. E. (1996). The effect of impeller type on floc size and structure during shear-induced flocculation. *Journal of Colloid and Interface Science*, *184*(1), 112–122. https://doi.org/10.1006/jcis.1996.0601

Stokes, G. G. (1850). On the theories of the internal friction of fluids in motion. In *Transactions of the Cambridge Philosophical Society* (pp. 75–129). https://doi.org/10.1017/CBO9780511702242

Struyf, E., Smis, A., van Damme, S., Meire, P., & Conley, D. J. (2009). The global biogeochemical silicon cycle. *Silicon*, *1*, 207–213. https://doi.org/10.1007/s12633-010-9035-x

Tabor, D., & Winterton, R. H. S. (1969). The direct measurement of normal and retarded van der Waals forces. *Proceedings of the Royal Society of London. A. Mathematical and Physical Sciences*, *312*(1511), 435–450. https://doi.org/10.1098/rspa.1969.0169

Tambo, N., & Hozumi, H. (1979). Physical characteristics of flocs-II. Strength of floc. *Water Research*, *13*(5), 421–427. https://doi.org/10.1016/0043-1354(79)90034-4

Tang, S., Ma, Y., & Sebastine, I. M. (2001). The fractal nature of Escherichia coli biological flocs. *Colloids and Surfaces B: Biointerfaces*, *20*(3), 211–218. https://doi.org/10.1016/S0927-7765(00)00179-X

Tang, S., Preece, J. M., McFarlane, C. M., & Zhang, Z. (2000). Fractal Morphology and Breakage of DLCA and RLCA Aggregates. *Journal of Colloid and Interface Science*, *221*(1). https://doi.org/10.1006/jcis.1999.6565

Thomas, D. G. (1964). Turbulent disruption of flocs in small particle size suspensions. *AIChE Journal*, *10*(4), 517–523. https://doi.org/10.1002/aic.690100420

Thorpe, S. A. (2005). The turbulent ocean. In *The Turbulent Ocean*. https://doi.org/10.1017/CBO9780511819933

Tirumkudulu, M., & Acrivos, A. (2001). Coating flows within a rotating horizontal cylinder: Lubrication analysis, numerical computations, and experimental measurements. *Physics of Fluids*, *13*(1). https://doi.org/10.1063/1.1329909

Tol, R. S. J. (2018). The Economic Impacts of Climate Change. *Review of Environmental Economics and Policy*, *12*(1), 4–25. https://doi.org/10.1093/reep/rex027

Tomi, D. T., & Bagster, D. F. (1980). Behaviour of aggregates in stirred vessels. *Minerals*

Science and Engineering, *56*(1), 9–18.

Torza, S., Cox, R. G., & Mason, S. G. (1972). Particle motions in sheared suspensions XXVII. Transient and steady deformation and burst of liquid drops. *Journal of Colloid And Interface Science*. https://doi.org/10.1016/0021-9797(72)90255-X

Turner, M. R., & Weidman, P. (2019). The boundary layer flow induced above the torsional motion of a disk. *Physics of Fluids*, *31*(043604). https://doi.org/10.1063/1.5091797

Vajihinejad, V., & Soares, J. B. P. (2018). Monitoring polymer flocculation in oil sands tailings: A population balance model approach. *Chemical Engineering Journal*, *346*, 447–457. https://doi.org/10.1016/j.cej.2018.04.039

van Oss, Carel J. (2006). *Interfacial Forces in Aqueous Media*. CRC Press. https://doi.org/10.1201/9781420015768

Van Oss, Carel J., Chaudhury, M. K., & Good, R. J. (1988). Interfacial Lifshitz-van der Waals and polar interactions in macroscopic systems. *Chemical Reviews*, *88*(6), 927–941. https://doi.org/10.1021/cr00088a006

van Oss, Carel Jan. (2008). *The Extended DLVO Theory* (pp. 31–48). https://doi.org/10.1016/S1573-4285(08)00203-2

Vander Zanden, M. J., Chandra, S., Allen, B. C., Reuter, J. E., & Goldman, C. R. (2003). Historical Food Web Structure and Restoration of Native Aquatic Communities in the Lake Tahoe (California–Nevada) Basin. *Ecosystems*, *6*(3), 274–288. https://doi.org/10.1007/s10021-002-0204-7

Verwey, E. J., & Overbeek, J. T. G. (1948). *Theory of the Stability of Lyophobic Colloids*. Elsevier.

Vlachos, P. P. (2015). *Prana PIV codes*. https://github.com/pvlachos/prana

Vrieling, E. G., Sun, Q., Tian, M., Kooyman, P. J., Gieskes, W. W. C., Van Santen, R. A., & Sommerdijk, N. A. J. M. (2007). Salinity-dependent diatom biosilicification implies an important role of external ionic strength. *Proceedings of the National Academy of Sciences of the United States of America*, *104*(25), 10441–10446. https://doi.org/10.1073/pnas.0608980104

Wahab, A., & Mahiuddin, S. (2001). Isentropic Compressibility and Viscosity of Aqueous and Methanolic Calcium Chloride Solutions. *Journal of Chemical & Engineering Data*, *46*(6), 1457–1463. https://doi.org/10.1021/je0100721

Weise, A. M., Nalewajko, C., & Lee, K. (1999). Oil-Mineral Fine Interactions Facilitate Oil Biodegradation in Seawater. *Environmental Technology*, *20*(8), 811–824. https://doi.org/10.1080/09593332008616877

Westerweel, J., & Scarano, F. (2005). Universal outlier detection for PIV data. *Experiments in Fluids*, *39*, 1096–1100. https://doi.org/10.1007/s00348-005-0016-6

Wheeler, T., & von Braun, J. (2013). Climate Change Impacts on Global Food Security. *Science*, *341*(6145), 508–513. https://doi.org/10.1126/science.1239402

Wieneke, B. (2015). PIV uncertainty quantification from correlation statistics. *Measurement Science and Technology*, *26*(7). https://doi.org/10.1088/0957-0233/26/7/074002

Wieneke, B., & Pfeiffer, K. (2010). Adaptive PIV with variable interrogation window size and shape. *5th Int Symp on Applications of Laser Techniques to Fluid Mechanics*.

Williams, A., Janssen, J. J. M., & Prins, A. (1997). Behaviour of droplets in simple shear flow in the presence of a protein emulsifier. *Colloids and Surfaces A: Physicochemical and Engineering Aspects*. https://doi.org/10.1016/S0927-7757(96)03972-6

Xu, W., Jericho, M. H., Meinertzhagen, I. A., & Kreuzer, H. J. (2002). Digital in-line holography of microspheres. *Applied Optics*, *41*(25), 5367. https://doi.org/10.1364/AO.41.005367

Xue, Z., Charonko, J. J., & Vlachos, P. P. (2014). Signal-to-noise ratio, error and uncertainty of PIV measurement. *10th International Symposium on Particle Image Velocimetry*. https://doi.org/10.1088/0957-0233/25/11/115301

Yang, M. Y., Chan, J. G. Y., & Chan, H. K. (2014). Pulmonary drug delivery by powder aerosols. *Journal of Controlled Release*, *193*, 228–240. https://doi.org/10.1016/j.jconrel.2014.04.055

Yuan, X., & Shen, X. (2008). Block Matching Algorithm Based on Particle Swarm Optimization for Motion Estimation. *2008 International Conference on Embedded Software and Systems*. https://doi.org/10.1109/ICESS.2008.35

Yue, X.-L., & Gao, Q.-X. (2018). Contributions of natural systems and human activity to greenhouse gas emissions. *Advances in Climate Change Research*, *9*(4), 243–252. https://doi.org/10.1016/j.accre.2018.12.003

Zaccone, A., Soos, M., Lattuada, M., Wu, H., Bäbler, M. U., & Morbidelli, M. (2009). Breakup of dense colloidal aggregates under hydrodynamic stresses. *Physical Review E - Statistical, Nonlinear, and Soft Matter Physics*, *79*. https://doi.org/10.1103/PhysRevE.79.061401

Zetsche, E., Larsson, A. I., Iversen, M. H., & Ploug, H. (2020). Flow and diffusion around and within diatom aggregates: Effects of aggregate composition and shape. *Limnology and Oceanography*, *65*(8), 1818–1833. https://doi.org/10.1002/lno.11420

Zhang, J., & Buffle, J. (1996). Multi-method determination of the fractal dimension of hematite aggregates. *Colloids and Surfaces A: Physicochemical and Engineering Aspects*, *107*, 175–187. https://doi.org/10.1016/0927-7757(95)03344-0

Ziervogel K, Sweet J, Bretherton L, Quigg A, & Passow U. (2020). Fragmentation of marine snow and marine oil snow due to small-scale turbulence. *Ocean Sciences Meeting 2020*.

YIXUAN SONG

EDUCATION

The Pennsylvania State University *University Park, PA*
Ph.D., Mechanical Engineering May 2023

Dissertation: Determination of Marine Aggregate Fragmentation Strength through Laboratory and Field Methods
Advisor: Matthew J. Rau

University of Southern California *Los Angeles, CA*
M.S., Mechanical and Aerospace Engineering May 2018

Shanghai Jiao Tong University *Shanghai, China*
B.S., Mechanical Engineering Aug 2016

SELECTED PUBLICATIONS

3. **Y. Song**, A. Burd, M. Rau, (2023) Aggregate deformation and its role in the fragmentation of marine snow, *Science Advances*. (*submitted*).

2. **Y. Song**, M. Rau, (2022) A novel method to study the fragmentation behavior of marine snow aggregates in controlled shear flow, *Limnology and Oceanography: Methods* 20(10): 618-632. doi.org/10.1002/lom3.10509

1. **Y. Song**, M. Rau, (2020) Viscous fluid flow inside an oscillating cylinder and its extension to Stokes' second problem, *Physics of Fluids* 32(4): 043601. doi.org/10.1063/1.5144415

SELECTED PRESENTATIONS

4. **Y. Song**, A. Burd, M. Rau, (2022) Deformation and fragmentation behaviors of phytoplankton and plastic particle aggregates, *APS Division of Fluid Dynamics Meeting*, Indianapolis, IN.

3. **Y. Song**, (2022) The effect of phytoplankton species on morphology and strength of laboratory-cultured marine snow aggregates, *Fluid Dynamics Research Consortium*, The Pennsylvania State University, University Park, PA.

2. **Y. Song**, A. Burd, M. Rau, (2021) Study of shear-induced deformation and fragmentation of laboratory-cultured marine aggregates, *APS Division of Fluid Dynamics Meeting*, Phoenix, AZ.

1. **Y. Song**, M. Rau, (2019) Characterization of a rotating/oscillating tank for studying particle aggregation, *Fluids Engineering Division Summer Meeting*, San Francisco, CA.

CRUISES

Research Scientist 2022
12-day cruise, Gulf of Maine, R/V Hugh R. Sharp, OCE-1948283.

Research Scientist 2022
2-day cruise, Lake Tahoe, CA, R/V Bob Richards.

AWARDS

Kulakowski Travel Award, Penn State 2019
Undergraduate Student Award, SJTU 2014, 2015
Merit Student, SJTU 2014